Title

A First Geologic Map of Isla Monserrate, Bahia De Loreto, Baja California Sur

Author

Yu, Kyung Woong

Publication Date

2024

Peer reviewed|Thesis/dissertation

A First Geologic Map of Isla Monserrate, Bahia De Loreto, Baja California Sur

By

KYUNG-WOONG YU

THESIS

Submitted in partial satisfaction of the requirements for the degree of

MASTER OF SCIENCE

in

Geology

in the

OFFICE OF GRADUATE STUDIES

of the

UNIVERSITY OF CALIFORNIA

DAVIS

Approved:

_____

Nicholas Pinter, Chair

_____

Michael Oskin

_____

John Fletcher

Committee in Charge

2024

Abstract:

Isla Monserrate, in the Gulf of California, records a history that spans arc convergent in the early Miocene, to rift-related extension during the middle Miocene to Quaternary uplift. But the island's geology is understudied. To understand Isla Monserrate's geological history, this study utilized geological and structural mapping, augmented by drone-based high-resolution orthoimagery and Digital Elevation Model (DEM). The lithological units, structures, and geomorphology mapped on Isla Monserrate record three main stages of the island's geological history: pre-extensional, early syn-extensional, and late syn-extensional.

The study identified at least five mappable lithological units: (1) pre-extensional Comondú Group volcanic and volcaniclastic rocks, (2) early syn-extensional pyroclastics, (3) early syn-extensional Pliocene marine deposits, (4) late syn-extensional littoral and shallow-marine sediments covering coastal terraces, and (5) recent alluvium and coastal sediments. The Comondú Group consists of volcaniclastic sandstones, debris - flow deposits, andesitic to mafic lavas, and syn-extensional dikes. Pyroclastic deposits include silicic tuff and welded ignimbrites. Pliocene sedimentary deposits record a marine transgression in the region, including basal conglomerates and fossiliferous marlstones.

Isla Monserrate has a sequence of coastal terraces and elevated platforms, documenting Quaternary uplift of the island. The lowest terrace level has elevations of ~15 m above sea level, while the highest terrace platforms in the island's interior are above 200 m. The lowest terrace levels are covered in fossiliferous and coral-rich sand and gravel. Higher terrace platforms are capped by sheets of secondary carbonates, likely derived from weathering of Pliocene carbonate rich sediments.

Isla Monserrate documents progressive eastward tilting above a west-directed detachment system. At least three west-dipping, low-angle detachment faults have been found. The syn-extensional basins systematically increase in size to the west, which may reflect a westward migration of deformation through the stacked system of detachment faults. High-angle faults with significantly smaller offset cross-cut Pliocene rocks. The overall orientation of rock units on Monserrate shows progressive tilting down to the east: from the oldest to youngest, Comondú layers and units dip ~50-70° to the east; silicic tuff strata ~30˚; Pliocene deposits ~10-25°. Kinematic analysis of fault striae indicates that the principal axis of extension is oriented E-W to ESE-WNW, consistent with a transtensional shearing

Based on these data, Isla Monserrate seems to have developed through the following stages. Subduction arc volcanism deposited the Comondú volcanics, which were then rotated by the initiation of extensional faulting. Dikes were emplaced at this stage, along with the deposition of pyroclastic units. Extension-induced lithospheric thinning submerged the area during the late Miocene to early Pliocene, depositing the first marine sediments at this location. Submergence switched to emergence, initiating uplift the island and development of coastal terraces, likely beginning in the Quaternary.

Chapter 1. Introduction

1.1 Study Area

1.1.1 Gulf of California

Over the last 25 million years, the Gulf of California has evolved from a convergent subduction arc to an oblique seafloor spreading center (Axen and Fletcher 1998; Busby et al. 2020; Calmus et al. 2011; Dorsey et al. 2001; Fletcher and Munguía 2000; Oskin, Stock, and Martín-Barajas 2001; Sawlan 1991; Umhoefer et al. 2001). The tectonic history of the Gulf can be roughly organized into three stages based on the dominant tectonism: (1) pre-extensional convergence, (2) early syn-extension, (3) late syn-extension.

During the pre-extension stage, convergent tectonism dominated the Gulf Extensional Province (GEP), as the Farallon Plate subducted eastward under the North American Plate, creating an Andean-style volcanic arc (Busby et al. 2020; Dorsey et al. 2001; Sawlan 1991; Umhoefer et al. 2001; Umhoefer, Mayer, and Dorsey 2002). Initially, the subduction-induced volcanic activity was mostly centered around central Mexico, creating the Sierra Madre Occidental (Sutherland et al. 2012; Umhoefer et al. 2002). This volcanism later migrated westward towards modern-day Baja California, resulting in the formation of extensive calc-alkaline volcanics and other rocks of the Comondú Group (Busby et al. 2020; Umhoefer et al. 2001, 2002). The Comondú is best exposed along the eastern side of Baja California Sur and consists of fluvial sediments, volcaniclastic debris, and lava flows that were deposited between ~25 Ma and 12 Ma (Busby et al. 2020; Drake et al. 2017; Ferrari et al. 2012, 2018; Umhoefer et al. 2001). The Comondú is categorized into Lower, Middle, and Upper units, based on depositional ages.

The Lower Comondú, formed between 25 to 19 Ma, records the Baja California region's shift from shallow marine to terrestrial forerarc environment, as shown by outcrops in Bahía de La Paz and Timbabichi (Drake et al. 2017; Gidde 1992; Hausback 1984), followed by the onset of Sierra Madre Occidental volcanic front's westward migration (Bryan et al. 2014; Busby et al. 2020; Calmus et al. 2011; Drake et al. 2017; Ferrari et al. 2018). Although lateral variability exists, the unit generally coarsens upward. Fine to pebbly volcaniclastic sandstones dominate the lower section of the Lower Comondú, which are overlain by layers of conglomerates, tuff, and volcanic breccias (Drake et al. 2017). Such pattern suggests a progressive shift from distal to proximal volcaniclastic sedimentation which has been interpreted as the encroachment of volcanic arc from the east (Drake et al. 2017; Sutherland et al. 2012; Umhoefer et al. 2001, 2002).

The contact between the Lower and Middle Comondú is marked by a transition from fluvial deposits to volcaniclastic debris flows, as shown by the erosional unconformity between the Middle Comondú Agua Verde formation (17.8 ± 0.7 Ma as dated by Sawlan and Smith 1984) and the underlying Lower Comondú La Aguililla formation (Ferrari et al. 2018; Hausback 1984; Sawlan and Smith 1984; Umhoefer et al. 2001). Thick sequences of debris flows characterize the Middle Comondú, which is mainly composed of volcaniclastic breccia and conglomerates as well as lava flows and ignimbrites (Drake et al. 2017; Hausback 1984; Umhoefer et al. 2001). The Middle Comondú is ~400-750 m thick, making it the thickest Comondú unit. It was likely deposited at ~19-15 Ma (Drake et al. 2017; Umhoefer et al. 2001). The presence of coarse conglomerates implies nearby sources of sediments, suggesting volcanic highlands in the adjacent area. This, along with breccia layers and minor andesite lava flows, is interpreted as the

volcanic arc's westward migration and arrival at the position of present-day Carmen Island (Umhoefer et al. 2001).

The Upper Comondú is dated at ~15-12 Ma (Bryan et al. 2014; Busby et al. 2020; Drake et al. 2017; Ferrari et al. 2018; Umhoefer et al. 2001). Its rocks are generally poorly preserved, suggesting either a lower eruption rate or more exposure to erosion (Drake et al. 2017). Similar to the lower units, the Upper Comondú also contains conglomerates and flow breccias but is dominantly composed of andesite and basaltic andesite lava flows, which suggests local volcanism attributable to the volcanic arc's westward arrival to present-day Baja California (Ferrari et al. 1999; Umhoefer et al. 2001). A series of intrusive rocks found in Loreto area also seems to be associated with the local eruptions that created the Upper Comondú lava flows, based on similar ages (Drake et al. 2017).

Around 16 to 12 Ma, Baja's arc volcanism was progressively extinguished, from north to south (Umhoefer 2011; Umhoefer et al. 2001, 2002), as subduction of Farallon Plate under the North American Plate ceased (Balestrieri et al. 2017; Busby et al. 2020; Duque-Trujillo et al. 2015; Ferrari et al. 2018; Fletcher et al. 2007; Fletcher and Munguía 2000; Oskin and Stock n.d.; Paz Moreno and Demant 1999) . The dominant tectonism transitioned to dextral-oblique extensional faulting, volcanism, and lithospheric thinning, associated with the formation of a continental rift (Bennett and Oskin 2014; Ferrari et al. 2013, 2018; Sawlan 1991; Sutherland et al. 2012). This period of continental rifting and crustal thinning, referred to in this study as the early syn-extensional stage, eventually led to marine incursion associated with formation of the Gulf of California (Balestrieri et al. 2017; Duque-Trujillo et al. 2015; Ferrari et al. 1999, 2018; Umhoefer et al. 2001). Rocks from this period include diverse volcanics, ranging from basalts to andesites and rhyolites (Busby et al. 2020). Some previous studies speculated that the initial

stage of oblique extension might have started in the middle Miocene (Bot et al. 2016; Rossi et al. 2017), while others have argued that a significant portion of continental extension initiated around 12 Ma (Busby et al. 2020; Fletcher and Munguía 2000; Oskin and Stock n.d.; Sutherland et al. 2012).

Some studies (Bennett and Oskin 2014; Oskin et al. 2001; Stock and Hodges 1989) have demonstrated that the Gulf of California underwent two phases of rifting. The early stage consisted of a wide zone that extended orthogonally to the Gulf rift axis, accompanied by dextral shear in the western boundary of Baja California. This was then overprinted from 6 Ma to the present by the oblique transtensional movement between the Pacific and North American Plates, creating the localized oblique-divergent plate boundary in the modern-day Gulf. Alternatively, some workers (Axen and Fletcher 1998; Fletcher and Munguía 2000; Rossi et al. 2017; Sutherland et al. 2012) argued for a one-phase model, in which shear between the Pacific and North American Plates has been present in Gulf of California ever since the cessation of subduction, initiating an oblique extensional plate motion that persists to present day.

The late syn-extensional phase, which refers here to the period when magnetically lineated oceanic crust appeared, spans from 6 Ma to the present day (Busby et al. 2020; Duque-Trujillo et al. 2015; Sutherland et al. 2012; Umhoefer et al. 2002). During this phase, the separation of the Baja California microplate from continental North America was complete, and Baja began migrating northwest as a part of the Pacific Plate (Busby et al. 2020), with NW-SE oblique transtension zone in the middle of the Gulf of California. To the northwest, this system links with the San Andreas transform plate boundary (Lonsdale 1989; Umhoefer et al. 2002). Although most of the strike-slip motion between the Pacific and North American Plate is partitioned by the Gulf's oblique-divergent boundary, a small portion of slip (~10%) is believed

to occur on the Tosco-Abreojos transform fault system to the west of Baja California (Lonsdale 1989).

1.1.2 Isla Monserrate

Isla Monserrate is located in the Gulf of California, ~18 km off the coast of Baja California Sur (see Figure 2). The island has never been systematically mapped, and thus its geological history is not well known. Among the small number of previous studies, most focused on the coastal margin of the island; consequently, little is known about Monserrate's inland geology.

Durham (1950) and Anderson (1950) report on a brief survey of Isla Monserrate during the 1940's Scripps expedition to Gulf of California. Anderson (1950) described the angular unconformity between the steeply east-dipping red-brown volcanics, presumably describing Comondú rocks, and overlying sedimentary layers. Anderson described the base of sedimentary unit as composed of a conglomerate layer overlain by limestone. Anderson (1950) also described a flat erosional surface covered by poorly consolidated gravels with well-preserved fossils, forming a terrace surface (Figures 52, 53, 63). These terraces were interpreted to have been offset by faults, suggesting several hundred feet of displacement that elevated some of the gravel surfaces to the high (~200 m) elevation plateaus. The same study also noted the existence of low-elevation terraces along the coast of Isla Monserrate, cut into both volcanic (Comondú) and limestone units. Durham (1950) described macro-invertebrate marine fossils on the island, listing corals, gastropods, and seashell species. He concluded the limestone to be roughly middle Pliocene in age, with overlying gravels to be Pleistocene.

Johnson (2014; a lay guidebook) described visits to Isla Monserrate that included access to the high-elevation plateaus and northern coastlines that were not visited by Durham or Anderson. The description of the island's general geology in Johnson (2014) mostly agrees with that of Anderson (1950); the island's lowest rocks are Comondú volcanics, steeply tilted to the east. Younger sedimentary rocks overlie the Comondú across an angular unconformity. The overlying deposits are characterized as having a conglomerate base and fossiliferous composition. On top of these deposits lie carbonate rocks and loose gravels above an angular unconformity, forming coastal terraces. Johnson (2014) hypothesized these terrace surfaces to be offset by multiple faults.

Carreño et al. (2015) examined fossiliferous orange marlstones found on low-elevation portions of northwestern and southwestern Isla Monserrate, which yielded macro- and micro-fossil marine invertebrates. Based on biostratigraphy, Carreño et al. (2015) placed the orange marlstones at roughly 5 to 3 Ma in age. The study also suggested that the assemblages record a shallow "Proto-Gulf" bathymetry influenced by upwelling deep waters, characterized by low-oxygen and nutrient-rich conditions. According to the study, the island might have been located in the tidal-mixing upwelling zone near the tip of the "Proto-Gulf", much like the present-day northern Gulf of California (Helenes, Carreño, and Carrillo 2009). Other studies (Martínez and Yanet 2019; Vázquez et al. 2007) have instead favored a deeper water depositional environment rather than a shallow one. The evidence for the deeper water deposition includes (1) the presence of armored mudballs, which can indicate gravity-induced flow in a deeper underwater ramp (Vázquez et al. 2007), and (2) re-evaluation of benthic fauna in marlstones that indicate upper middle bathyal depths at ~500-1500 m (Martínez and Yanet 2019; McDougall 2009).

1.1.3 Coastal Terraces

Coastal terraces are planar landforms typically created by marine physical and biological erosion, created near sea level and then subsequently uplifted. These features are created when waves erode bedrock and shallow marine organisms help cut bioabrasional platforms (Anderson, Densmore, and Ellis 1999; Kelsey 2015). Coastal terraces provide important information about sea-level changes or vertical tectonic motion (Dietz 1963; Keller and Pinter 2002; Kelsey 2015). During interglacial periods (e.g. Marine Isotope Stages MIS 5, 7, etc.), sea-level highstands carved coastal terrace levels which were then slowly uplifted during glacial periods of low sea level (Anderson et al. 1999; Kelsey 2015). Modern elevations of Pleistocene coastal terraces can be used to analyze the local uplift history (Keller and Pinter 2002; Oretsky 2020).

Coastal terrace platforms can be distinguished from other flat geomorphic surfaces by shallow-marine sediments preserved on the wave-cut platform. The line of intersection between the bioabrasional platform of a terrace and the associated sea cliff is called a shoreline angle, which marks the farthest advance of erosion, typically, the highest sea level during a highstand (Scott and Pinter 2003). The shoreline angle associated with an inactive and uplifted coastal terrace and its paleo sea cliff is called a Paleo Shoreline Angle (PSA). Often, uplifted terrace platforms are covered by colluvium transported from higher topography and can cover the PSA (Scott and Pinter 2003). The true maximum elevation of an uplifted coastal terrace is the elevation of its PSA, so this feature must be exposed in outcrop and rigorously measured for quantitative studies (Dietz 1963).

Chapter 2. Methods

2.1. Field Mapping

The geology of Isla Monserrate was explored and mapped during three field expeditions that included five cumulative weeks of work. Field work focused on investigating lithological units, geological structures, fossil evidence, and geomorphological features. These field observations were augmented by aerial drone surveys that yielded a high-resolution orthomosaic map and, through structure-from-motion, a Digital Elevation Model (DEM) with 16.1 cm average pixel resolution. The data gathered by drone were then compiled by the program Pix4D Mapper, which served as a basemap and provided a DEM for 3D geological mapping and analyses using ArcGIS Pro.

2.1.1. Geology

The lithology of Isla Monserrate was mapped in the field based on color, lithic content and phenocryst composition, matrix composition, sedimentary textures, fossil assemblages, post-depositional deformation, etc. Based on the field and thin-section observations, five rock packages were identified on Isla Monserrate:

1. pre-extensional undifferentiated Comondú volcaniclastics (not further differentiated in this study),
2. early syn-extensional pyroclastics,
3. early syn-extensional Pliocene marine sedimentary rocks,
4. late syn-extensional littoral terrace-capping sediments, and recent Quaternary sediments.

Structural measurements were taken on features such as bedding planes, fault planes, fault lineations, and flow indicators. Each measurement's location was measured with GPS and plotted on a basemap. The measurements were analyzed using software such as Stereogram and Faultkin 8 (Allmendinger, 2018) to assess the island's extensional, rotational, and folding pattern.

2.1.2. Terraces

Uplifted coastal terraces can be crudely mapped based on their morphology and more precisely using shoreline platforms and terrace-capped sediments exposed in outcrop. Different terrace levels on Isla Monserrate were identified and mapped based on field observations and 3D mapping of the drone-based DEM and orthoimage using ArcGIS. The isolated high-elevation plateaus on the island required quantitative analysis of elevation distributions. For the terrace elevation distribution analysis, plateau surfaces were divided into 5x5 m grids, with the center point of each grid assigned an elevation value from the DEM. The frequency distribution of the resulting 20,971 elevation points was analyzed to assess the number and distribution of plateau levels.

In addition, this study analyzed the alignment of projected plateau surfaces (Figures 9 to 16). Elevation profiles, based on drone generated DEM, were plotted for different pairs of plateaus (e.g., elevation profiles between Plateau 3 and 4, 5 and 6, etc.) with surface elevation as the y axis and straight-line distance as the x axis. Best-fit lines were then drawn on plateau surfaces, which were extended and projected to other surfaces, to assess whether the pair of plateau surfaces align. Those with clear alignment were deemed likely to belong to the same terrace level; the plateaus with poor alignment likely to be of separate levels. This was a

qualitative method to categorize the plateau levels, as quantifying the degree of surface alignment was not available within the scope of this study.

Outcrop exposures of paleo shoreline angles (PSAs) are required to measure true terrace elevation. PSA locations were identified in the field, with horizontal coordinates measured using a handheld GPS. These PSA stations were later geolocated on ArcGIS using outcrop photos and GPS coordinates, where each PSA station's vertical elevation was estimated based on drone-generated DEM of each location (Figure 6). A few PSA locations on older terraces, where bedrock is well exposed with little to no surface sediments, were identified following field work based on drone orthoimagery and a DEM generated ArcGIS 3D map. On this remote imagery, PSA locations were identifiable based on the changes in slope. These PSA locations were estimates, limited by the uncertainty in horizontal coordinates derived from a hand-held GPS receiver and by the accuracy and precision limitations of the drone-based DEM.

2.2. Sample Analyses

Multiple samples were collected from various sources (shown as red dots in Figure 2; sample site numbers listed in Table 1) during field work, including igneous rocks, sediments and sedimentary rocks, and fossils. Samples of silicic tuff, Comondú lava, and dikes were retrieved for geochemistry and geochronology analysis. Fossil corals, marine macroinvertebrate fossils, and carbonates were retrieved for biogeochronology and paleo environment analysis. All samples were cut into thin sections to assess the compositions and conditions of phenocrysts, lithic fragments, carbonate grains, and fossils using photomicrography.

2.2.1. Petrographic Analyses

For geochemistry, X-Ray Fluorescence Spectroscopy and Inductively Coupled Mass Spectroscopy (ICP-MS) whole-rock major-and trace-element analyses (Figure 42) on five samples were conducted at the Washington State University GeoAnalytical Laboratory using a Thermo-ARL XRF and Agilent 7700 ICPMS. One sample was sent to Teresa Orozco at UNAM for $^{40}Ar/^{39}Ar$ analysis on amphibole phenocrysts to establish geochronology, using a 20 W Ar-ion laser for gas extraction and Isotope NGX multi-collector noble gas mass spectrometer (Figure 43). $^{40}Ar/^{39}Ar$ geochronology and major- and trace-element geochemistry was funded by NSF EAR 1921182 to Putirka and Busby.

2.2.2. Paleontological Analyses

Macro-invertebrate fossils were examined by Charles L. Powell, II (United States Geological Survey, Emeritus [USGS]), who identified macrofossil taxa from photographs taken in the lab and the field. The temporal range of each species was determined from published literature to aid in establishing the biostratigraphic ranges and paleo-environments (Table 2). Sediment samples containing microfossils were sent to Dr. Kristin McDougall (USGS). Samples were processed and examined to determine sample age and environment based on foraminifers. The foraminiferal samples were processed with solvent (kerosene) and Quaternary-O, washed through a 63 μm mesh screen, and dried at low temperatures (< 40 C). The entire ≥150 μm fraction or a known split obtained using a microsplitter was picked for foraminifers, and the presence of fragments, planktic foraminifers and other organic remains (radiolarians, diatoms, ostracodes, and fish debris) was noted. Foraminiferal slides and residues are on file at the U.S. Geological Survey Micropaleontology Laboratory in Flagstaff, Arizona.

Chapter 3. Pre-Extensional Rocks and Structures

Rocks of Isla Monserrate are dominantly volcanic and volcaniclastic, overlain by latest Pliocene and Quaternary sedimentary deposits. Volcanic units consist of meters to tens-of-meters thick beds of basaltic andesite lavas and volcaniclastic debris-flow deposits, together comprising a near kilometer thick sequence. These rocks are stratigraphically the lowest lithological group on the island, forming a local basement to other overlying rocks units. Structurally, these volcanic strata dip steeply to the east at ~50-70°, with little angular difference between each layer or fault block (Figures 2, 22, 23).

3.1. Debris-Flows

Volcaniclastic debris-flow deposits are some of the most prevalent and diverse lithologic units within the Comondú on Monserrate. The clasts in debris-flow units are poorly sorted, ranging from pebbles to boulders (Figures 25, 26), with grain shape varying between angular and rounded. The clast compositions also vary (Figures 25, 26, 27), including tuff, breccia consisting of older lahars, sandstones, and andesites, listed in the order of increasing prevalence.

Lahar deposits on Monserrate are typically massive, and crude layering is distinguishable. The matrix of lahar deposits is moderately to well lithified, very poorly sorted, and composed of medium- to coarse-grained sand. The lahar sands are typically reddish brown (Figure 25), but some deposits with yellowish-brown sand matrix are found along the eastern shore of Isla Monserrate (Figure 26).

Fluvial sandstone beds (Figures 28, 29) were also found interbedded with the debris-flow deposits. The depositional contacts between the two lithologies can be gradational but are

typically sharp and conformable (Figure 28). These fluvial layers usually exhibit moderately to strong laminations. Some of the sandstone beds have mud/silt layers draped over planar laminations. The colors of the fluvial units are typically identical to the lahars they are interbedded with; red lahars are interbedded with red sandstones, and yellow lahars are interbedded with yellow sandstones (Figures 28, 29).

At least one reddish brown fluvial sandstone that crops out on the southeast Monserrate coast preserves flow indicators (Figure 30). Some of these are multiple linear depressions on the depositional surface with nearly parallel trends. These depressions are interpreted as bounce marks, created by saltating clasts bouncing along the riverbed and deforming the floor's soft sediments. Fluvial scour marks have U-shaped scour holes around the obstacle and streamlined tails with sediment ridge downstream (Várkonyiv and Hargitai 2021). In this (Figure 30 left) outcrop, the obstacles are pebble- and cobble-sized siliciclastic grains, which were either half buried or sitting on the floor, obstructing the current flow and scouring the soft sediments around them. The fluvial scour marks show two slightly different trends of 246° and 206°. When the bedding plane is rotated back to horizontal, the initial flow directions trend 244° and 202°.

Signs of biological activity preserved in the fluvial sandstones are rare. So far, the field survey has revealed only one set of trace fossils within the Comondú; possible burrows and worm traces preserved on a yellow sandstone outcrop on the southeast coast (Figure 31).

3.2. Lava Flows

Lavas (Figures 32, 33, 34, 35, 36) exposed on Isla Monserrate are interbedded with debris-flow layers and can vary from a few meters to tens of meters in thickness. Contacts between lava units and debris-flow deposits are parallel to the bedding of the lahar deposits and

associated fluvial sandstones. Basal contacts of lava flows show a thin chilled margin, and the lavas sometimes contain detached clasts from the underlying deposits (Figure 32). The upper contacts are irregular and lack chilled margins (Figure 33). The phenocryst and groundmass compositions vary greatly between different basaltic layers. Based on porphyroclast compositions described in the field, the Monserrate Comondú lavas were roughly classified into: hornblende porphyry and plagioclase porphyry (Figures 34, 35, 36).

Hornblende porphyry lavas on Isla Monserrate (Figure 34) exhibit light grey to greenish grey colors, intermediate in Color Index (Panchuk 2019). Thin-section analysis reveals 10% amphibole phenocrysts and light grey aphanitic groundmass. Amphiboles are typically spheroidal, around 1 mm in diameter, but occasionally were elongated and ranged up to approximately 3 mm in length.

Plagioclase porphyry lavas (Figure 35) exhibit darker colors of the groundmass, ranging from darker grey to dark reddish grey. The plagioclase porphyroclasts are elongate, with large grains reaching up to ~5-7 mm (Figure 37 A). Thin-section analysis under cross-polarized light revealed fine-grained plagioclase phenocrysts making up ~30-40% of the whole-rock composition (Figure 37). Some outcrops contained only very fine-grained plagioclase phenocrysts, making up ~40-50% of the overall composition, with little to no visible plagioclase porphyroclasts (Figre 37 C). Thin-section analysis also revealed that these lavas contain 10% clionopyroxene phenocrysts with high birefringence (Figure 37 B). Locally, many of these outcrops have rounded spheroid vugs filled with secondary mineral growth, predominantly plagioclase, ranging ~3-5 cm in diameter (Figure 36). In a few zones, these vugs are elongate, creating a zone of lineated fabric (Figure 36).

Geochemistry analysis reveals relatively high (6-8%) alkali composition. Total alkali vs silica plot (Figure 42) places the Monserrate lavas within trachyandesite (ISMON 23-D18 S8) and basaltic trachyandesite (ISMON 23-D18 S5).

3.3. Discussion

No numerical ages have yet been obtained from the volcanic units on Isla Monserrate, which permits multiple interpretations. For example, it has been suggested that the Monserrate volcanics might be syn-extensional, as post-subduction-age lavas could look identical to the Comondú arc lavas in the field (Busby et al. 2020; Graettinger et al. in press). Alternatively, I argue that the Monserrate volcanic strata were emplaced prior to extension. This is based on the homogeneity of volcanic layering orientations (Figure 22), even across different fault blocks, suggesting these rocks were deposited before the onset of extensional rotation. The radiometric dating of overlying pyroclastic deposits, which is further discussed in the later chapter, supports the latter conclusion: ~16 Ma age of syn-extensional pyroclastics implies the underlying deposits must be older, confirming the Monserrate volcanic units as a part of the Comondú Group.

The lithology of pre-extension Monserrate volcanics vary significantly, each with different phenocryst and groundmass compositions, much like the Comondú volcanics found on the Baja mainland. Such lithological diversity also applies to the volcaniclastic units, in terms of matrix and clast compositions. The differing sand lithologies imply multiple depositional events with heterogenous sediment sources. The clast compositions also vary widely, including lithics that are not found among the exposed Monserrate units. One example is a debris-flow deposits containing tuffaceous rocks and other types of lithics that are not found within pre-extensional Monserrate sequence (Figure 27), suggesting that the Comondú debris flows on Isla Monserrate

were far-traveled. The NE-SW trending paleo-flow directions suggest that much of the sediments likely originated from the subduction arc located to the east/northeast. This coincides with the current understanding on the formation of the Comondú Group (Busby et al. 2020; Drake et al. 2017; Ferrari et al. 2013, 2018; Graettinger et al. in press; Umhoefer et al. 2001), which concludes that the volcanic/volcaniclastic materials were shed from the active volcanic arc highlands to the east.

Chapter 4. Early-Stage Syn-Extension

The syn-extension phase of Isla Monserrate refers to the period of active extension that dominated local tectonism. In this study, this phase is divided into two stages: early and late syn-extension, where the former interpreted as the period of lithospheric thinning and subsidence, and latter to uplift. Isla Monserrate's extension is a local expression of regional extension that thinned and ruptured Baja California Microplate (BCM), separating it from mainland North America. Present-day extension continues, as transtensional oblique rifting is still active in the middle of the Gulf Extensional Province (GEP), producing oceanic crust and continuing seafloor spreading.

The early syn-extension phase on Isla Monserrate spans the period of active extensions that rotated and thinned the crust, eventually leading to submergence of the surface below sea level. The phase is recorded by a series of detachment fault systems, pyroclastic units, and marine deposition varying from shallow to deep, all of which show signs of progressive rotation within the extensional regime.

4.1. Faults

Isla Monserrate features numerous fault systems that deformed and offset the lithological units (Figures 2, 18, 19, 24, 57, 58, 59, 60). These faults are mostly extensional, ranging from

low-angle detachment faults with multiple cores (Figures 57) to high-angle normal faults with lesser displacement (Figures 58, 59). Associated with these extensional faults are progressive rotation of bedding, as shown by dip change from older to younger lithological units (Figures 22, 23). In addition, at least one reverse fault was observed at the southern tip of Plateau 2 (Figures 2, 18, 19).

4.1.1. Detachment Faults

Three low-angle detachment fault systems have been mapped on Isla Monserrate. They have curvilinear traces that suggest megamullion structures and generally strike NNW-SSE and dip 25~30° down to the west. These three systems can be traced along the (1) western margin, (2) central, and (3) eastern margin of the island (Figures 2, 24) and are referred to here as the Eastern Monserrate Detachment (EMD), Central Monserrate Detachment (CMD), and Western Monserrate Detachment (WMD), respectively. Each detachment system is found with multiple fault cores coupled with secondary fracture fabrics and damage zones containing fault breccia, gouge, cataclasites, etc. Because internal units within the Comondú Group have not been differentiated, and because detachment fault cores have only been found within the Comondú, this study could not characterize offset magnitude. Nonetheless, the amount of displacement could be estimated (Axen 1988) based on horizontal distance between each fault at ~1km (Figure 2), fault dip at ~30°W, and Comondú bed dip at ~60°E. Using these values and a law of cosine gives us ~850 meters of displacement.

Each detachment system is associated with a subsided basin developed on the west (hanging wall) side of the fault (Figures 2, 8). These basins are filled with syn-extensional pyroclastic deposits and/or marine sediments and show systematic variation in size between

different detachment fault systems. Among the three, the EMD is associated with the smallest basin (~0.18 km^2), with only small amounts of pyroclastic and marine sediments deposited on the hanging wall of the fault. The CMD has a few basins developed along the northern fault, filled by Plateau 2's trachydacite tuff and carbonates, and a small section of Pliocene sequence exposure along the northern beach. The WMD is associated with the largest (~1.98 km^2) and most laterally continuous basin, with the thickest deposits of both pyroclastics and Pliocene sediments.

Measured slip vector trends on these detachment faults vary slightly by system and by regional domains (Figure 24). In most cases, striae on low-angle normal fault planes range between WNW to WSW. In a few localities, such as the northern section of the EMD, S- to SSE-trending striae can be observed (Figure 2). At least one of the fault cores of the EMD is associated with several slip vectors within one fault plane.

4.1.2. High-Angle Normal Faults

Isla Monserrate has higher-angle (~50-75°) normal faults that are likely younger than the detachment faults. The orientations of these high-angle normal faults vary less than those of low-angle faults, as they generally dip down to the WNW or WSW (Figure 2, 58, 59). Lineations of striae on fault planes generally trend W and WSW.

Most of the high-angle normal faults are found within shallow-dipping(~15-25°E) Pliocene marine beds. Locally, these normal faults form contacts between Pliocene deposits and the Comondú, where the former unit composes the hanging wall and the latter the foot wall (Figure 58). Notably, while the faults cross-cut Pliocene deposits and low-angle detachment cores, they do not offset presumed Late Quaternary terrace sediments.

In the field, some marker beds are distinguishable via higher resistance and/or different colors (Figure 59). Displacements were estimated using offset of these marker beds. The high-angle normal faults show less offset than the detachment faults, varying between <1 m to ~3 m. These marker beds also show drag folds developed on both the hanging walls and foot walls of some faults.

Neptunian/clastic dikes, which are clastic deposits filling fissures formed by fault activity (Lehner 1991; Smart et al. 1988), were found on Isla Monserrate adjacent to the high-angle normal faults in the Pliocene marine deposits. They are recognized from vertical, sheet-like bodies cutting through the horizontally bedded sediments (Figure 60). These clastic dikes tended to be more resistant to erosion than surrounding deposits. The dikes were infilled by the same yellow fine-grained sediments as the Pliocene sequence.

One outcrop in the northwestern corner of the island exposes a contact of Pliocene sediments overlying Comondú volcanics. The Comondú basement is cut with a few fissures, which are filled with yellow and fine-grained sediments identical to the marlstones. The underlying Comondú volcanics and volcaniclastics are dominantly reddish-brown to dark grey and can be ruled out as the possible source of these sediments. These fissure-filling sediments exhibit horizontal fabric, implying that the fissures were filled via soft sediment deposition rather than injection from a lithified source.

4.1.3. Reverse Fault at Plateau 2 Tuff Outcrop

Plateau 2 is cut by a reverse fault that strikes N-S and dips down to the east (Figure 18, 19). Its displacement can be estimated by the offset of basal tuff bed, at ~6 m. This fault strand does not seem to cross-cut Pliocene carbonates that overlie the tuff deposits, which is further

supported by the fact that the hanging wall carbonates are lower than the foot wall carbonates. Measurements of the fault plane and striations average strike and dip of 6°/73°, and trend and plunge of 129°/53°.

4.2. Intrusions

Dikes and other intrusive bodies in the Comondú were mapped throughout Isla Monserrate (Figures 2, 57). They are distinguishable from the Comondú volcanics due to their colors, orientations, cross-cutting relationship, injection into surrounding rock units, lack of flow breccia, and chilled margins. Dike colors tend to be reddish brown to greenish yellow, in contrast to the dark brown and grey colors typical of Comondú volcanic flows (Figure 57). Dike textures are aphanitic-porphyritic, with ~3-4 mm phenocrysts that show signs of heavy alterations. The thin section examination reveals compositions of ~10% hornblende and ~20% plagioclase phenocryst. These intrusive bodies predominantly dip down to the west, unlike the Comondú flows that dip steeply to the east. Consequently, dikes crosscut the older Comondú layers, sometimes injecting into them. The contact boundaries between the intrusive cores and the wall rocks lack flow breccias, and instead exhibit chilled margins.

Many of the dikes on Isla Monserrate are emplaced within fault cores, with orientations similar to the fault planes (Figure 57). In at least two localities, the dikes are truncated by detachment faults, one with ~1 m offset and the other with ~15-20 m offset.

4.3. Early-Stage Extensional Pyroclastic units

The lowermost unit of the early Monserrate syn-extensional sequence consists of pyroclastic deposits, including welded ignimbrite flows and moderately lithified silicic tuff beds.

Most of these outcrops are in the northern part of the island, particularly the northwest corner of the island, and along the ridges of Plateau 2 (Figure 2). Notably, all pyroclastic units on the island are located on the hanging walls of detachment fault systems (Figures 2, 8). Stratigraphically, these pyroclastic deposits overlie the Comondú Group and underlie Pliocene carbonates, with angular unconformities at both contacts. In almost all localities, the pyroclastic deposits dip to the east with a gentler tilt than the Comondú. Some outcrops, as will be described in more detail, record signs of internal angular unconformities, together forming a fanning-dip sequence. Many of the pyroclastic rocks also contain an abundance of fresh phenocrysts, making them a valuable unit for establishing geochemistry and geochronology.

4.3.1. Ignimbrite Flow Deposits

Ignimbrite flow deposits (Figure 38) are found along the northwest coast of the island and likely form the basal unit within the pyroclastic sequence. Notably, these ignimbrite flow deposits are only found in the WMD fault basin, as the basal unit of the CMD and EMD basin pyroclastics are tuff beds. The ignimbrite deposits are welded and contain distinctive dark brown flow bandings. The flow bandings dip ~80-90°. The color varies widely from outcrop to outcrop, including light grey with pink hues and red and purple colors. Based on field observations, these deposits contain little to no lithic fragments and ~40% coarse phenocrysts, ~90% of which are plagioclase and ~10% amphiboles.

4.3.2. Tuff Deposits

Tuff deposits are typically well stratified, moderately lithified, contain lithic clasts and phenocrysts, and lack flow bandings (Figure 39). Their colors range from pink to tan-white,

probably due to varying degrees of weathering and oxidation. The true thickness of these deposits can only be approximated, but are at least 30 m. These tuff units generally dip to the east at ~35-45°, with the eastern hillside of Plateau 2 (Figure 3) being the only exception (Figures 18, 19). The tuffs are most abundant along Monserrate's northwest corner and underneath the carbonate outcrops of Plateau 2 (Figure 2).

The tuff deposits that outcrop along the northwest coast of Monserrate (Figure 2) are perhaps the most voluminous on the island. These deposits are well lithified, medium to well stratified, and reddish brown to pink in color. Visual examination suggested few lithic fragments and ~30-40% phenocrysts, most of which consist of plagioclase and few red hornblendes. Thin-section analysis revealed plagioclase, hornblendes, and resorbed quartz (Figure 41). Plagioclase crystals are relatively fresh and average ~3-5 mm in diameter. Amphibole phenocrysts tend to be smaller, ~0.5-1 mm, and are more weathered, with opaque minerals developing on the rims or replacing them completely. There is a trace amount of heavily resorbed quartz, which are embayed and average ~2 mm in diameter.

11 samples were retrieved from tuff outcrops (Figure 2, Table 1). Of these, three were sent for geochemical analysis, and one sample, ISMON 22-2, was sent for geochronology ($^{40}Ar/^{39}Ar$). The results are as follows.

XRF geochemistry analyses (Figure 42) of tuff samples (Sample Sites 1, 35, and 39 on Figure 2) reveal normalized values of ~65% silicates and ~8% alkalic composition, making the Monserrate tuff a trachydacite. $^{40}Ar/^{39}Ar$ dating was conducted using hornblendes in sample ISMON 22-2 (Site 1 on Figure 2) and yielded a well-defined age of 15.849 ± 0.062 Ma (1σ) (Figure 43) (Orozoco, written communication).

Based on the ~16 Ma age of trachydacite tuffs from Isla Monserrate, the pyroclastic units should be classified as a part of the Upper Comondú Group. However, this study described these pyroclastic units as separate from the underlying pre-extensional Comondú due to: 1) distinct lithological differences; 2) deposition during a different local tectonic setting, i.e. syn-extensional vs. pre-extensional.

4.3.2.1. Fanning Dip Outcrop

At Plateau 2, a large deposit of tuff underlies carbonate beds across an angular unconformity. The western side of the plateau exposes tuff dipping east at ~35-45° (Figures 18, 19), but the eastern hillside exposes a west-dipping and steepening-upward sequence of tuff deposits, consisting internally of three to four ~5-10 m-thick packages (Figures 21, 40). Within the same package, tuff layers show parallel bedding with little or no lateral change in thickness.

The basal unit in this sequence is at least ~4-5 m thick, and contains rounded and angular Comondú volcanic clasts, making it a tuff breccia (Figures 21, 39). It dips ~12° to the west and forms the depositional contact with the underlying Comondú. The beds are normally graded, with large Comondú fragments most abundant at the base (Figure 21). Thin-section analysis reveals the composition to be 60~70% lithic fragments with a few fresh phenocrysts of biotite, hornblende, and plagioclase.

Higher portions of the tuff sequence, including individual beds, are normally graded, as lithic clasts become finer and rarer upwards (Figure 21). The matrix of these upper strata tuff is tan-white to light brown in color, although some of the outcrops exhibit green hues within the volcanic ash matrix and on the surface of lithic clasts. Thin-section analysis of a sample collected from one of the upper layers shows a composition of ~10% lithic fragments of Comondú

volcanics and ~20% phenocrysts. About half of these phenocrysts are amphiboles, and the other half plagioclase, with a few biotites. The size of amphibole phenocrysts ranges up to 5.5 mm in diameter. Plagioclase phenocrysts rarely exceed 2 mm and feature well developed twinning in many grains.

The uppermost tuff package dips down to the west at 32°, the steepest of any layers in the tuff sequence (Figures 18, 21). These deposits contain little to no lithic clasts, consisting instead of almost pure ash groundmass and phenocrysts. The ash matrix is pale white, and amphibole phenocrysts are lighter brown in color, contrasting with the black amphiboles that predominate in the lower strata. Thin-section analysis (Figure 41) reveals a matrix with vitroclastic texture, containing relict glass shards. Phenocrysts are fresh, perhaps the least altered among all tuff samples. Phenocrysts are mostly amphiboles and plagioclase, lacking biotites or other mafic minerals. Amphiboles make up ~10% of the composition, range up to 6-7 mm in diameter, and exhibit light greenish brown to dark reddish-brown color. Plagioclase represents ~10% of the composition, averaging ~1-2 mm in diameter.

4.4. Submergent Marine Sedimentary Units

Overlying the pre-extensional Comondú outcrops and syn-rift tuffaceous deposits are marine sedimentary deposits that include conglomerates, marlstones, and fossiliferous limestones (Figures 44, 45, 46, 47, 48, 49, 50). Despite local compositional variations, most of these deposits share a distinctive yellow color unless they are heavily weathered. These marine sedimentary units dip at an average of ~10-25° and locally overlie the Comondú units across an angular unconformity. These sedimentary deposits are most prevalent along the northwest and southwest coast of Monserrate and at the island interior plateaus. Based on their locations, the

marine deposits show differences in lithology, thickness, bedding orientation, and fossil assemblages. Therefore, this study has grouped these deposits into two tentative categories: coastal and high-elevation outcrops.

4.4.1. Coastal Deposits

Marine sedimentary deposits exposed near the present coast of Isla Monserrate are composed of basal conglomerates overlain by distinctive yellow marlstones and fossiliferous limestones. These deposits locally overlie Comondú bedrock, across both fault and depositional contacts. The depositional contacts include a local buttress unconformity, recording significant topographic relief at the onset of deposition. Over this buttress unconformity, the basal sedimentary deposits include brecciated boulder clasts (Figure 45). In other locations, basal marine deposits are typically consisted of finer, rounded gravel layer (Figure 44).

Basal conglomerates (Figure 44) are poorly stratified, and their thickness is roughly 3-4 meters. The clasts are well-rounded and poorly sorted, with average textures ranging between cobble and pebble sizes. The clasts are primarily composed of the Comondú volcaniclastics and syn-rift tuffaceous unit, suggesting a local origin. The overall framework is grain supported, and the matrix is made of yellow silty sediments, similar to the yellow grains of overlying marlstones.

The overlying marlstone deposits (Figure 47) have a yellowish-orange color. They are most common at lower elevations, especially along the northwest and southwest coasts of the island. They are the thickest unit of the marine sedimentary units, reaching 60 m or more (Vázquez et al. 2007). These deposits are moderately to well bedded, dipping at ~15-25°. Deposits near the north coast dip down to the northeast, versus the southern coast outcrops that

dip down to the southeast. Vázquez et al. (2007) also noted these divergent dips. The marlstones are typically poorly lithified and are weaker than the more durable Comondú fluvial sediments. Marlstone grains are well sorted, generally silt to very fine-grained. Thin-section examination (Figure 51) reveals roughly 80% allochems, which are dominantly made of hollow skeletal remains of various marine microfossils such as benthic and planktonic foraminifers, calcareous nanoplanktons, and ostracods (Appendix I). The matrix is made of unconsolidated micrite mud with orange-brown hue, which is probably responsible for the marlstones' yellowish-orange color. The facies contain few siliciclastic grains, with plagioclase, hornblende, and biotite crystal fragments making up only ~1-2% of the whole rock. The overall structure is grain-supported, making these facies packstones according to the carbonate textural classification of Dunham (1962).

Interbedded with the marlstones are local and discontinuous marine invertebrate fossiliferous layers (Figures 48, 49). The contacts between the fossiliferous beds and marlstones are gradational, as fossil concentration changes gradually from layer to layer. Some of these beds can have up to 90% fossil composition, effectively making them coquinas (Figure 48). The sediments of these fossil-rich beds, or biostrome layers, often lack well defined bedding, except as defined by layering of fossil fragments themselves.

The fossils in these biostrome layers are typically well preserved, disarticulated but rarely fragmented, and are made of marine invertebrate skeletal remains. The shell sizes average around 5-8 cm in diameter, but some large specimens range up to ~13 cm. They are predominantly bivalves, such as *Argopecten abietis, Argopecten percarus, Lyropecten subnodosus, and Patinopecten bakeri* (Table 2). Based on the species list identified by Charles Powell, the age ranges of the identified species suggest an age range of ~5.3-3.6 Ma (Table 2). The matrix of

these shell-rich layers is yellow marl, mixed with coarse, poorly sorted, subangular to subrounded rhodolith fragments (Figure 46).

Several of the shell-rich beds, especially on the southwest coast and the northwestern coast of Isla Monserrate, include features resembling armored mudballs. These features were observed by Johnson (2014) and Vázquez et al. (2007), who described them as "spherical structures composed of disarticulated fossil shells, arranged in multiple layers of part-radial and part-tangential circles, bound by fine-grained sediment matrix." The mudballs observed in this study are smaller than the ones described in the previous studies, generally ~10-20 cm in diameter (Figure 49).

Two samples of coastal marlstone were collected for microfossil analysis: ISMON SEPT 23 D18 S3 and D18 S4 (Figure 2, Table 1). The microfossil analyses by McDougall suggest paleo depositional environments and ages and are reported in Appendix I. The presence of foraminifera *Galliherina uvigerinaformis* suggests an age correlation to the Carmen Formation section studied by Carreño et al. (2015), and revised by Martínez and Yanet (2019), to be Late Miocene to Early Pliocene, specifically ~5.8-5.2 Ma. Based on this correlation, this study will use Carmen Formation interchangeably with the syn-extensional Monserrate marine deposits. The foraminiferal samples from Monserrate are interpreted here as deposition at depths of ~700-1000 m, and that some of the materials may have been transported downslope from the adjacent shelf. More details are provided in Appendix I.

4.4.2. High-Elevation Deposits

Much of the island's elevated surfaces, such as higher levels of coastal terraces, are covered with tan-white to grey, indurated carbonates that lack laminations and lithic clasts

(Figure 55). These carbonate caps are extensively recrystalized, but locally contain invertebrate fossils and rhodoliths in a micrite matrix. The fossils in these carbonates are heavily leached, sometimes leaving only mold or cast impressions (Figure 50). These grey, indurated carbonates are exclusively found atop the higher marine terraces and deposits, but rarely on Comondú bedrock (Figure 52). The carbonates show strong signs of carbonate weathering, such as jagged surfaces and dissolution pits and joints, immature flank margin caves, and pit caves (Figures 54, 55, 56). These weathering features are more intense and more common on the high-level terraces than on low-elevation terraces.

The contact between indurated carbonates and underlying, less recrystalized and less cemented marlstones is gradational, with variational depth. Where the marlstone is exposed, a lateral, gradual transition from soft marlstones to indurated carbonates is common, as shown in Figure 54 outcrop. This outcrop also illustrates internal bedding in the marlstone that extends laterally into indurated carbonate.

Plateaus form the highest topographical features of Isla Monserrate, which are typically covered in recrystallized carbonates. These carbonates are typically tan-white to light grey, and show signs of heavy weathering. Thickness of the plateau carbonates typically range within a few meters, but locally can thicken to ~15 m or thin out completely, exposing the underlying Comondú bedrock (Figure 55). Unlike the buttress unconformity contact found near the coast, the plateau carbonates and the underlying Comondú units form nearly planar contact (Figure 55). These contacts are often tilted down to the east, which gives plateau carbonates a wedge-like shape that thins out to the west. The contacts are typically overlain by a thin (up to 0.5m) conglomeratic basal layer. The clasts of the basal conglomerates are significantly finer than their

lower elevation counterparts, ranging between granules to pebble-sized, with a few clasts reaching cobble size.

Instead of silty unconsolidated marlstones, the elevated plateaus' carbonate facies above the basal conglomerates are made of indurated fossiliferous limestones and coarse rhodolith wackestones (Figures 56). The fossil assemblages consist predominantly of pectenids, along with oysters and echinoderms. Some of the identified species include *Argopecten mendenhalli, Argopecten revellei, Nodipecten subnodosus*, and *Clypeaster bowersi* (Table 2). Charles Powell's identifications and paleobiodatabase age ranges suggest an age of ~5.3-2.58 Ma. Most of the skeletal remains are disarticulated and moderately to poorly layered (Figure 56). Some outcrops exhibit very well-preserved fossils, whereas others show significant leaching that is more intense in the lower layers, whereas higher fossils are sometimes better preserved.

Microfossil analysis (Appendix I) of five samples from the plateau carbonates reveal they are Late Miocene to Early Pliocene in age, coeval to the coastal marlstones of Carmen Formation. Samples from Plateau 2A are dominated by *Amphistegina gibbosa*, typical of a warm, shallow reef environment. Although Plateau 7 samples are dominated by A. gibbosa, they contain other benthic foraminifers with inner neritic and upper bathyal depths, suggesting that deposition occurred at outer neritic depths (50-150 m). This evidence, along with the low number of planktic foraminifers present in these samples, suggests the depositional environment of Plateau 7 was likely a carbonate shelf edge or proximal to it. Detailed foraminiferal information is reported in Appendix I.

4.5. Progressive Rotation

Monserrate lithological units show progressive rotation from the oldest to youngest (Figures 22, 23). As mentioned in the previous chapter, Comondú rocks are most steeply tilted, dipping ~50-70°E. The overlying pyroclastic units dip ~25-40°E. The only exception is the nearly ~80-90° dipping ignimbrite outcrop on the west coast, but these flow banding orientations likely do not represent the original depositional horizon. The fanning dips within the tuff sequence underneath Plateau 2B is consistent with the larger pattern of progressive rotation. The Carmen Formation sediments dip at an average of ~10-25°, overlying the Comondú and tuff units across an angular unconformity.

4.6. Discussion

4.6.1. Onset of Extension

The age of the pyroclastic units of 15.8 Ma provides the minimum age for the onset of extensional tectonism in what is now Isla Monserrate. This age is synchronous with subduction and regional arc volcanism that deposited the Comondú Group in mainland Baja California.

In southern Baja California, previous studies (Drake et al. 2017; McLean, Hausback, and Knapp 1986; Umhoefer et al. 2002) have not found evidence of significant faulting in volcanic rocks older than 12 Ma, except for ~17-12 Ma detachment systems south of La Paz. This study's finding implies that local extension in the Monserrate area, and perhaps in the greater region of southern Gulf of California, began earlier than the accepted ~10-12 Ma timeframe for the onset of GoC rifting. There are two possible explanations: 1) this early deformation was arc/subduction-related extension rather than rifting; 2) the tectonic reorganization in Monserrate area might have begun earlier than previously suspected.

Explanation #1 above is largely based on similar examples of documented intra-arc extensional faults in other regions of the GEP (Busby et al., 2020; Graettinger et al., in press). Other locations of Baja California experienced extensional deformation during the Miocene arc volcanism. These locations include the Bahía Concepción fault zone (BCFZ), and the hypothesized extensional basin east of the BCFZ under the present-day Gulf of California that accommodated the deposition of Middle Comondú volcanics. The Monserrate detachment could have been first activated by topographic gradients and collapse of the westward-sweeping axis of the subduction arc that thermally uplifted the region. If so, the observations in this study show that these faults remained active throughout most of the period of rifting from ~12 Ma to the Pliocene.

Explanation #2 would suggest an earlier onset of rift-related deformation in the Isla Monserrate region. Fletcher et al. 2007 demonstrated a series of microplate capture events that led to the opening of the Gulf of California, which coincides with the 16 Ma onset of faulting in Monserrate. Magnetic anomalies demonstrate that shortly after 16 Ma, the East Pacific Rise fragmented and rotated clockwise into a series of eight shorter spreading segments connected by transform faults oriented parallel to Pacific-North America plate motion (Lonsdale 1991; Mammerickx and Klitgord 1982). Fletcher et al. 2007 proposed that this reorganization of the spreading system must have occurred after the opening of a deep slab window beneath the proto-Gulf of California, coinciding with the onset of rifting in the GEP.

Explanation 2 would involve a (likely partial) shift in tectonic motion from subduction to rifting well before the geochemical transition from arc magmatism to rift magmatism. According to this explanation, both waning subduction and Farallon-derived microplate capture events could have generated magmatism during a transition period in the Middle Miocene. In fact, arc

volcanism geochemical signatures are detected in many Quaternary volcanic centers in modern Gulf of California (Avellán et al. 2019; Batiza 1978; Batiza, Futa, and Hedge 1979; Ferrari, Stock, and Fucugauchi 2000; Guerrero et al. 2021; Ocampo-Díaz et al. 2021; Osorio-Ocampo et al. 2019; Sosa-Ceballos et al. 2019). Therefore, arc geochemistry alone does not preclude the mechanical transition from subduction to rifting.

Because the Farallon-derived Magdalena microplate was severed underneath North American Plate at ~16 Ma, the deeper portions of the slab must have continued to subduct while the shallow portions became accreted to the base of the Baja California microplate, an act that should have significantly diminished shallow subduction at the trench (Fletcher et al. 2007). Other studies (i.e., Brothers et al. 2012; Ferrari et al. 2013; Hausback 1984; Umhoefer et al. 2001) also note waning subduction and possible tectonic reorganization in southern Baja at ~16 Ma. The onset of Monserrate extension coincides well with ~16 Ma subducted microplate severing event, and it also likely ended within the timeframe when the GEP continental crust was thinned below sea level and ruptured to the east, completing the separation from the mainland North America. If we use the definition of rifting as the process that separated BCM from the mainland North America, then the detachment faults found in Monserrate that remained active throughout the extensional stages of lithospheric thinning and rupture should be considered rift-related extension.

4.6.2. Rolling Hinge and Extensional Basins

Comparing the syn-extensional sedimentary deposits associated with each detachment system on Isla Monserrate shows that the aerial extent and volume of the early and late syn-extensional deposits increase from east to west. This suggests that there is a systematic variation in the size

of extensional basins, controlled by the associated detachment system. This observation fits with the rolling hinge model (Bartley, Fletcher, and Glazner 1990; Wernicke and Axen 1988). In this model, an initially higher-angle normal fault strand becomes deactivated, uplifted, and rotated to a lower angle (Figure 65). If extension migrated from east to west across Isla Monserrate, the eastern fault strands would have been deactivated and uplifted earlier than their western counterparts. Thus, the eastern extensional basins would have been either eroded or could not accommodate as much marine deposition as the more deeply submerged western fault basins. The eventual deactivation of all three detachment systems and subsequent isostatic rebound of Monserrate might be the mechanism behind Quaternary uplift, as discussed in Chapter 5. This could also imply the existence of another, younger detachment system west of Isla Monserrate, creating a submarine basin to the west and uplifting Monserrate to the east.

4.6.3. Timing of Dike Emplacement

The pre-tuff Comondú rocks, including the intrusive units, on Isla Monserrate have not yet been dated. This study favors a syn-extensional age for the dikes, based on the following reasons:

Dikes on Isla Monserrate were observed to cut the pre-extensional Comondú rocks, and therefore the dikes must postdate the Comondú deposition. Many of the dikes found near the Central and Eastern Monserrate Detachment fault zones were emplaced parallel to the fault plane (Figure 57). This evidence suggests that the emplacement of dikes was likely associated with the extension, as has been suggested by other previous studies on the association between extensional zones and dikes (Anderson 1951; LaForge, John, and Grimes 2017). At least one locality (Figure 57) shows a dike cut by detachment fault, with an approximate offset of ~20 m.

This is significantly less than the estimated displacement of the Comondú by the detachment systems (Section 4.1.1.), which suggests the dikes were emplaced sometime after the extensions had begun deforming the Comondú. However, the possibility that some of these dikes might be feeder dikes for younger pre-extensional Comondú rocks and may predate the onset of extensional faulting cannot be ruled out.

4.6.4. Tuff Fanning-Dip Sequence

The existence of fanning dips ranging from ~10-35° within the trachydacite tuff deposits could be interpreted in different ways. Analyses of samples taken from the upper section and lower section show similar geochemistry, which could be interpreted as eruption from the event. Based on this, some could argue that the apparent intra-tuff angular unconformities could be a product of soft sediment slumping. Alternatively, tuff composition could have remained similar over multiple eruption events and potentially over long periods of time. In fact, the tuffs in the upper and lower portions of the sequence do differ slightly, for example in color and mineralogy, from light-brown amphiboles and apparent lack of biotites in the upper most section to the black amphiboles and presence of biotites in the lower portion. The existence of multiple normally graded beds within the tuff also could imply multiple depositional sequences. It is also possible, however, for multiple graded beds to occur in tuff deposits created from single eruption event, as can be seen in Bishop Tuff (Wilson and Hildreth 1997).

Several beds within the trachydacite tuff sequence are coherently stratified, with no evidence of soft sediment deformation. Slumping or other soft sediment deformation is typically associated with complex internal deformation, including ball-and-pillow structures, flame structures, or folds (Boggs 2006). The Monserrate trachydacite tuff beds lack evidence of such

deformation. For example, at the southern hillside of Plateau 2, the basal tuff bed extends continuously, undisturbed and undeformed, and with no significant thickness change. If these tuff beds were deposited on top of an already existing half graben with enough topography to cause soft sediment slumping downslope, one would expect the beds to thicken towards the basin, rather than having a homogenous thickness. This study interprets the internal angular unconformities in the trachydacite beds as fanning dips that formed due to deposition in a half-graben basin during active extension (Figures 20, 61 B). The structural complexity associated with this location will be discussed in the next part of this section.

4.6.5. Reverse Fault – Possible Post-Detachment Exhumation

The reverse fault cutting through Plateau 2 (Figures 2, 18, 19) shows only a small amount of displacement, but its significance comes from the change in orientation of the beds across the fault plane. While the foot wall block to the west dips down to the east, deposits in the hanging-wall block dip to the west, contrary to pre- or early-extensional stage units elsewhere on Monserrate. As this is a reverse fault, the likely explanation is that the beds were originally east-dipping but were uplifted and tilted due to fault-bend folding. The result is an inverse fanning dip, with the uppermost strata dipping most steeply to the west and the basal strata dipping the least (Figure 20). As the reverse fault does not seem to crosscut Pliocene carbonates, the slip may have occurred during the Middle to Late Miocene, after the deposition of earlier tuff and before the marine sediments.

4.6.6. Diagenesis and Induration of the High-Elevation Carbonates

The indurated carbonates on the high-elevation plateaus on Isla Monserrate resemble Quaternary calcareous sediments on coastal terrace surfaces at lower elevations. Those terrace and terrace-capping sediments will be discussed in Chapter 5. However, rather than being a separate, younger unit deposited during coastal terrace formation, these well cemented carbonates are more likely a product of weathering of Pliocene sedimentary deposits.

Unlike the Quaternary terrace cover sediments, the indurated high-elevation carbonates contain little to no lithic siliciclastic clasts aside from the basal conglomerate layer. They also contain little to no cross laminations such as ripples, which are commonly found in the younger terrace deposits (Figure 63). The macrofossil assemblages within the indurated carbonates – rich in pectenids and rhodoliths but lack gastropods and large coral heads – are similar to fossils in the Pliocene sequence and are dissimilar to the fossils found in Quaternary terrace deposits.

The interpretation of indurated carbonates being a separate unit from terrace deposits is also backed by the presence of carbonates being controlled by the underlying geology. The indurated carbonates are only found where the bedrock is composed of fossiliferous Pliocene sequence, but not on top of the Comondú bedrock (Figure 52). Furthermore, at the northwestern coastal terrace level 4 (see Chap. 5), which is underlain by tuff, the surface is not covered by indurated carbonates and directly exposes the tuff bedrock. These observations suggest that the high-elevation plateaus may not have had an original, depositional carbonate-rich cap in all areas of Monserrate.

Another piece of evidence is the nature of the contact between marlstones and indurated carbonates. The contact between lower-level terrace-covering sediments and Pliocene sequence is sharp (Figure 53). This is contrasted by the gradual and lateral nature of the contact between indurated carbonates and Pliocene marlstones, best illustrated by Figure 54. This suggests that

the indurated carbonates are the result of post-depositional recrystallization of the softer Pliocene sequence due to weathering, rather than a younger, overlying depositional unit.

Based on these properties and their weathered, karstified textures, such as dissolution pits and pit caves, the likely conclusion is that these indurated carbonates are epikarsts of Carmen Formation sediments. Given the emergent history of the island which will be discussed in Chapter 5, the higher elevated surfaces were exposed to atmospheric weathering for longer than the recently exposed lower elevation sedimentary units, thus developing much stronger carbonate weathering lithology and surficial characteristics. Such karstification also seems to have been intensified at the level of basal contact between the basement rock and the overlying carbonates, where freshwater lens/vadose zone likely developed (Mylroie and Mylroie 2007). Such accelerated diagenesis process around the contact of the Comondú basement and overlying carbonates could explain the higher degree of calcareous fossil material dissolution at the lower strata of elevated plateau carbonates. Subsequently, these dissolved, leached out fossils probably provided the cement materials required for the induration of the surrounding matrix. This is further supported by the fact that the epikarst development seems to be more intense in facies with higher skeletal fossil composition, such as elevated platforms' biostrome carbonate layers.

4.6.7. Depositional Environment

Several studies discuss the depositional environment of the first marine sedimentary deposits on Isla Monserrate (Carreño et al. 2015; Johnson 2014; Martínez and Yanet 2019; Vázquez et al. 2007). Carreño et al. (2015) found deeper bathyal microfossils within the orange-colored marlstone that crops out on northern Monserrate but argued for shallow bathyal depth. According to the study, the deep-water microfossils are the result of upwelling driven by tidal

mixing, as observed in the modern-day northern Gulf of California. In contrast, Johnson (2014) and Vázquez et al. (2007) noted the presence of armored mudballs as evidence that the marlstones were deposited on a deeper marine ramp, driven by gravity flows and bathymetric relief.

This study favors the latter conclusion, where a small island core (or a series of small island cores) made of the Comondú volcanics was exposed barely above sea level during the Pliocene (Figure 61 D). Around this island core, a shallow marine carbonate shelf developed, which was surrounded by steeper and deeper marine ramps. In support of this interpretation, armored mudballs were found in the lower-elevation Pliocene deposits, and were absent in high-elevation plateau coquina beds.

Other evidence that supports a deep depositional environment for low-elevation Monserrate marine sediments is the orientation of the plateau-forming carbonates and coastal marlstones. Most of the plateau carbonates are nearly horizontal; in contrast, the northern beach marlstones dip to the north and southern beach marlstones dip to the south. Comondú rocks on Isla Monserrate have been tilted down to the east, so that the dips of the Pliocene sediments are interpreted here as syn-depositional bathymetry. The interpretation here is that the current carbonate highlands of Monserrate formed a shallow marine carbonate platform during the Late Miocene-Early Pliocene (Figure 61 D). From this source, the sediments were transported downslope, depositing deeper marine marlstone ramps that dipped away from the shelf. The plateau carbonates have denser biostrome layers compared to the low-elevation marlstone; marine platforms at wave base would include larger skeletal grains than a deep marlstone.

The model above also explains why the plateau carbonates are thinner than the low-elevation marlstones, since deposition on a shallow platform could exceed the accommodation

space controlled by sea level (shown as shallow marine biostrome deposition in Figure 61 D). The coastal outcrops also have thicker and coarser-grained basal conglomerates, whereas the high-elevation carbonates exhibit thinner and finer grained base. The marlstones' basal conglomerate layers represent transgression associated with syn-rift submergence (Figure 61 C). At this stage, most of the surrounding area was subaerial, allowing a large quantity of coarse-grained sediments to be deposited. In contrast, at the peak of the submergent phase, most of the source area would have been submerged, resulting in less transport and deposition of siliciclastic sediments.

4.6.8. Syn-depositional deformation

Earlier studies (Johnson 2014; Vázquez et al. 2007) suggested that active seismicity from extensional faults triggered gravity flows that caused the formation of armored mudballs. This study further supports the interpretation of syn-depositional extension; Comondú fissures with horizontal fabric suggests that these fissures were opened at a shallow depth and were filled from above, coeval with the deposition of Carmen Formation sediments; fault-related drag-folding of Carmen strata imply that these sediments were still plastic at the time of deformation.

Chapter 5. Late-Stage Extension and Uplift

The late phase on Isla Monserrate is recorded by geological units and landforms developed during the island's late-stage uplift. Such features include the island's emergent geomorphology such as elevated plateau surfaces and coastal terraces, and other modern landforms such as eolian dunes, beaches, wave-cut notches, and fluvial channels.

5.1. High-Elevation Plateau Surfaces

The interior highlands of the Monserrate are marked by disconnected plateaus (Figure 3). Most of the plateau surfaces show heavily weathered and surfaces cut on Pliocene Carmen carbonate bedrock, with little or no additional sedimentary cover (Figure 55). At a few locations, however, such as Plateaus 6 and 8, the plateau surfaces are cut onto Comondú bedrock. At these locations, the plateau surfaces have a float of well-rounded gravels and isolated fossil fragments on the surface.

Because the plateaus are disconnected from each other, sometimes with hundreds of meters separating them, determining if these plateaus belong to the same terrace geomorphic level or if they represent different steps, remains challenging. To address this, this study analyzed surface slope alignment (Figures 9-16) and surface elevation frequency distributions (Figure 17), with those methods detailed in Chapter 2. The results are presented below.

On Plateau 6, the elevation profile (Figure 11) shows a change in slope between the northern and southern areas of the plateau. The southern half of Plateau 6 is nearly horizontal, with a slope of just 0.0017. In contrast, the northern half surface of Plateau 6 slopes 0.072. The southern half of Plateau 6 is the highest plateau of Isla Monserrate, and no other plateaus align

well with its surface. This highest plateau group is dubbed Group 1 in this study (Figure 4). Group 1 is located in the southeastern section of the island, coincident with the highest topography of the island (Figure 1).

The profile slopes of Plateau 7 and 8 (Figure 10), Plateau 5 and northern half of 6 (Figure 11), Plateau 3 and 5 (Figure 12) all have similar slopes. Plateau 2A aligns with the more steeply inclined northern surface of Plateau 3 (Figure 13). Plateau 3 and 8 (Figure 9) are moderately aligned, with a possible break in slope between them. Plateau 4 is moderately aligned with Plateau 3 but shows poorer alignment with 5 (Figures 14, 15). Assessing Plateau 4 is challenging, because it is small and uneven. Considered as a whole, Plateau 2A, 3, 5, 6, 7, and 8 are assigned to the second highest terrace level, Group 2. Group 2 plateaus are mostly located in western and central Monserrate.

Plateau 1 and 2B (Figure 16) are aligned similarly, and therefore are classified into the same terrace level, Group 3. Plateau 4, which showed poor alignment with Group 2 surfaces is tentatively associated with Group 3. Group 3 plateaus are located around the northern area of Isla Monserrate (Figure 4). The surfaces in this group are small compared to other plateaus such as Plateaus 3 and 6. The smaller area of the surfaces in Group 3 also increases the uncertainty in grouping it with other surfaces, and it is unclear if Plateau 1 should be considered a terrace level even lower than Group 3.

As described in Chapter 2 (Methods), the distribution of elevations on each terrace unit were analyzed in GIS to help understand terrace topography and correlations. Histograms of surface elevation points (Figure 17) shows at least three modes, which supports the classification of at least three plateau groups. The elevation cluster with the highest elevation mode, at 207.7 m (Figure 17 B), corresponds to plateau Group 1. This group is relatively tightly clustered about the

207.7 m mode. This area includes the horizontal southern half of Plateau 6. The second terrace-elevation mode consists of two closely spaced peaks, at 175 m and 170 m, the latter being the dominant mode. This group of elevations varies more than Group 1.

The elevations of the younger plateaus, Group 3, must be examined separately from other plateau groups due to a much smaller preserved surface area. The frequency distribution histogram in Figure 17 C shows a possible bimodal distribution, with two peaks at 132-139 m range and 104 m. This bimodal distribution could represent either noise in the topographic data or possibly two subgroups/levels.

5.2. Coastal Terraces

Below the high-elevation plateaus, Isla Monserrate also has a sequence of well-developed coastal terraces. At least four distinct levels of terrace have been identified: Terrace 1, the youngest level, assumed to be MIS 5e (~125 kyr; Shackleton 1987) in previous research (Oretsky 2020), Terrace 2, Terrace 3, and Terrace 4, listed from the lowest to the highest level above Terrace 1 (Figure 5). Potentially, there is another, even younger level of terrace than what Oretsky (2020) mapped as level 1. This level sub-1 terrace is found only along the west coast of Isla Monserrate and is lower than the Terrace 1 level found adjacent to it, as will be described in the later part of this chapter. The different terraces differ in their elevations and have variations in features such as surface slope, sediments, and substrate. Additionally, even within the terraces of the same level, significant local variations exist, in terms of elevations, surface geometry, and sediments, as detailed below.

All four consecutive levels are present together only on the northwestern and southwestern coasts of the island (Figure 5). Although terraces are present along most of the Monserrate coastline, they typically feature level 1, with level 2 rare and level 3 even rarer.

5.2.1. Terrace Substrate

Segments of Terrace 1 on much of Isla Monserrate are cut onto the Comondú (Figures 2, 5, 52). In contrast, Terrace 4, located in the northwestern terrace sequence (Figure 5), is underlain by pyroclastic deposits (Figures 2, 5). Otherwise, the best-preserved terraces on Isla Monserrate seem to occur predominantly on top of Pliocene carbonate bedrock, as the widest and largest terraces seem to have been preferentially developed or preserved on this sedimentary substrate.

5.2.2. Terrace-Covering Sediments

A veneer of shallow marine sediment often is a good indicator for distinguishing coastal terrace surfaces from other morphological benches. On Isla Monserrate, terrace-capping sediments can be difficult to distinguish from the underlying Pliocene deposits as both are fossiliferous and calcareous. However, terrace-capping sediments on Monserrate typically lack the distinctive orange color of some of the Pliocene deposits, are richer in siliciclastic grains, and feature younger and shallower fossil assemblages.

Terrace-capping deposits become rarer on the higher, therefore older terrace levels. The thick sedimentary beds on level sub-1 and level 1 terraces (Figure 63) contrast with a typically thinner veneer on Terrace 2, to sparse cover or bare bedrock platforms on Terrace 3 and higher. On these high levels, terrace sediments are sometimes present only as isolated clasts or pockets

of rounded cobbles and pebbles. The clasts are typically covered in desert varnish and are composed of Comondú or tuff.

The sediments atop Terrace 1 and the sub-1 terrace can reach up to 4-5 m in thickness and are locally stratified, with interbedding conglomerates and sandstones (Figure 63). These lower terrace deposits are identifiable by their tan-white colored sands with dark clasts. The moderately well sorted white sands are calcareous, made of marine skeletal fragments. The dark gray and brown silicic grains are made of Comondú or tuff and are poorly sorted, ranging from sand to gravel and cobbles. These deposits have a carbonate-rich muddy matrix and are moderately cemented by secondary carbonates.

Terrace-capping sediments include marine fossils, ranging from gastropods to molluscs and corals (Figures 62, 63). Interestingly, gastropods are commonly found in terrace-capping sediments, in contrast to the Pliocene sediments, which are dominated by bivalves. The chronology analysis completed by Charles Powell (Chapter 4) shows that the terrace-capping fossils are likely recent (Table 2). Preservation of fossils in the terrace caps is consistent with their recent age, and the inner nacreous layers of a few bivalve specimens are still intact (Figure 62). Whole coral heads up to ~20-30 cm in diameter are common. Since these deposits typically contain >10% of >2mm organic grains which were disrupted and displaced from their original emplacement by wave energy, as evident by pieces of detached coral heads, they can be categorized as float stones (Dunham 1962).

A few outcrops of the sub-1 terrace along the western shore of Isla Monserrate show well developed ripple cross laminations and imbrication of gravels (Figure 63), indicating nearshore environment above wave base, consistent with most terrace caps. The direction of imbrication is approximately to the east, towards the modern-day island interior.

5.2.3. Paleo Shoreline Angle Elevations and Uplift Rate

The paleo shoreline angles (PSAs) of different terrace levels were identified in the field, and surface elevations were estimated from the drone-based DEM. The accuracy and precision of these elevations was not tested, with uncertainty within the realm of ~1-2 m. In an area of uniform uplift, PSA elevations from the same terrace level should be equal. Systematic differences in PSA elevations can suggest locally varying uplift rate.

Figures 6 and 7 suggest that PSA elevations for the same terrace levels seem to vary in different areas of Isla Monserrate. For example, in northwestern Monserrate, the PSA of Terrace 3 has elevations of ~69-73 m a.s.l., gradually increasing from west to east. This increase in elevation is repeated for Terrace 2, which increases from ~45 m on western part of the terrace to ~50 m to the east. In contrast, terraces on southwestern Isla Monserrate are significantly lower, ~48-55 m for Terrace 3, ~33-35 m for Terrace 2. On Terrace 1, PSA elevations are ~22-23 m a.s.l. on the northwestern coast, compared to ~11-14 m along the southwestern coast. Regional differences in terrace uplift are also suggested by PSA elevations of Terrace 1 at different locations around Isla Monserrate (Figure 6). PSA elevations on Terrace 1 are highest at the southern tip of the island, averaging ~19 m a.s.l., and on the northwestern coast, where the elevations average ~23 m. The east and west coast terraces seem to be lower, with typical PSA elevations ranging ~9-12 m.

5.3. Recent Sediments

There is active erosion and deposition on Isla Monserrate, resulting in fluvial channels, sandy coasts, and eolian deposits. Beaches on the northern and southwestern coasts feature orange fine-

grained sand due to the erosion of adjacent orange marlstones. In contrast, most of Monserrate shorelines are dominated by dark gray and brown siliciclastic gravels, with clasts derived primarily from Comondú rocks. The island has also developed fluvial channels filled with alluvial deposits, transporting sediments to the shore during ephemeral flow and flooding events from the island interior. The northwest shore of the island also has dune deposits (Figure 64).

5.4. Discussion

5.4.1. Early-Stage Uplift

Due to the poor preservation of fossil material on the plateau surfaces, it was not possible to estimate when these surfaces were last submerged. The interpretation here is that these surfaces were submerged by the early Pliocene, during which a wide and low-relief shallow-marine carbonate platform was built in what is now the interior of Isla Monserrate. Afterwards, the island began to emerge. Notably, none of the higher and lower terrace surface or terrace-capping sediments have been offset by extensional faults. This suggests that the uplift began only after most deformation of the island had ceased.

This study proposes that Plateau Groups 1, 2, and 3 (Figure 4), represent the order of emergence above sea level. According to this interpretation, the southeast portion of Isla Monserrate was the first to be exposed above sea level. One could argue that some parts of it never completely submerged underwater, since a few locations of the plateaus never developed carbonate bedrocks. Alternatively, some of these marine deposits might have eroded away, and exposing the Comondú bedrock underneath. After the emergence of southern Monserrate, the western/central portion of the island emerged, then the north. This interpretation is supported by

the observation that the highest areas of Isla Monserrate are located in the southeast, while the topography in the northern section tends to be lower (Figure 1).

5.4.2. Late-Stage Uplift

The reason why the west coast of Isla Monserrate is the only place where all four terrace levels are preserved is unclear. One possible explanation is based on the nature of bedrock and its association with the detachment systems on Isla Monserrate. Since the Monserrate detachment faults dip west, the hanging wall fault basins preferentially developed on the western side of the island. This is supported by the fact that western Monserrate is where the largest volume of soft, poorly lithified deep-water sediments was deposited, as discussed in the previous chapter. In contrast, the Comondú volcaniclastics that make up most of the bedrock on other coastlines are typically well lithified and therefore more resistant to erosion. Wave energy would carve wider terrace platforms on the marlstone bedrock, as opposed to the narrower terraces that developed on the Comondú bedrock coastlines. This might explain why the west coast of Isla Monserrate, rich in marlstone, has more and better-preserved coastal terraces than other areas of the island.

This chapter notes that the lower terraces on Isla Monserrate have thicker sedimentary veneers, whereas Terrace 3 and higher terraces are typically stripped of sediments. Such contrast could have been because at the early stage of uplift, much of the island bedrock was still submerged and thus would have produced less sediments. Later uplift would have raised enough island mass above sea level to develop a fluvial network and transport sediments to the shore. Another possible interpretation is that subsequent erosion might have removed much of the sediments in the older terraces.

The elevation differences between the northwestern and southwestern terraces, and systematic variations in PSA elevations of Terrace 1 suggest differential uplift across Isla Monserrate. Uplift seems to have been most rapid in the northwest and southeast coast, while the east and west margins of the island show uplift approximately half as fast (Figure 6, 7).

5.4.3. The Cause of Uplift

The cause of Isla Monserrate's shift from submergence to emergence remains unclear. One possible explanation related to the rolling-hinge model, where the center of active extension "migrates" through the system (Axen and Hartley 1997; Buck 1988; Mizera et al. 2019; Spencer 1984; Wernicke and Axen 1988). According to this model, during detachment system evolution, an active extensional fault that initially controls the extensional basin becomes deactivated. When this happens, the former basin margin is exhumed and rotated to a shallower angle due to differential isostatic rebound. Simultaneously, a new, steeper fault strand forms in the middle of the extensional basin, becoming the new margin of the extensional basin. The low-angle detachment faults on Isla Monserrate might record an east-to-west succession of exhumed, inactivated extensional systems. Since they do not cut young terrace sediments or erosional terrace surfaces, these faults have been inactive at least since Isla Monserrate's uplift began. Another piece of supporting evidence is the systematic increase of extensional basin size from east to west. As discussed in the previous chapter, the volume of syn-extensional basin sediments associated with EMD, CMD, and WMD strands increases, in the listed order. The schematic cross section (Figure 8) of Isla Monserrate's geology also reveals lower basins in the west compared to the eastern extensional systems. These suggest that Isla Monserrate's recent uplift

might be related to the deactivation and exhumation of the Monserrate detachment strands, as the zone of active faulting migrated from east to west.

Another explanation is that Isla Monserrate's uplift might not be related to detachment systems, but rather lithospheric density changes due to thermal perturbations. East of Monserrate, in the GEP center where the rifting occurred, continental lithospheric mantle was replaced by upwelling asthenosphere (Busby et al. 2020; Calmus et al. 2011; Ferrari et al. 2012; Fletcher et al. 2007) (Busby et al. 2020b; Calmus et al. 2011b; Ferrari et al. 2012; Fletcher et al. 2007). This could have increased the buoyancy of the crust in the surrounding areas, including Isla Monserrate, thus uplifting the island. However, such change in mantle buoyancy typically affects a much larger region than the size of Isla Monserrate and would need to be corroborated by uplift rate data from adjacent sites along the GEP.

Chapter 6. Conclusion:

Mapping of Isla Monserrate, in the Gulf of California, shows a geologic record from pre-extensional subduction arc deposition to syn-extensional submergence, and to recent uplift.

Most of Isla Monserrate is made of Comondú Group rocks, primarily composed of trachyandesite lava flows and lahar sediments. Their bedding orientations are relatively uniform throughout the island, typically ~60-70°E. The lack of internal orientation variation suggests that these units were deposited before the onset of extension and subsequent rotation. Flow indicators found on the fluvial sedimentary bed suggest NE to SW paleo transport, consistent with the current understanding of Comondú volcaniclastic deposition from a subduction arc located to the east.

Extensional faults and angular unconformity mark the division between the pre-extensional Comondú Group rocks and the overlying syn-extensional units. The three Monserrate detachment fault systems strike NNW-SSE and dip ~30°W, with estimated offset of ~850 m, and show systematic increases in basin size from east to west. The timing of the extension is constrained by the oldest syn-extensional trachydacite tuff, with a $^{40}Ar/^{39}Ar$ date of ~16 Ma age. This age is significantly older than the currently hypothesized age of rifting for ~11 Ma in GEP. Possibly, some sort of tectonic reorganization occurred earlier, as suggested by some workers (Bryan et al. 2014; Ferrari et al. 2018). Alternatively, this extensional faults' early-stage deformation may have been caused by subduction-related extension.

Orange-colored marine marlstone deposits (in coastal outcrops) and indurated carbonates on elevated plateaus, were identified to be Late Miocene-Early Pliocene in age, correlative with the Carmen Formation, based on paleontological data. The Carmen Formation on Isla

Monserrate records submergence due to continued extension and lithospheric thinning, as shown by environmental analysis from fossil evidence: deposits from the coastal areas suggest a deeper marine environment, whereas the fossils from elevated plateau deposits suggest a shallow carbonate platform environment. Likely, these facies were deposited at the peak of extensional crustal thinning that submerged the island. Normal faults with ~3-4 m of offset found within the Carmen units also support deposition coeval with active extension.

After a period of subsidence, Isla Monserrate was then uplifted. Broad elevated plateau surfaces and coastal terraces are interpreted here to have been carved as the earlier marine transgression, followed by regression, punctuated by periodic eustatic fluctuations. The elevated plateaus developed in the Monserrate interior are the oldest surfaces, perhaps showing separate ~2-3 levels. Terraces found along the coastlines were grouped into four levels, with most remnants on the northwestern and southwestern coast, cut on Carmen bedrock. Unlike the elevated plateaus, which consist of heavily weathered carbonate bedrock, the lower terraces are capped by clastic beds, locally quite thick. The increasing thickness of terrace deposits is interpreted here as the development of sediment transport system as the island was uplifted and exposed to subaerial erosion. The sediment produced by erosion formed various landforms such as beaches and eolian dunes that can be observed today. The cause of the uplift remains unclear, with possible mechanisms including post-extensional isostatic flexure, rolling hinge seismic center migration, etc.

Figures & Tables

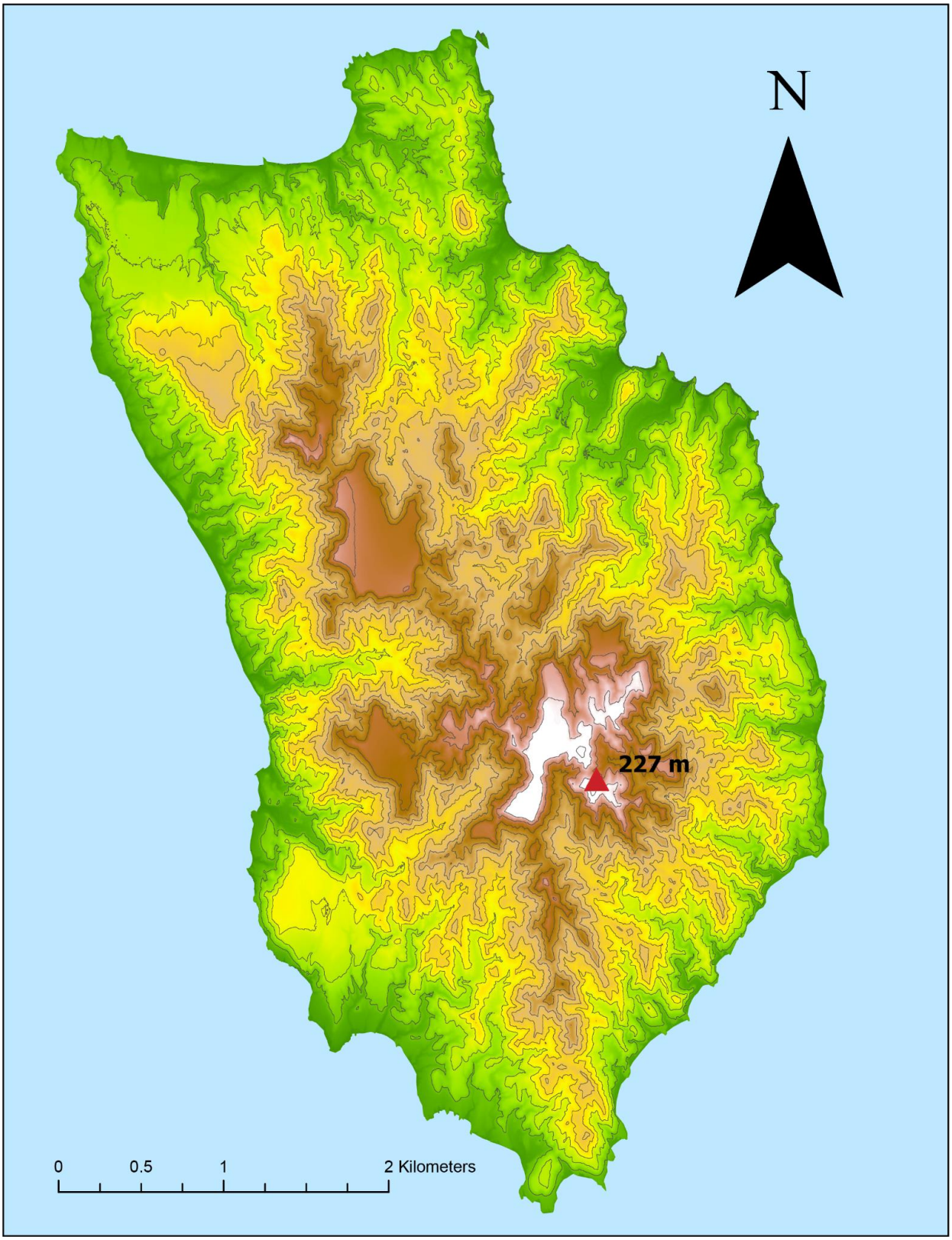

Figure 1. Topographical map of Isla Monserrate. The red triangle shows the highest peak of the island.

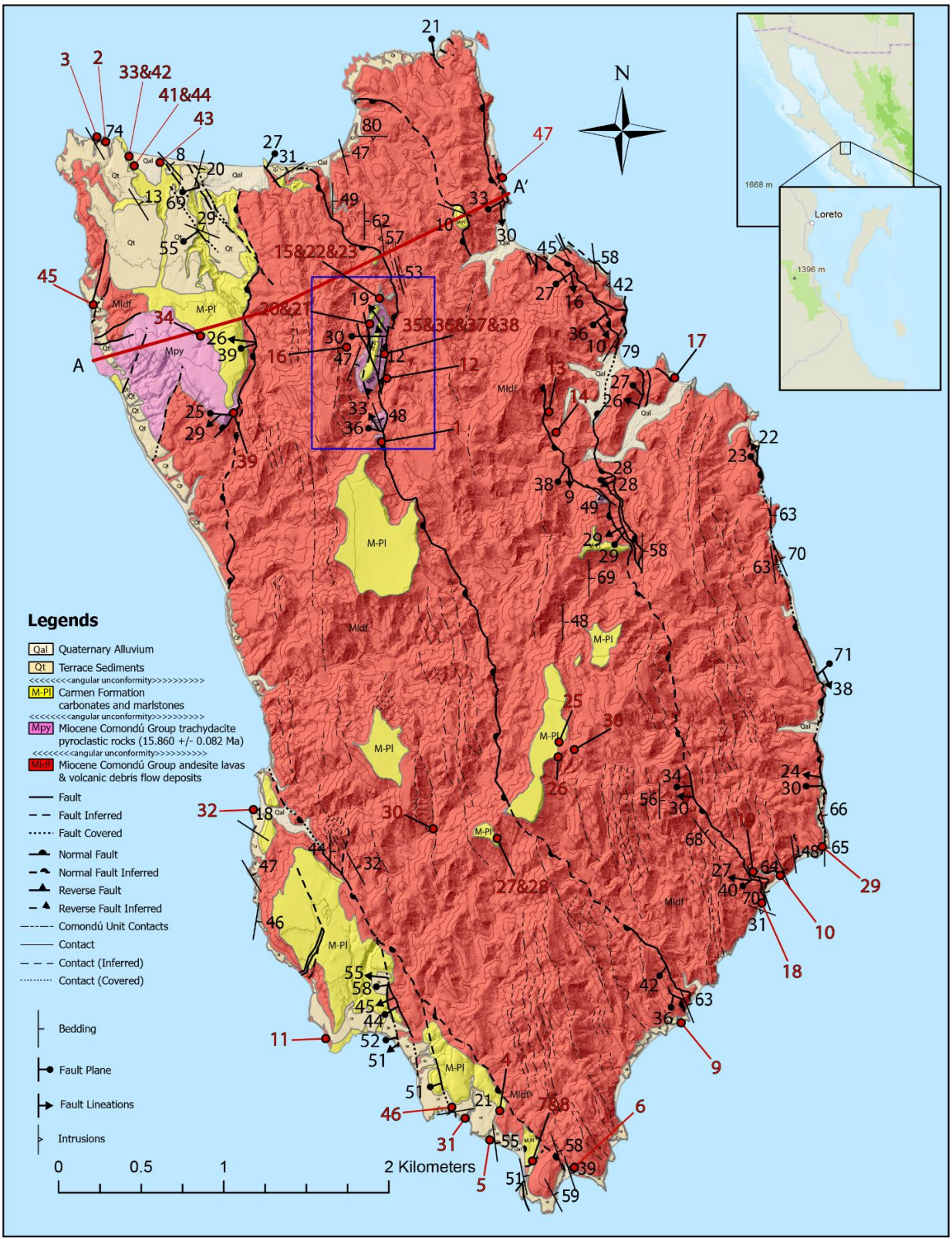

Figure 2. Geological map of Isla Monserrate, in Gulf of California. The blue square outlines the zoomed-up map in Figure 19. Information on sample stations (red dot) is presented in Table 1.

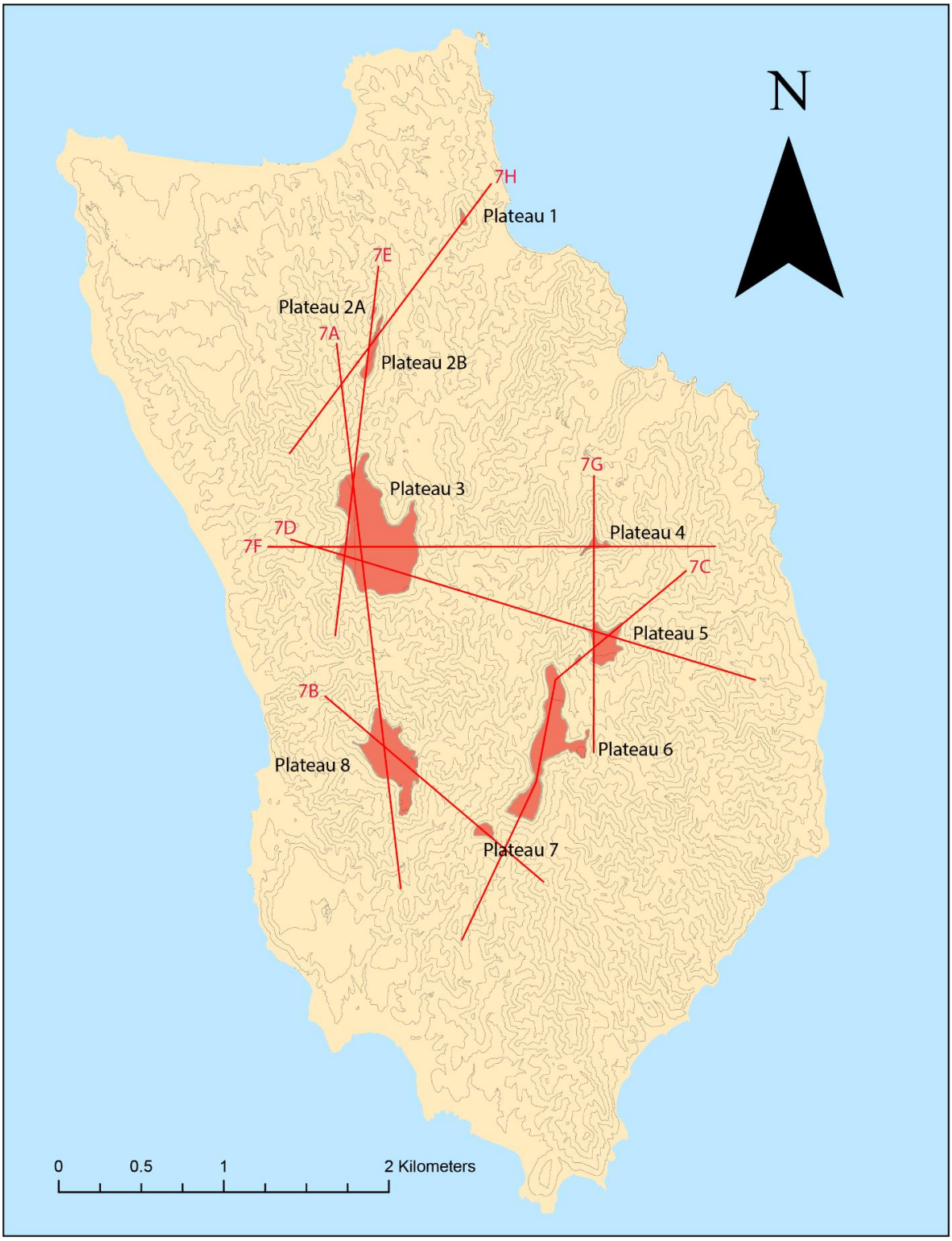

Figure 3. Names and locations of Isla Monserrate interior plateaus. Red lines are elevation profile lines drawn for plateau surface alignment analysis as shown in Figure 7.

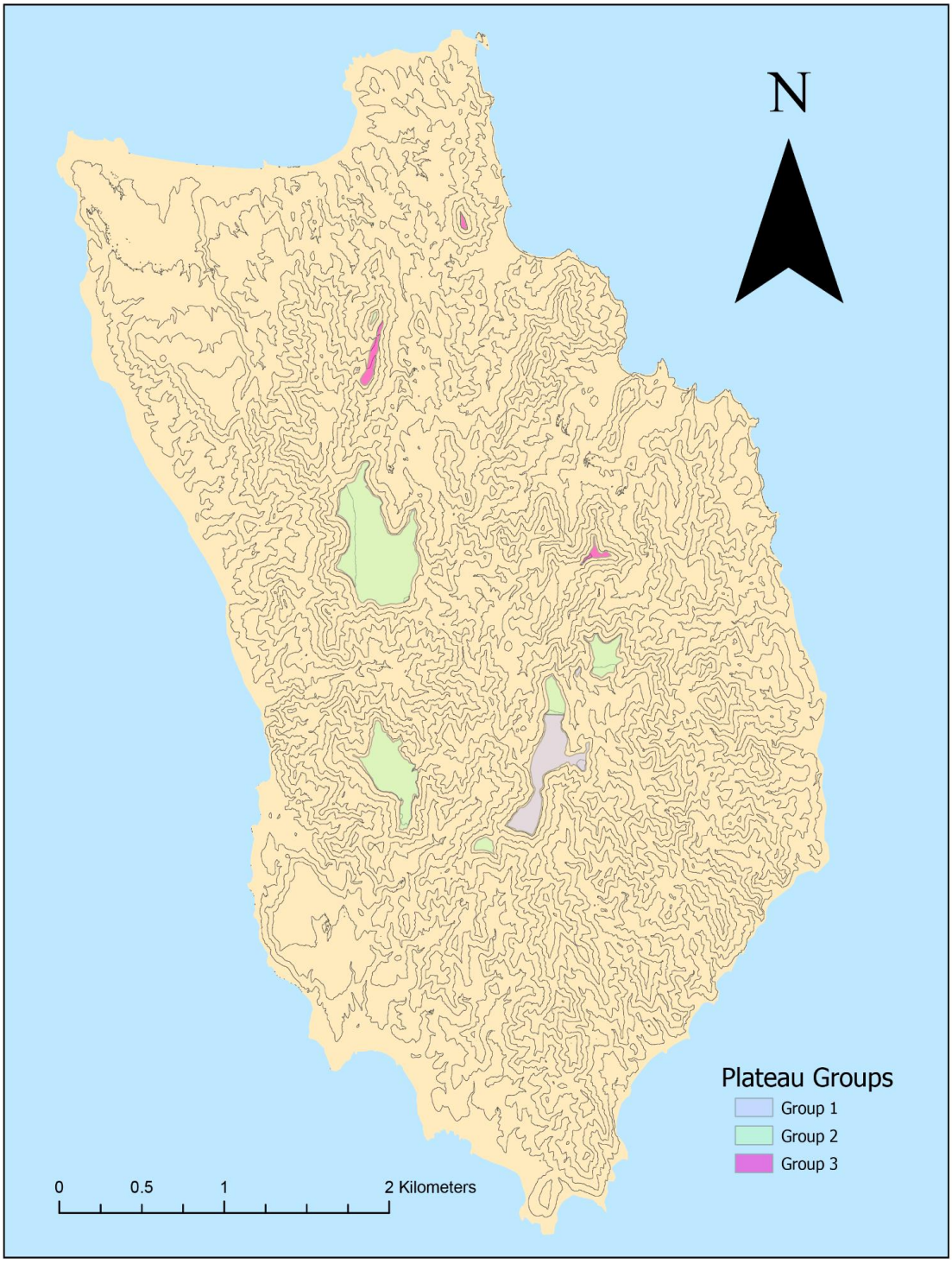

Figure 4. Isla Monserrate Plateau Groups – Classified based on Plateau Surface Alignment and Elevation Distribution Analyses. Group 1 is the highest and likely the most ancient terrace level, Group 2 a lower level, and Group 3 the lowest.

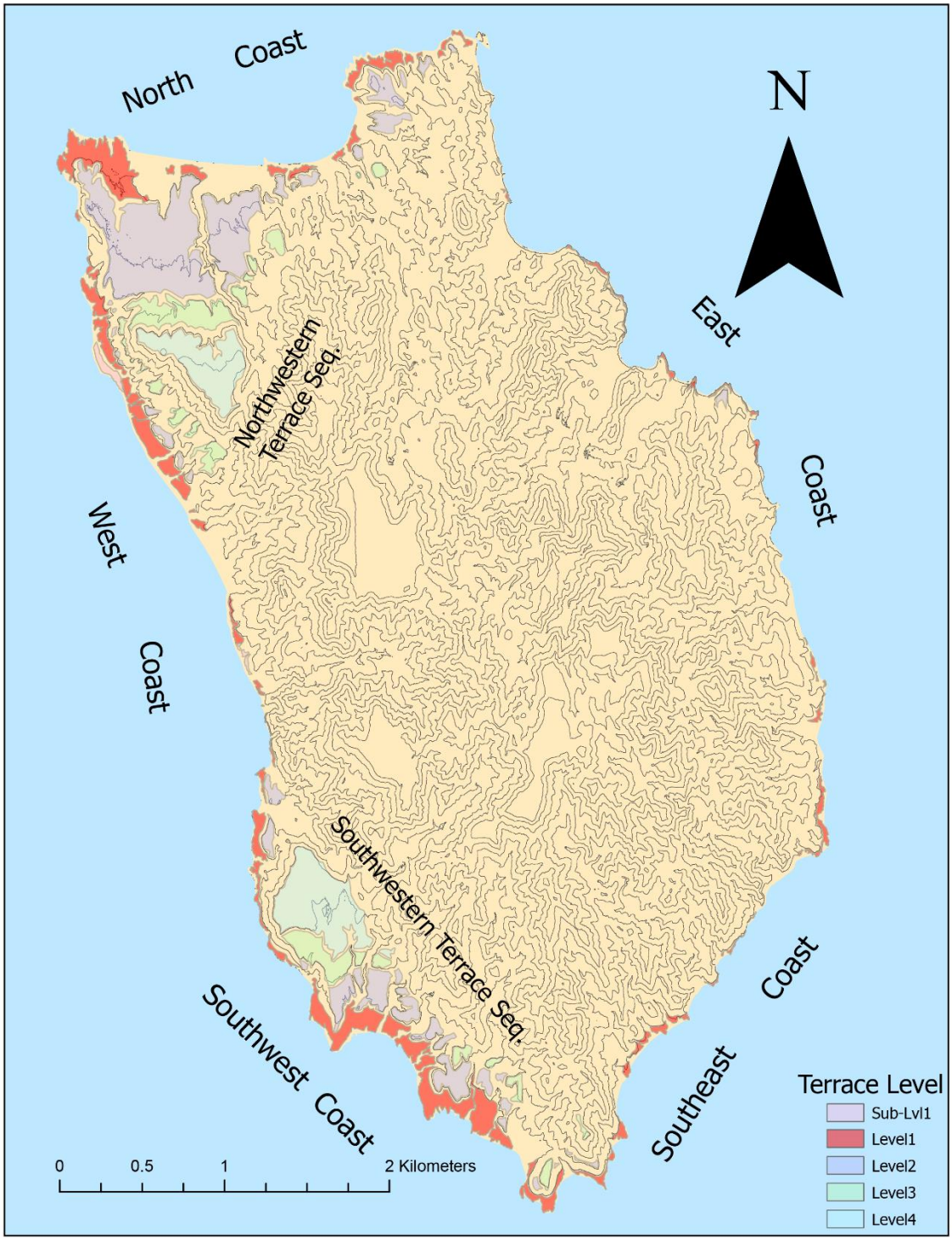

Figure 5. Map of all coastal terraces on Isla Monserrate. Successive terrace sequences containing all four levels are only preserved in the northwest and southwest.

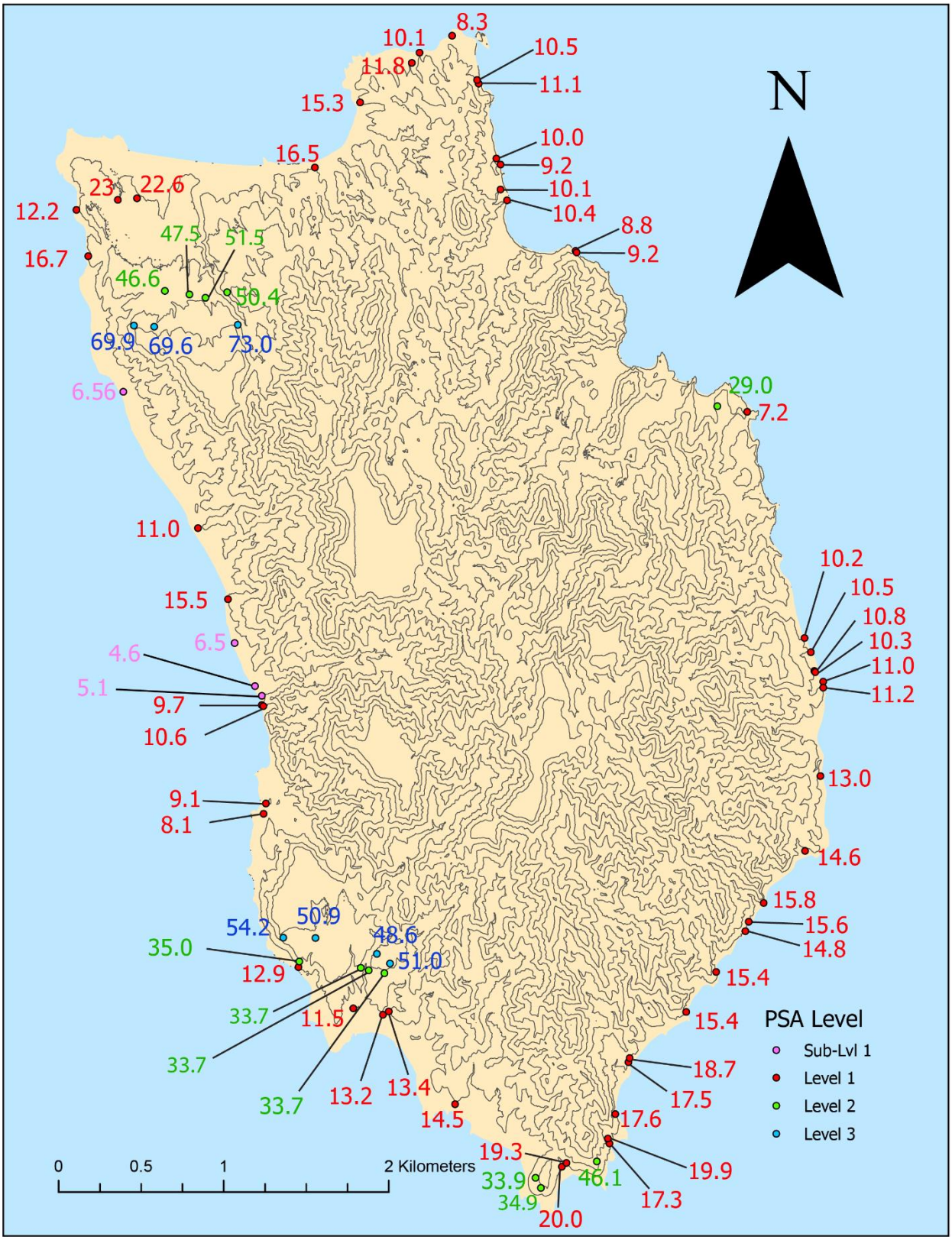

Figure 6. Locations and elevation estimates (m) of all terrace level PSA points.

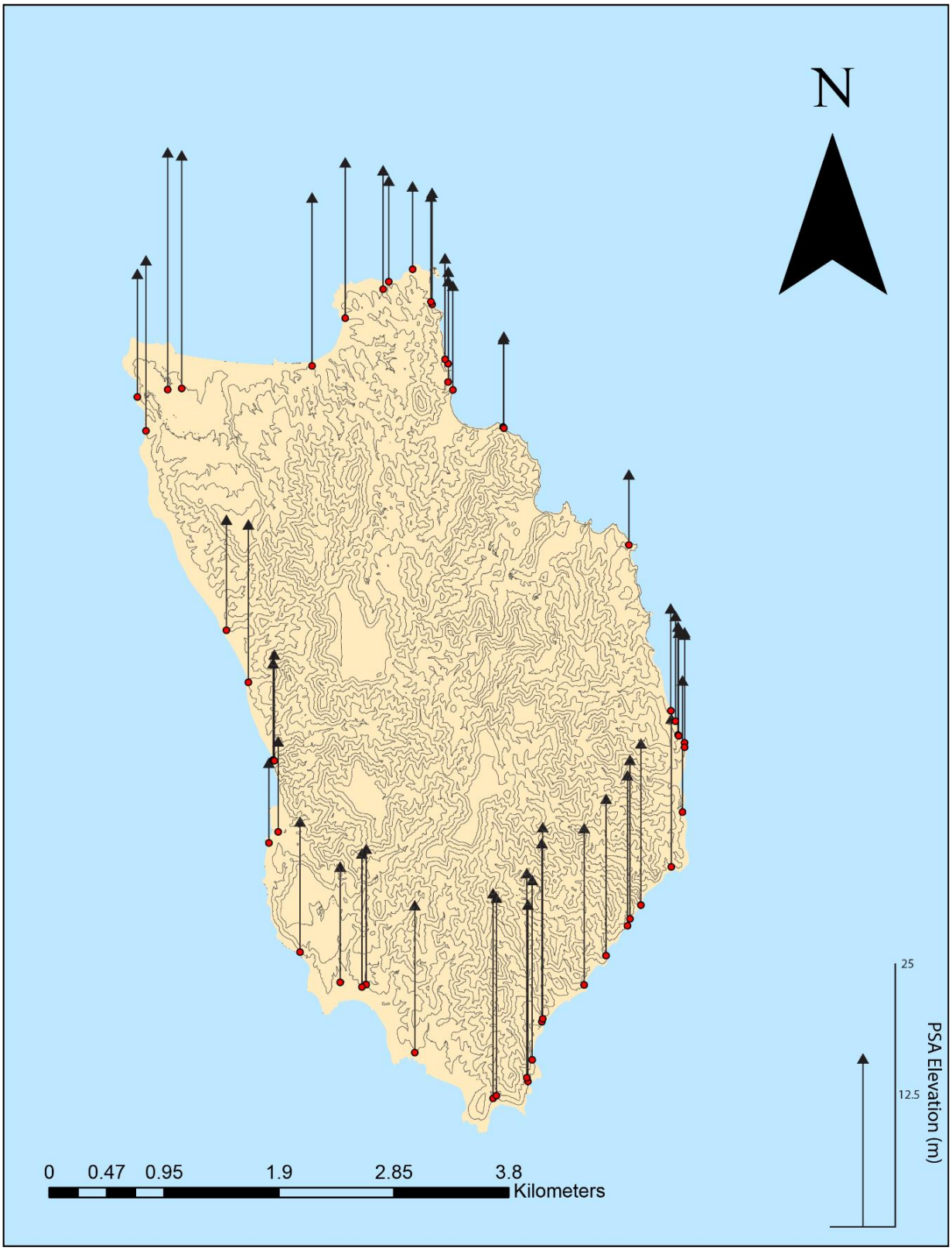

Figure 7. Elevations of Terrace 1 paleo shoreline angle (PSA) elevations, measured from the drone-based DEM.

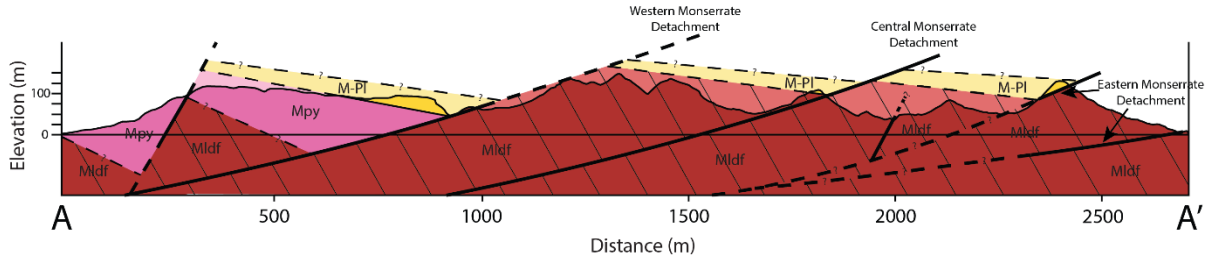

Figure 8. Cross section of A-A' on Figure 2, no vertical exaggeration. Legends and color schemes are identical to Figure 2. Note the lower, larger fault basins towards the west.

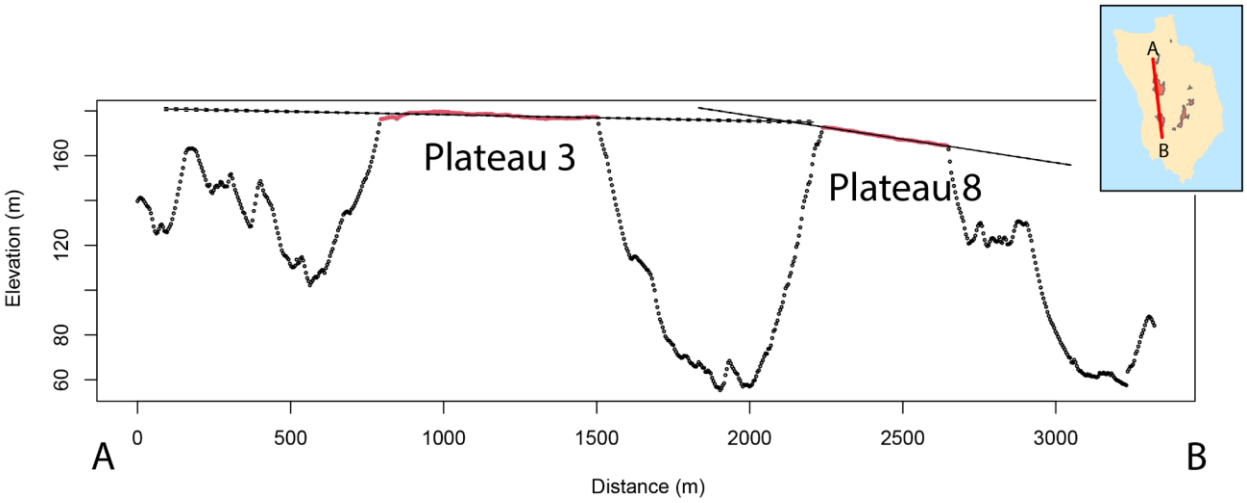

Figure 9. Elevation Profile of Plateau 3 and 8, showing projected surface alignment. Profile locations are shown on the mini map and Figure 3. The surfaces are moderately aligned, with a possible change in slope between the two plateaus.

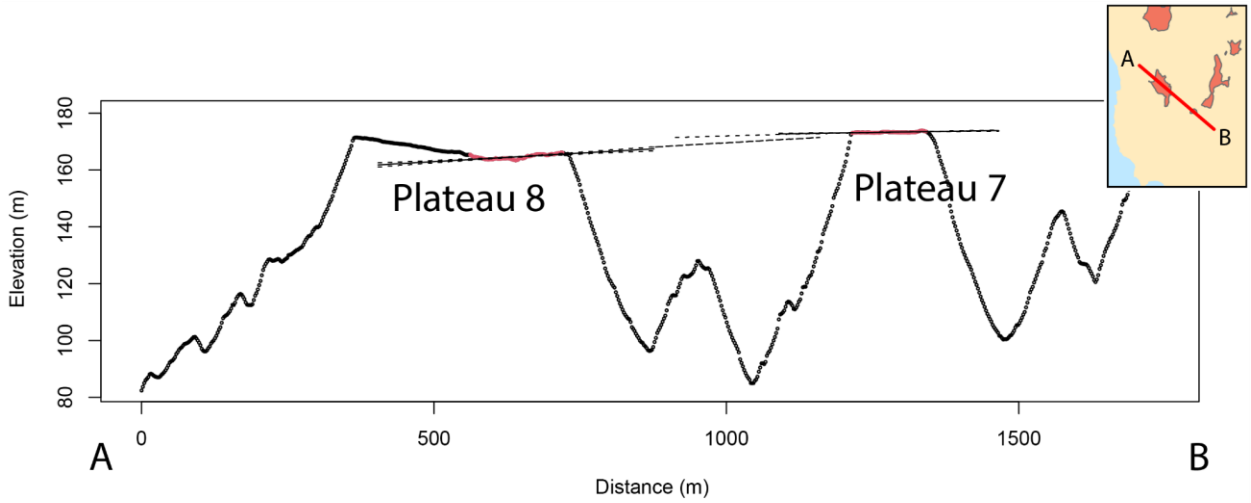

Figure 10. Elevation Profile of Plateau 7 and 8, showing projected surface alignment. Plateau 7's surface shows good alignment with the eastern surface of Plateau 8.

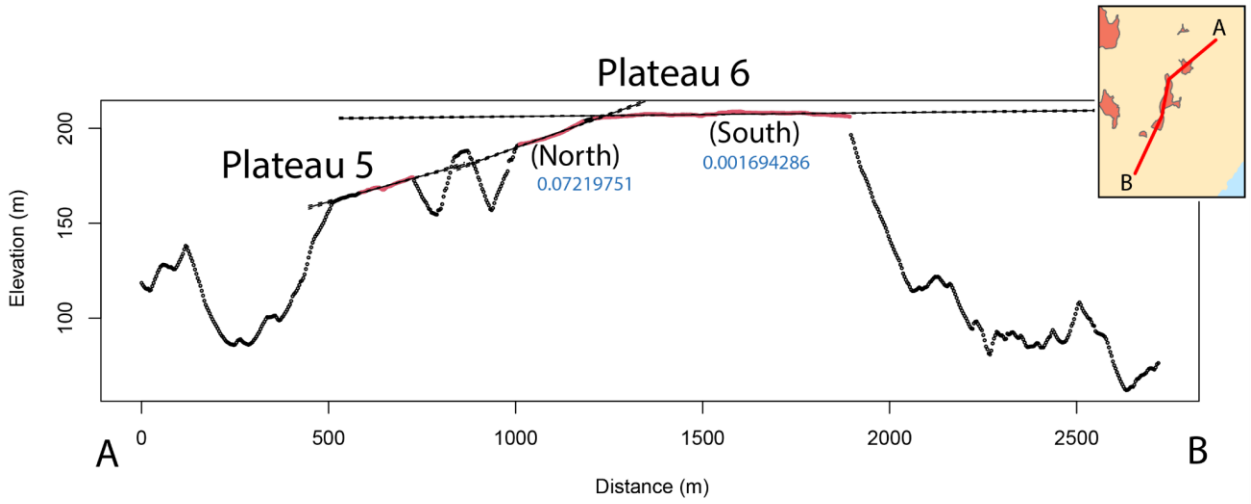

Figure 11. Elevation Profile of Plateau 6 and 7. The sloped (0.0722) northern half of Plateau 6 shows good alignment with Plateau 5, but flatter (0.00169) southern half of Plateau 6 does not. The southern surface likely was formed during the relatively stable sea level period, while the northern slope represents the initiation of uplift.

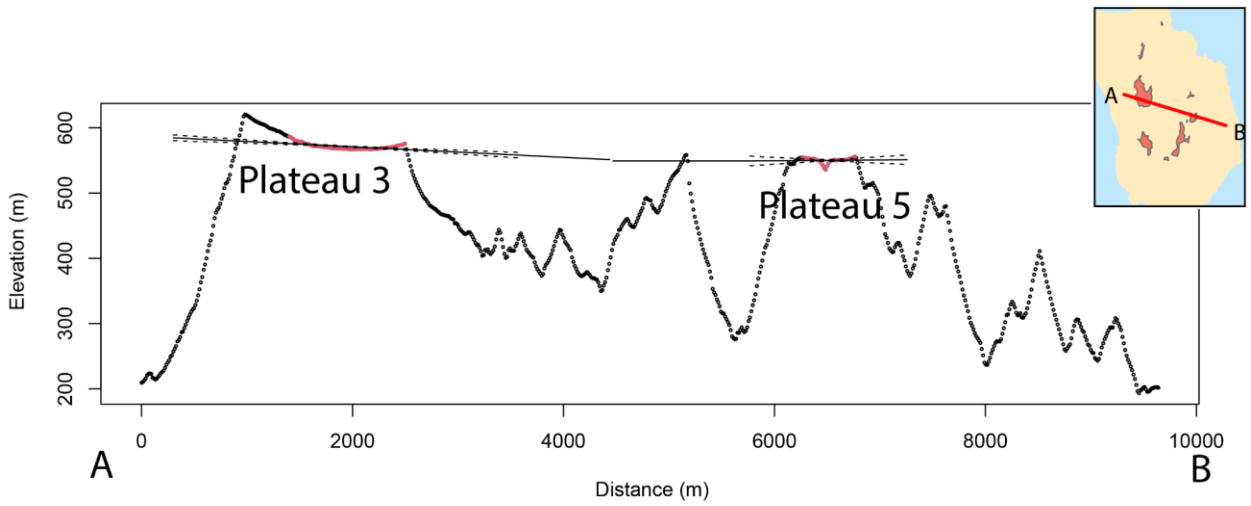

Figure 12. Elevation Profile of Plateau 3 and 5. Projected surfaces show moderate to good alignment.

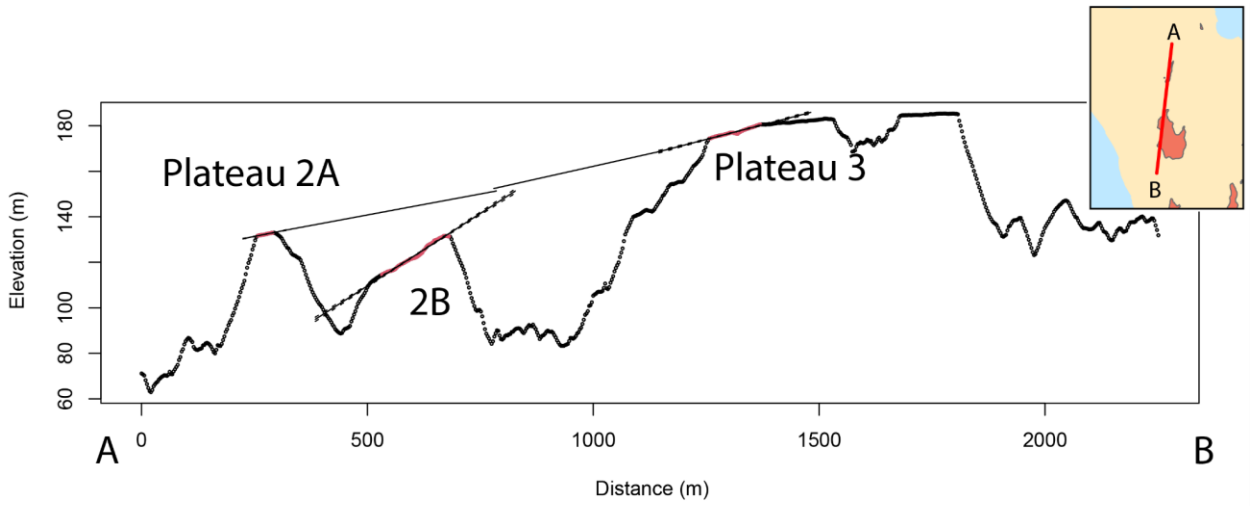

Figure 13. Elevation Profile of Plateau 2A, 2B, and 3. The northern part of Plateau 3 shows changes in slope, contrast to the rest of the plateau's relatively flat topography. This sloped northern section shows good alignment with Plateau 2A, and poor alignment with 2B.

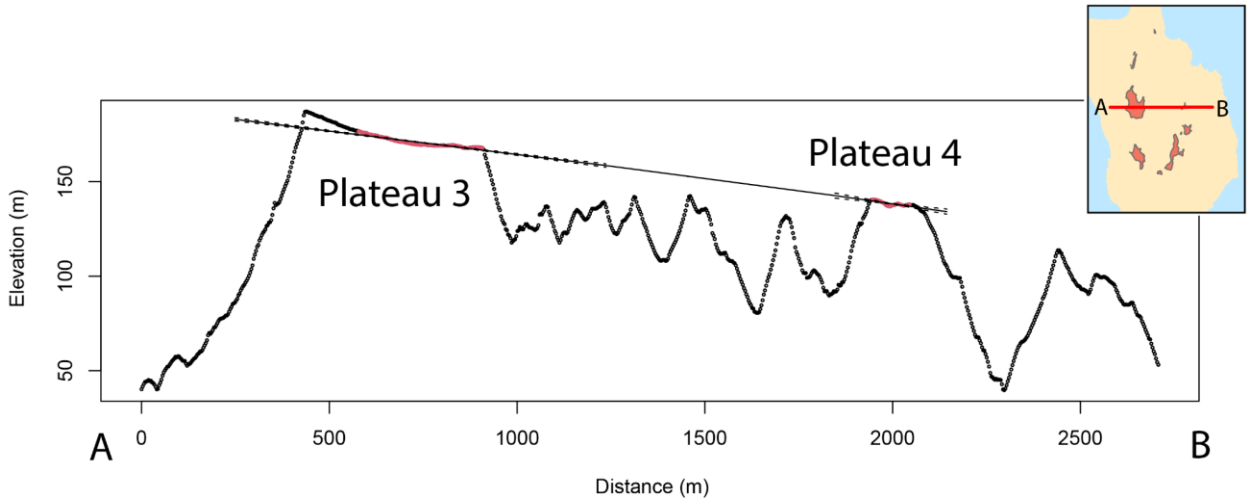

Figure 14. Elevation Profile of Plateau 3 and 4. The projected surfaces show good alignment.

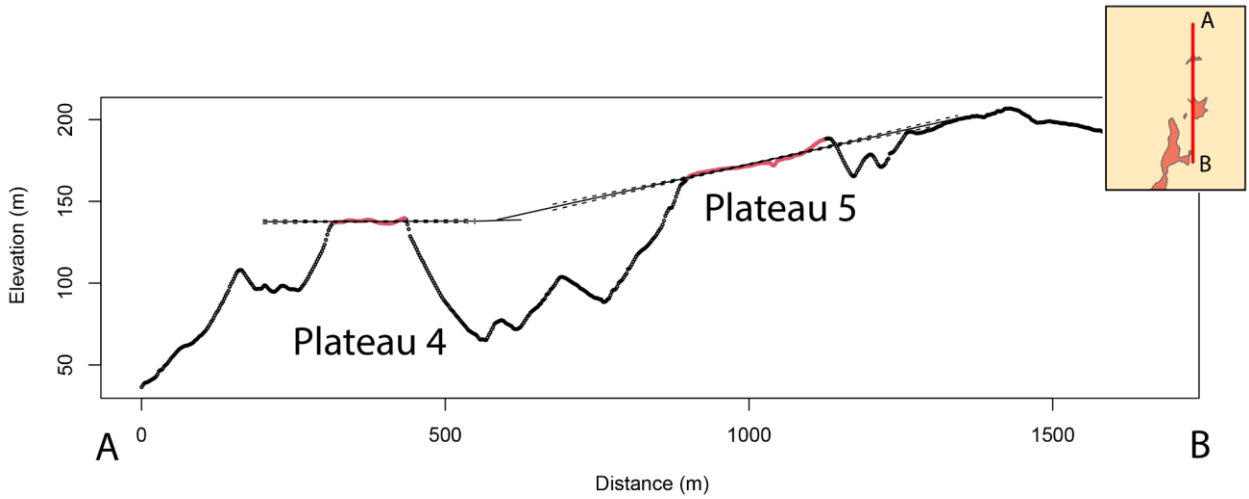

Figure 15. Elevation Profile of Plateau 4 and 5. The projected surfaces show moderate alignment, with possible change in slope between the plateaus.

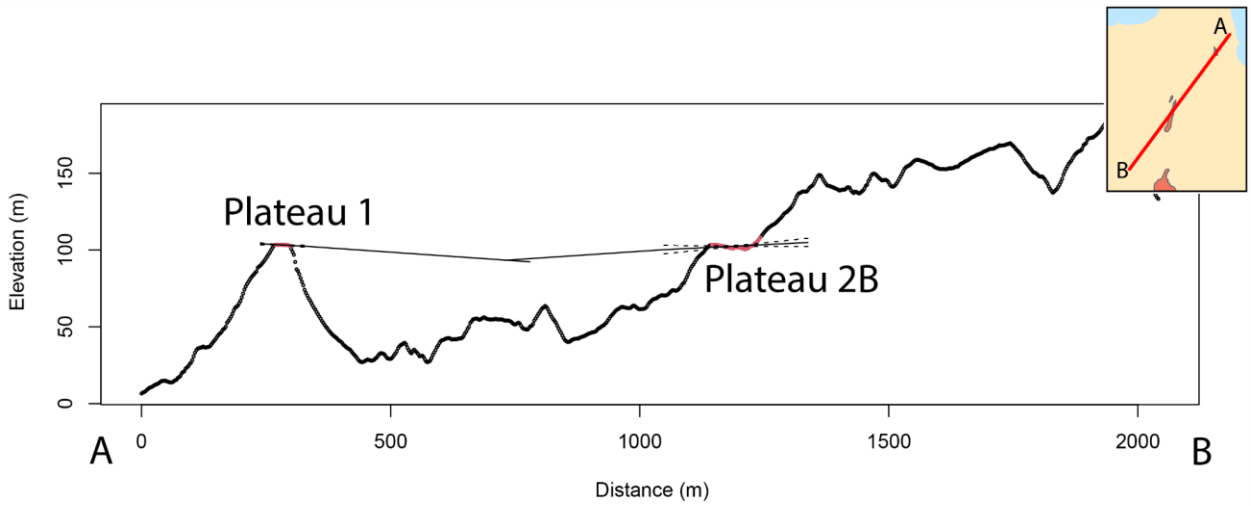

Figure 16. Elevation Profile of Plateau 1 and 2B. The projected surfaces show moderate to good alignment, but uncertainties are high due to poor preservation of Plateau 1.

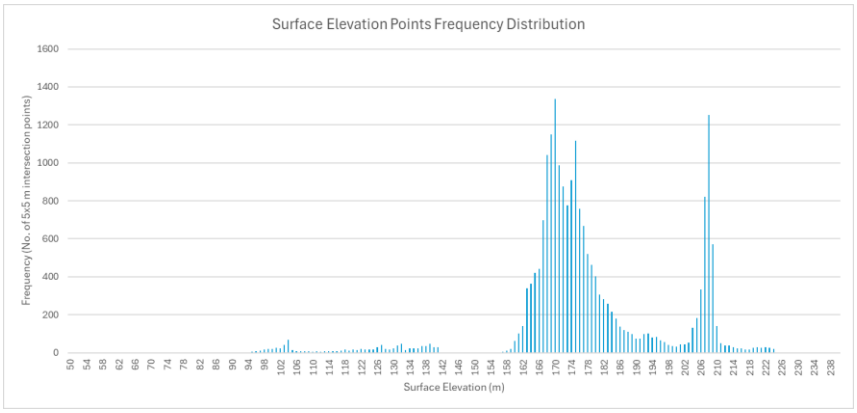

A)

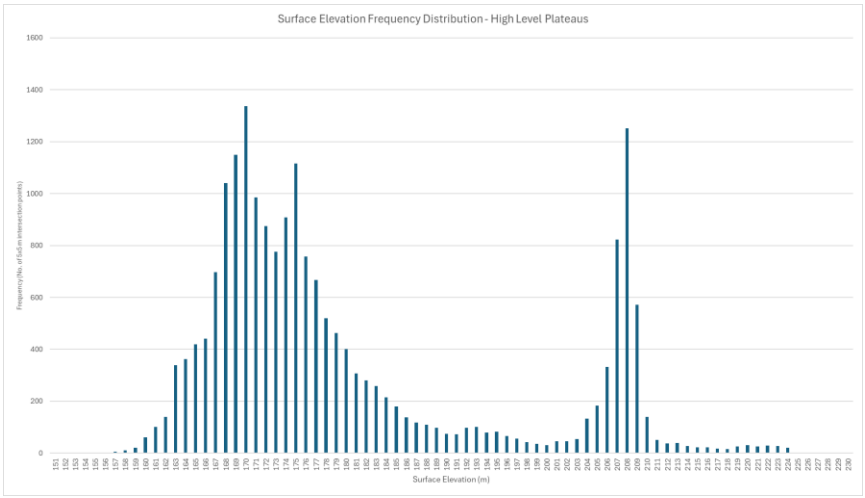

B)

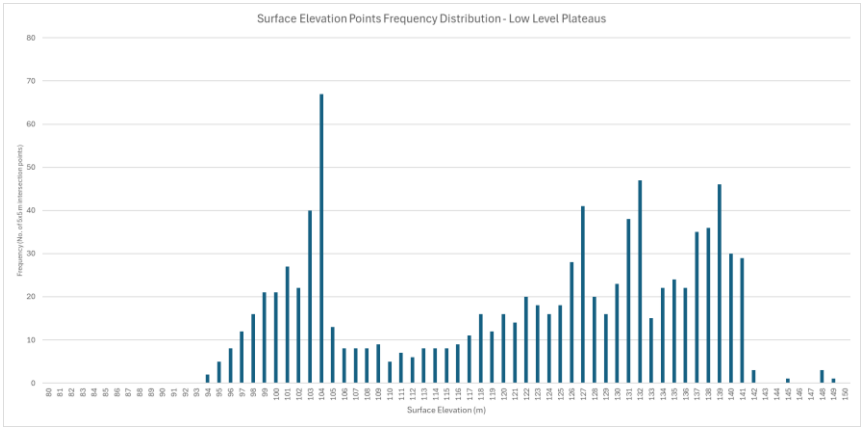

C)

Figure 17. Frequency Diagram of Surface Elevation Distribution. Data points are extracted from 5x5 m grid points with assigned elevation values based on DEM. A) shows frequency distributions of all surface elevations, B) shows isolated frequency diagram of elevations higher

than 150 m, and C) shows elevations equal to or lower than 150 m. Note the tight cluster of the highest elevation curve and the more deviated bell curves of lower elevation curves.

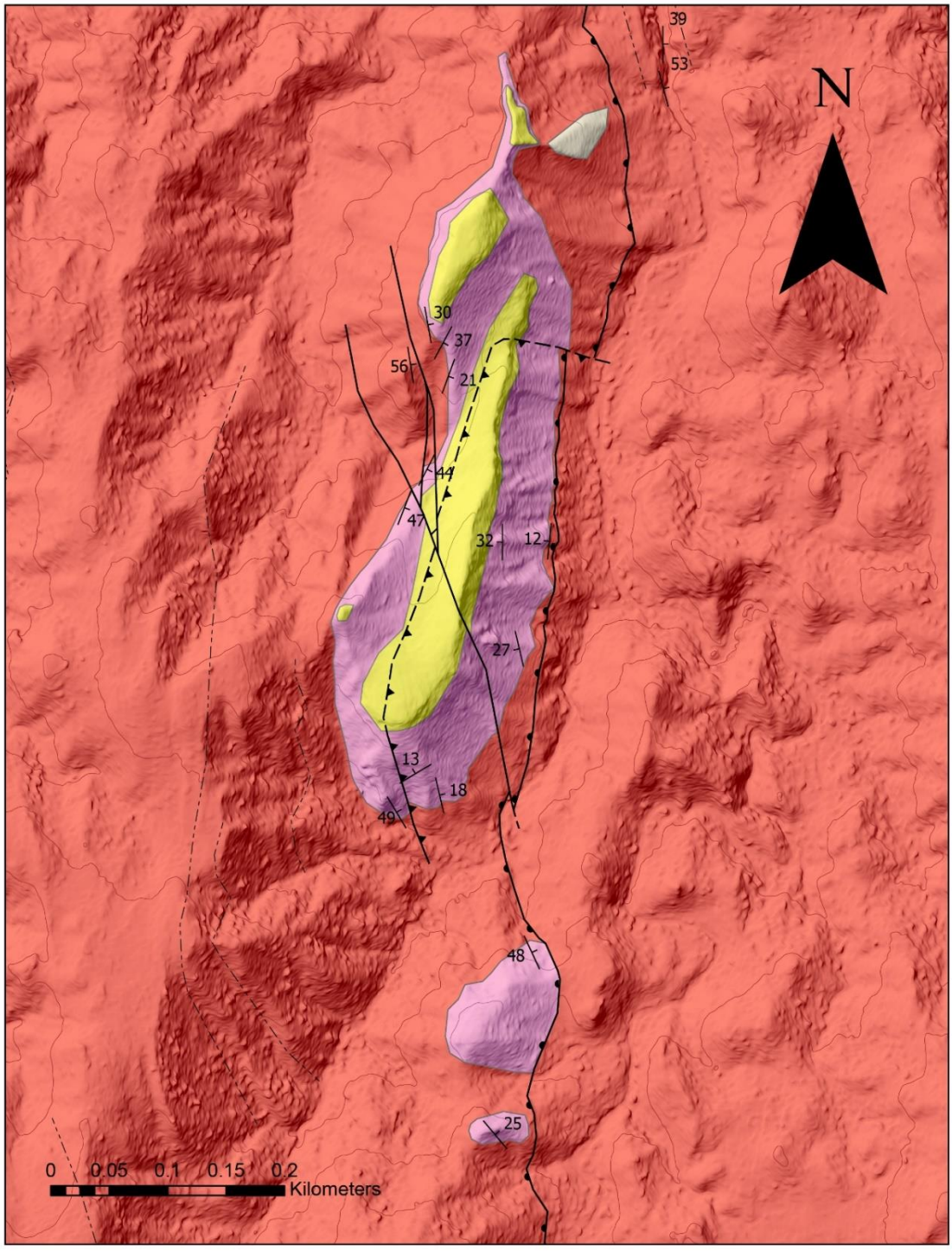

Figure 18. Expanded geological map of Plateau 2 and the surrounding area. Legends are the

same as Figure 2. Low angle detachment fault controls the basin that accommodates tuff and carbonate deposition. Reverse fault cuts through the plateau, offsetting trachydacite tuff but not cutting through carbonates. Note the change in dip of the tuff across the reverse fault, and the steepening-upwards trend of the beds on the eastern hillside.

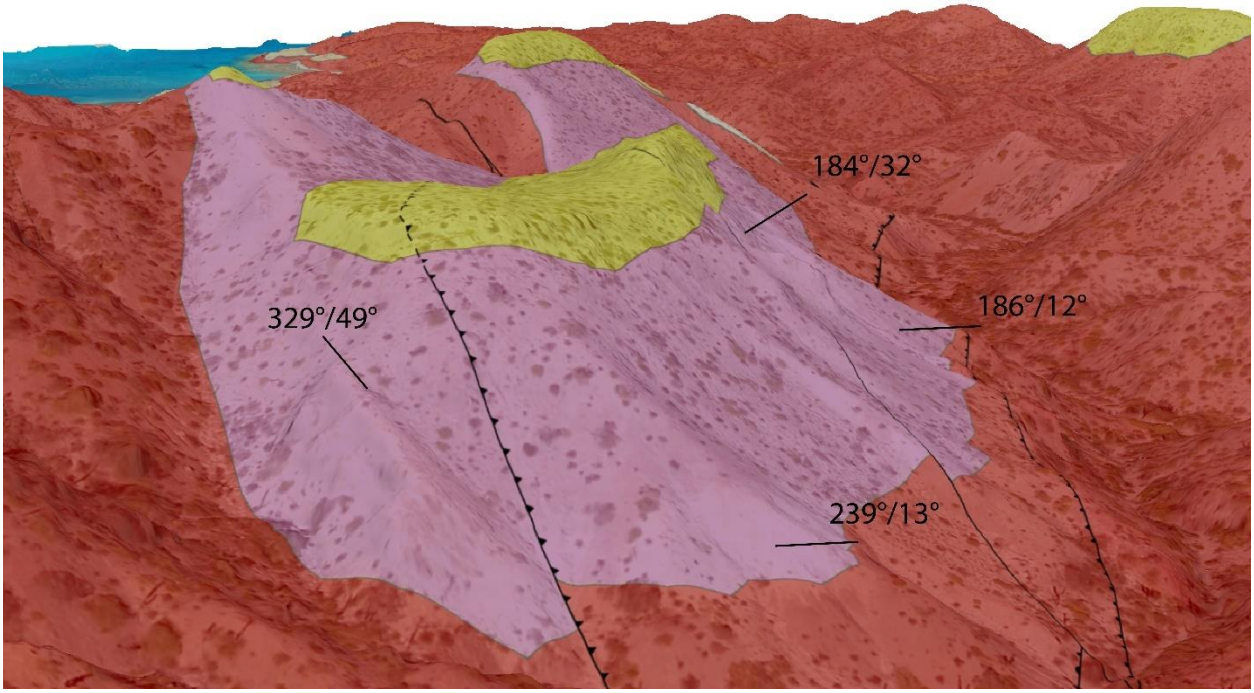

Figure 19. 3D view of Plateau 2 geology, looking NNE. The legends are the same as Figure 2. Tick mark symbols and associated numbers show strike and dip of each bed. Tuff and carbonate deposits are formed on the hanging wall of the detachment fault on the right side of the figure. The reverse fault is seen on the left side, dipping down east. Tuff on the eastern hillside progressively steepens upwards, with internal angular unconformities.

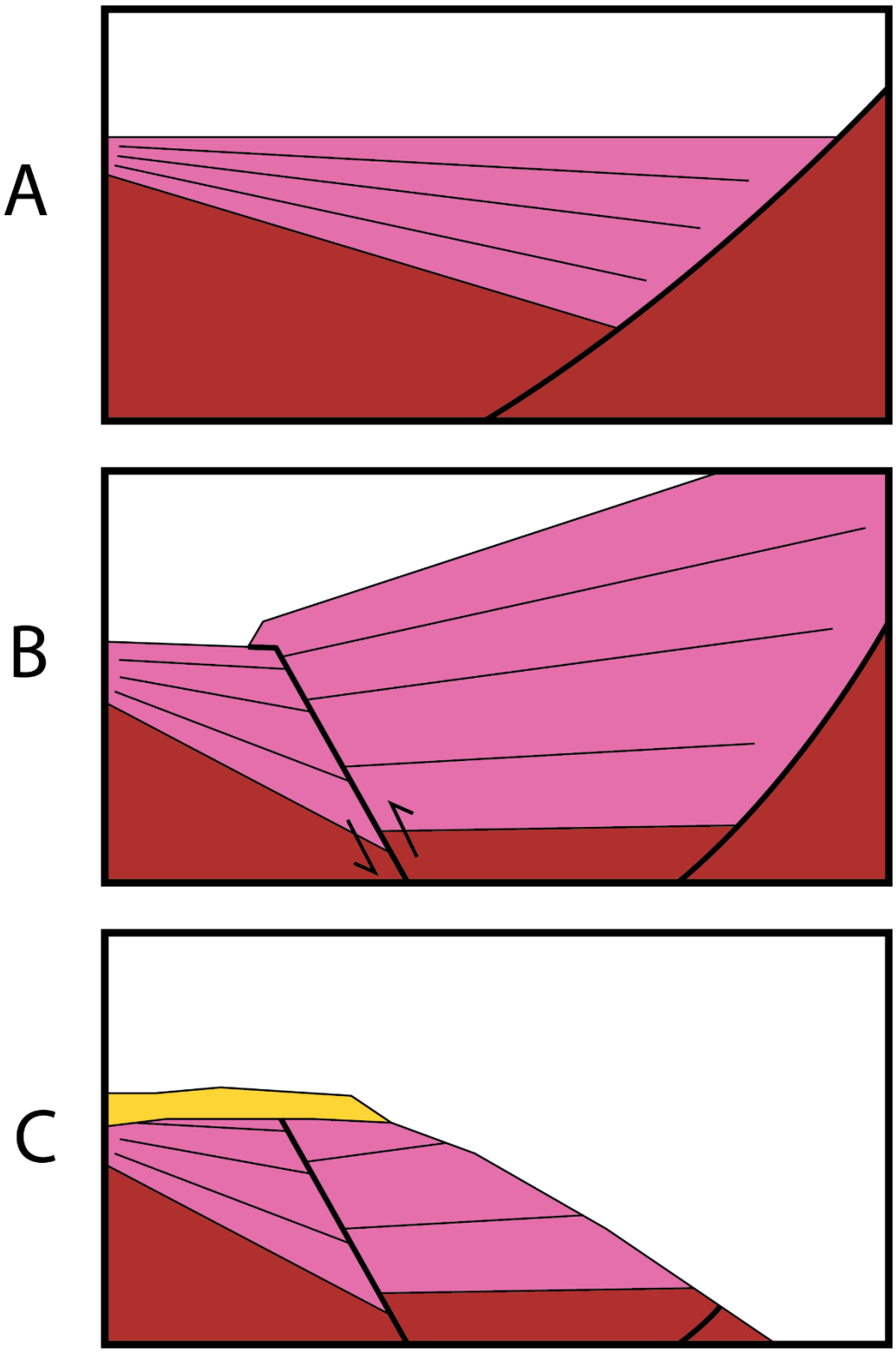

Figure 20. Schematic diagram illustrating the evolution of plateau 2 geology. Legends are the same as Figure 2. A) The tuff beds were probably originally deposited as a fanning dip, B) which was later uplifted due to fault propagation fold of the reverse fault. C) The beds were buried

underneath carbonates due to transgression, which was recently (Quaternary) uplifted and eroded.

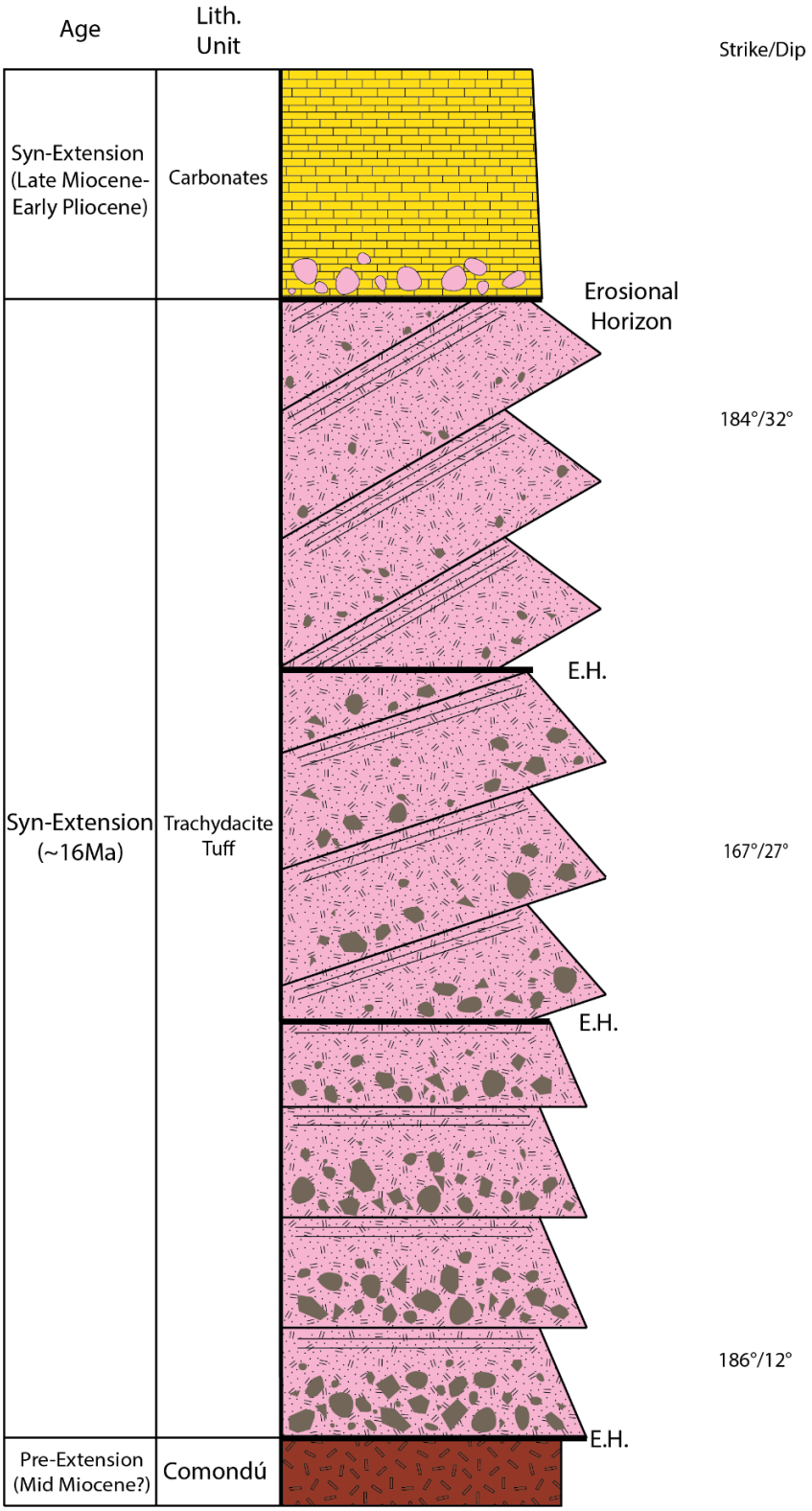

Figure 21. Schematic stratigraphic column of Plateau 2 eastern hillside section. There are at least

three tuff strata groups separated by angular unconformities. Both the individual beds and the whole section are normally graded, as can be seen by the gradual disappearance and fining of lithic fragments upwards.

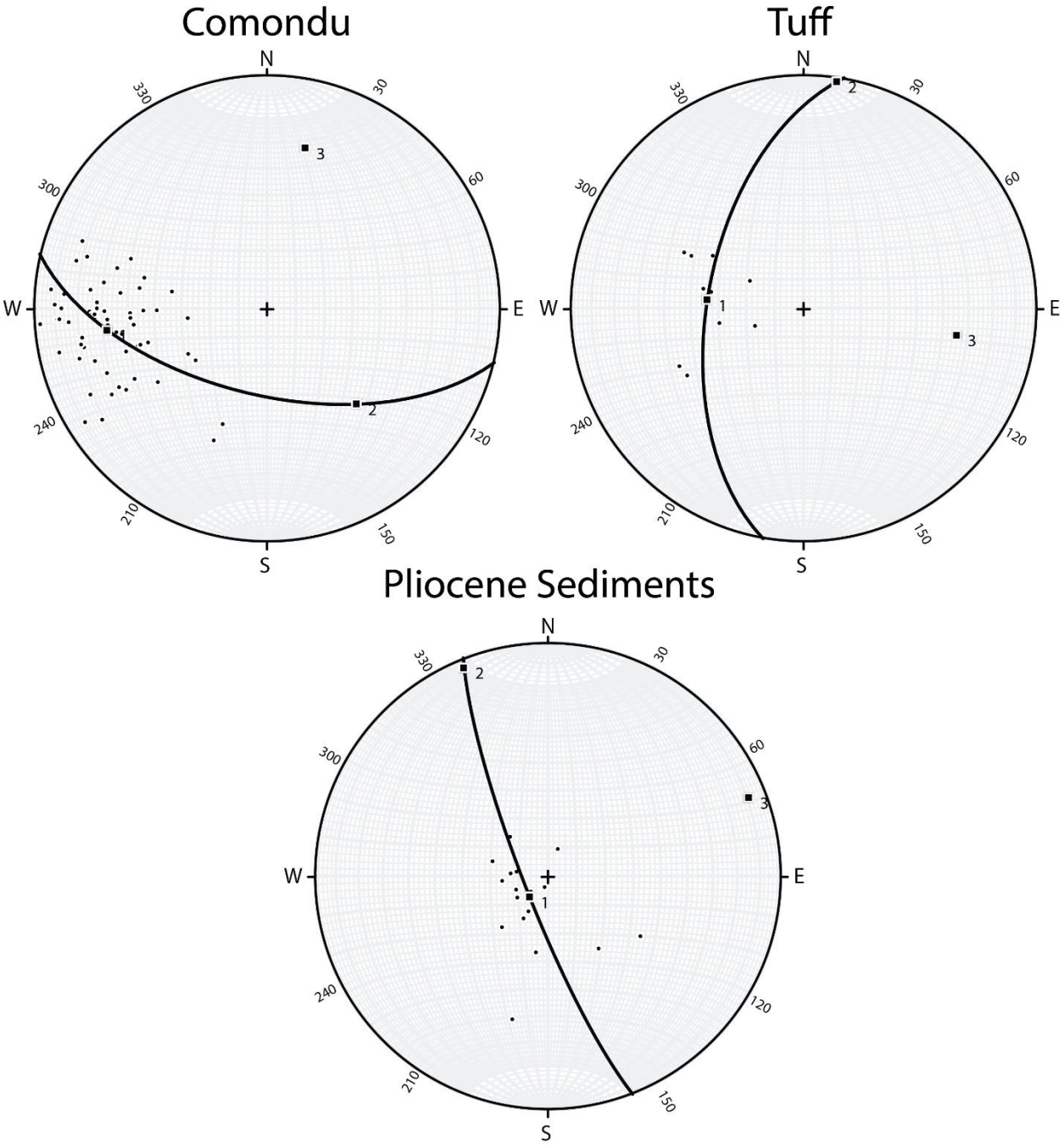

Figure 22. Stereogram showing poles drawn for bedding planes of Monserrate Comondú, trachydacite tuffs, and Late Miocene/Early Pliocene marine sediments. A tight cluster is formed around: 264°/32° for the Comondú; 274°/56° for tuff; 262°/84° for Pliocene sediments.

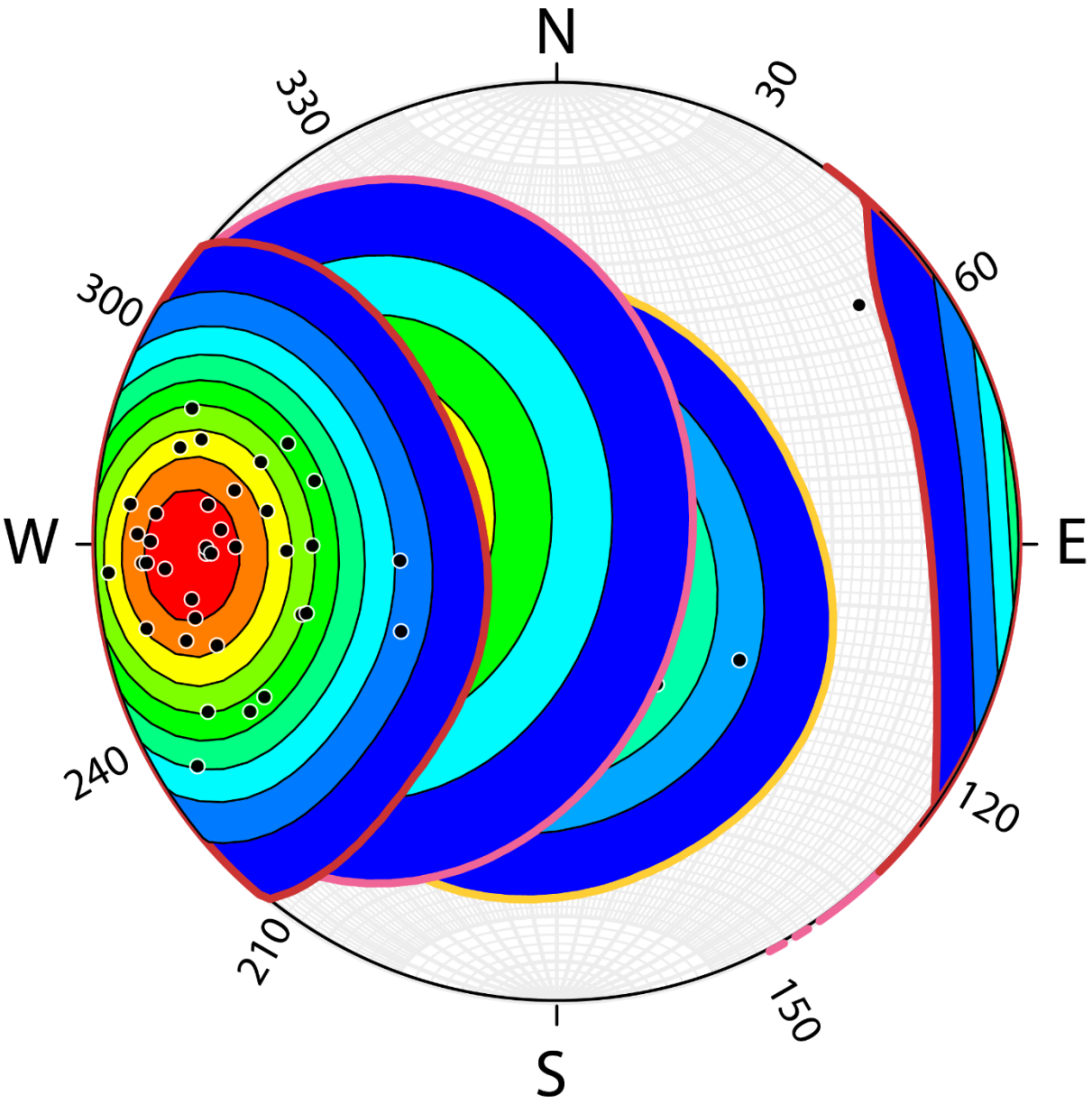

Figure 23. Stereogram showing contours drawn around the poles of Pre-extensional Comondú, pyroclastic deposits, and Pliocene deposits bedding planes, respectively represented by red, pink, and yellow boundaries. A clear, progressive sequence of steep-to-gentle dip can be observed.

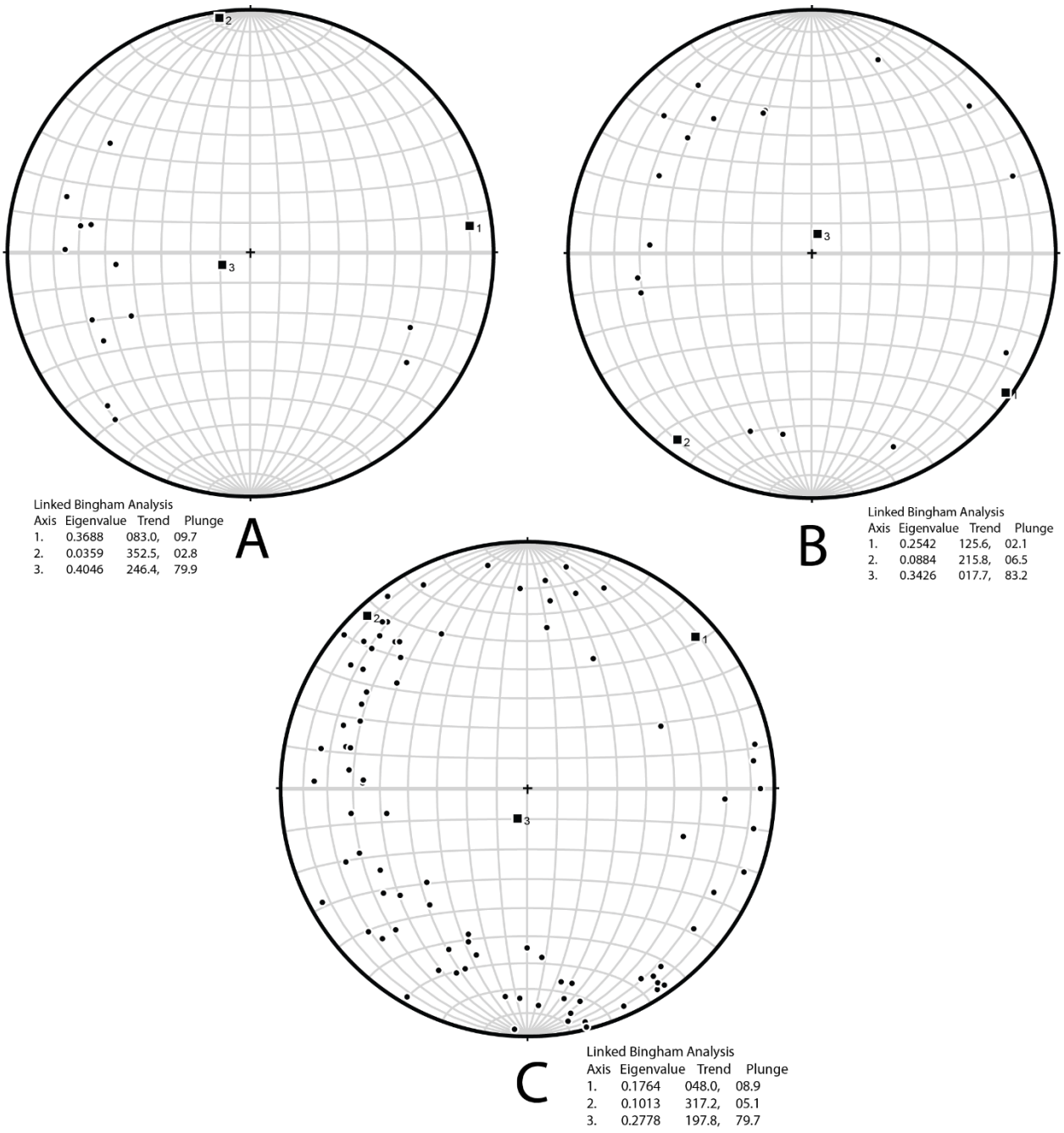

Figure 24. Striae of Monserrate Detachment Fault systems plotted on stereogram. Linked Bingham Analysis values are shown underneath each stereogram. A) Western Monserrate Detachment, B) Central Monserrate Detachment, C) Eastern Monserrate Detachment.

Figure 25. Comondú debris flow deposits, showing a mixture of various siliciclastic fragments and red sand matrix.

Figure 26. Comondú debris flow deposits with yellowish brown sand matrix. The boulder clast in the center is made of another debris flow with dark grey matrix.

Figure 27. Sample of Comondú lahar featuring a green, possibly a metaigneous lithic fragment, atypical of Monserrate Comondú volcanics. Photo from Ivan Arturo Pena Villa.

Figure 28. Reddish-brown fluvial sandstones interbedding massive, brownish-grey lahar deposits. The fluvial sands are typically medium to coarse grained, with occasional drapes of mud/silt layers. Contacts between sandstones and debris flows are typically sharp but conformable. Photograph taken looking east, from Ivan Arturo Pena Villa.

Figure 29. Yellow fluvial sandstone interbedding yellowish-brown debris flow deposits.

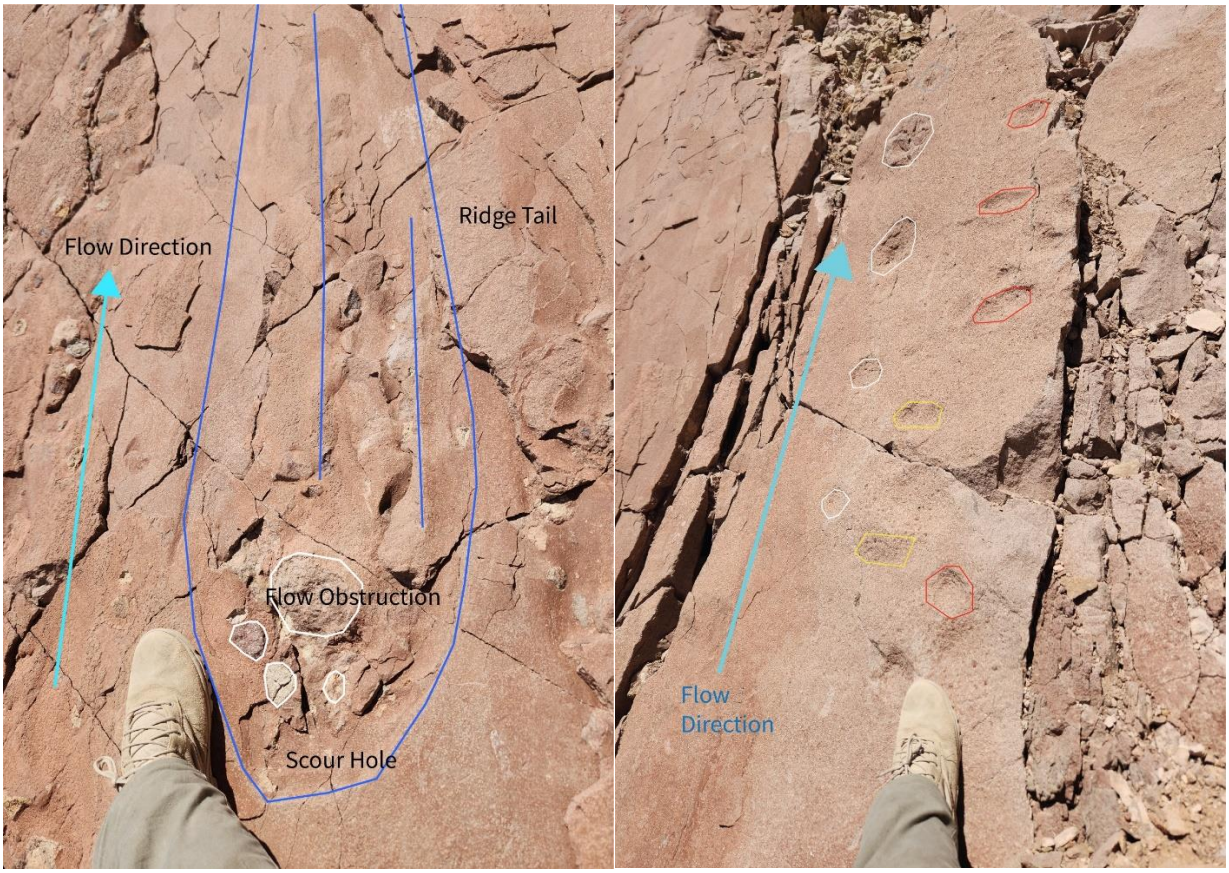

Figure 30. Flow indicators: scour marks (left) and bounce marks (right), preserved on reddish brown fluvial sandstone in the southeast coast Monserrate. For the scour marks, half-embedded clasts in the middle likely obstructed the flow of water, leading to the development of U-shaped scour holes and streamlined ridge tail downstream. For the bounce marks, saltating clasts in a water current likely bounced off the riverbed, leaving linear sets of depressions on the floor.

Figure 31. Possible worm burrows preserved in yellow fluvial sandstone, southeast Monserrate coast.

Figure 32. Comondú trachyandesite flow deposited on top of red fluvial sandstone. Photograph taken at the south coast, looking north. Note the east-dipping contact parallel with east-dipping sandstone strata. Close examination reveals chilled margin at the contact between the underlying sediments and lava flow.

Figure 33. Trachyandesite flow and overlying Comondú lahar deposits. Parts of detached trachyandesites can be seen “afloat” in the brown sandy lahar matrix. Note the lack of chilled margin.

.

Figure 34. “Hornblende porphyry” lava, exhibiting light grey colored groundmass and dark spheroidal amphibole phenocrysts.

Figure 35. “Plagioclase-porphyry” lava, exhibiting darker mafic groundmass and white, elongated plagioclase phenocrysts, approximately 5-7 mm in length.

Figure 36. Vuggy “plagioclase porphyry” lava, with ~3-5 cm diameter spheroidal vugs filled with white secondary mineral growth. Note the zone of lineated fabric, recognizable via elongated vugs.

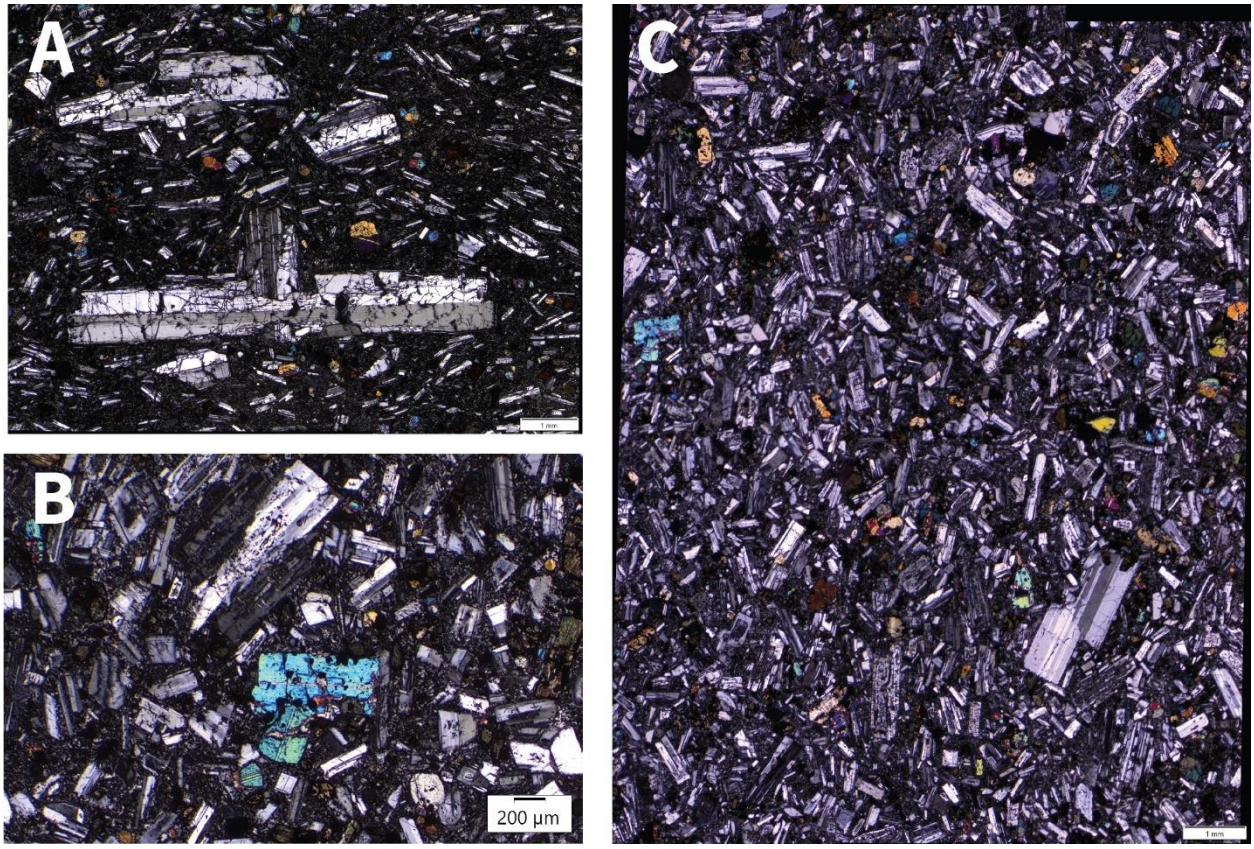

Figure 37. Cross-Polarized Light Micrograph of Monserrate trachyandesite volcanic samples. A) Thin section of ISMON SEPT 23 D18 S5. Elongated plagioclase porphyroclasts as big as ~7-8 mm can be seen. Finer plagioclase phenocrysts <1 mm in length can also be observed, making up ~30-40% of the groundmass composition. Colorful clinopyroxene phenocrysts with high birefringence are also visible. B) Close-up of clinopyroxene phenocryst in ISMON SEPT 23 D18 S8. C) Thin section of sample ISMON SEPT 23 D18 S8. Large porphyroclasts are much rarer and bulk of the composition is made of fine-grained phenocrysts, ranging between 0.1-1 mm in length. The overall composition is ~40-50% plagioclase and ~10% clinopyroxene.

Figure 38. Welded, light grey ignimbrite outcrop and its flow bandings. Lithic fragments, amphiboles, pumice, and ash groundmass can be seen.

Figure 39. Trachydacite tuff bed exposed on Plateau 2. It contains multiple Comondú lithic clasts, phenocrysts, and white, moderately welded ash matrix. Stratifications are better developed upwards. The beds are overall normally graded, as large lithic fragments are bigger and more numerous towards the base.

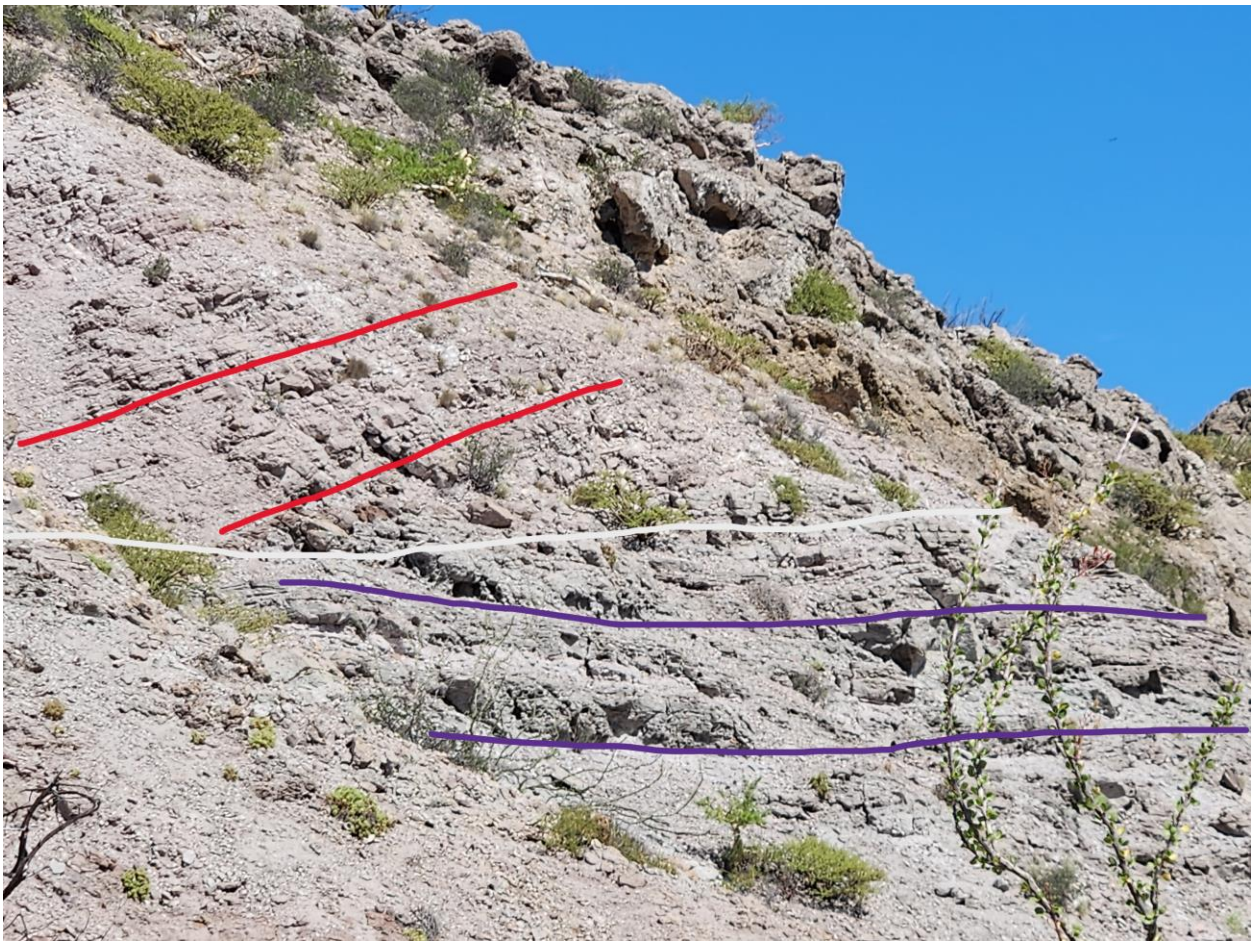

Figure 40. Trachydacite tuff beds with internal angular unconformity, exposed on the eastern hillside of Plateau 2. White line shows the approximate location of erosional horizon. Red and purple lines show the approximate orientation of upper strata group and lower strata group, respectively. The section was likely formed as a fanning dip sequence dipping down east, which was later uplifted and tilted to the west.

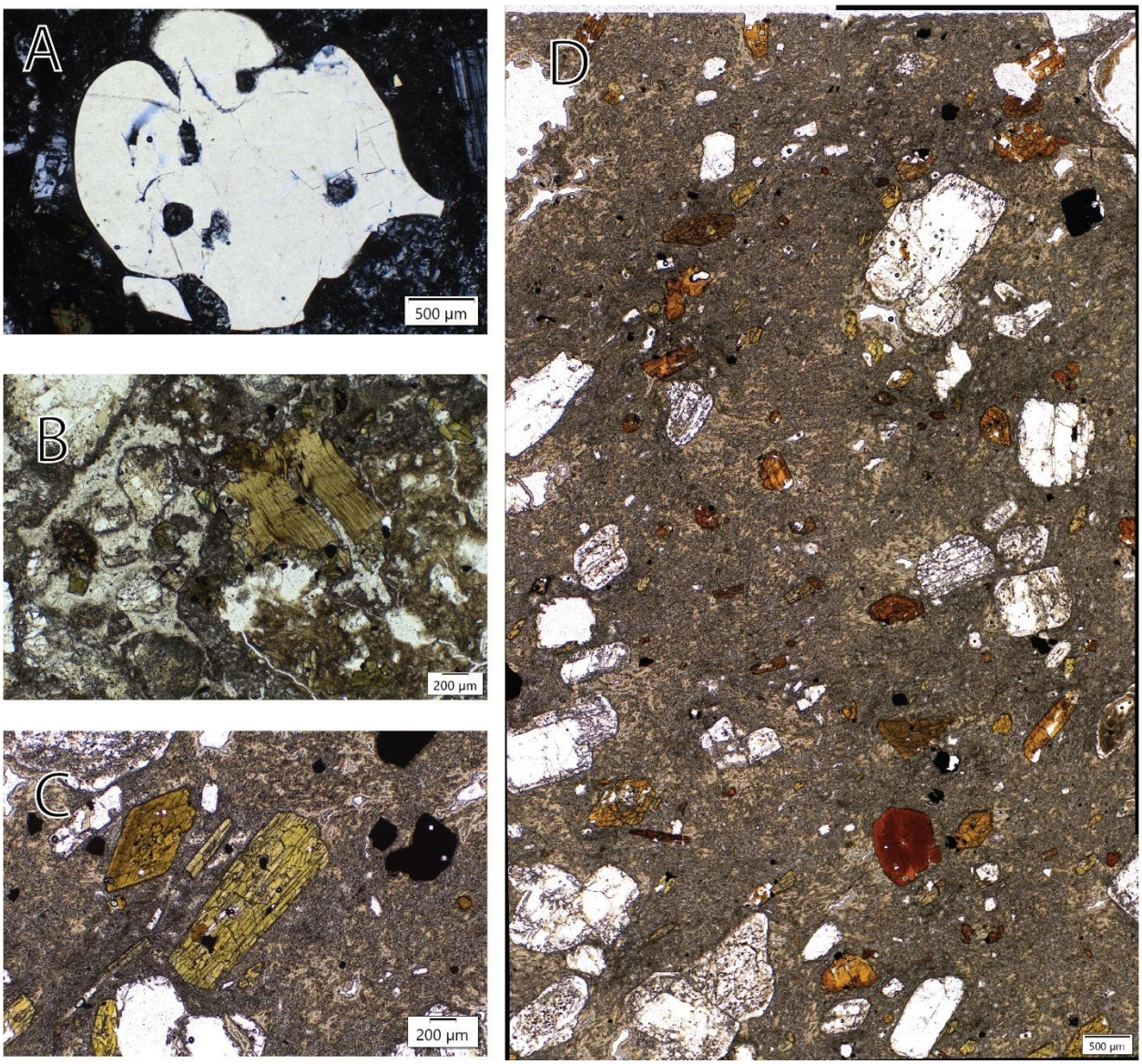

Figure 41. Photomicrographs of trachydacite tuff samples. A) Resorbed, embayed quartz from sample ISMON SEPT 23 D16 S1 under cross polarized light. B) Biotite from ISMON 22-2 under plane polarized light. C) Greenish amphibole from ISMON 22-2 under plane polarized light. D) Photomicrograph of sample ISMON SEPT 23 D15-D, plane polarized light, showing plagioclase and amphbioles. Note the red and amber-brown color of amphiboles.

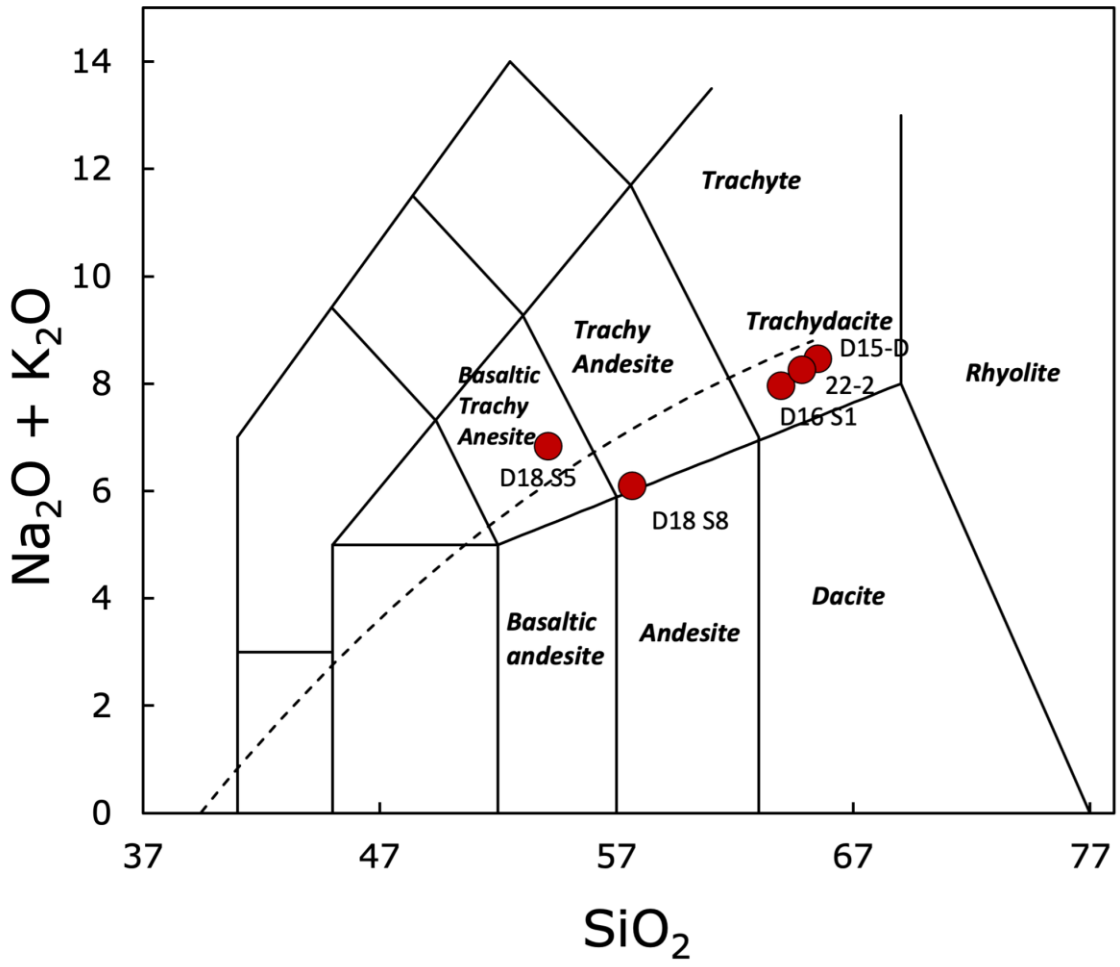

Figure 42. Plot of geochemistry analysis from the Monserrate volcanic samples, showing alkalic composition vs silicates. Lava samples D18 S5 and S8 are within trachyandesite/basaltic trachyandesite domains, while the tuff samples 22-2, D15-D, and D16 S1 are within trachydacite domain. Plot courtesy of Keith Putirka, CSU Fresno

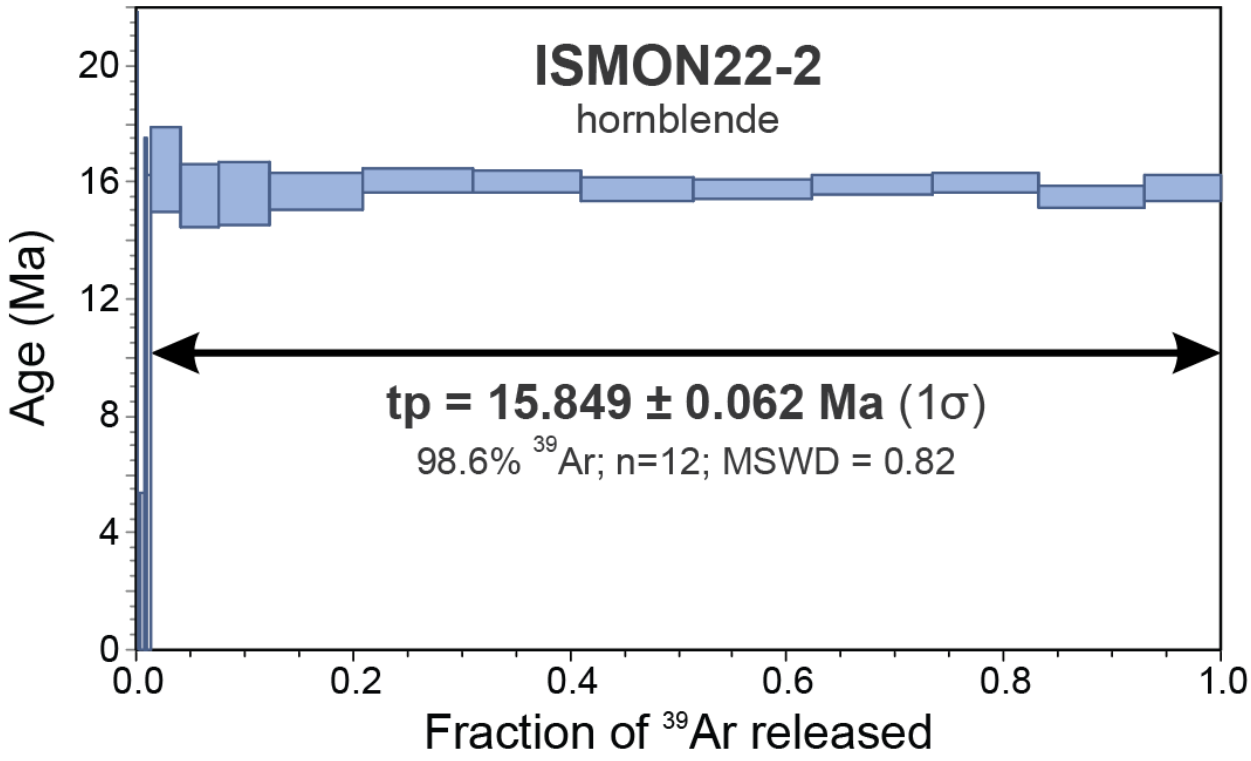

Figure 43. $^{40}Ar/^{39}Ar$ dating on Monserrate tuff sample ISMON 22-2 hornblendes, yielding a well-defined age of 15.849 ± 0.062 Ma (1σ). Plot courtesy of Teresa Orozco, UNAM.

Figure 44. Pliocene sequence basal conglomerates, overlying light grey Comondú volcanics. Clasts are composed of various siliciclastics, including Comondú and trachydacite tuff. Located on the southwest coast of Isla Monserrate.

Figure 45. Poorly sorted beds containing boulder sized brecciated clasts of various Comondú volcanics, predominantly mafic “plagioclase porphyry” lava. Depositional contact with underlying Comondú can be seen at the bottom of the figure. Matrix is filled with orange sediments typical of Pliocene marlstones. Located on the northern beach of Isla Monserrate.

A) B)

Figure 46. Rhodoliths in Pliocene marine deposits. A) Outcrop exposing rhodolith grains, ~1 mm in diameter. Located by the northern cliffside of Plateau 7. B) Thin section micrograph of rhodoliths, from sample ISMON SEPT 23 D8 JPN PL F2, retrieved from the same location of Plateau 7.

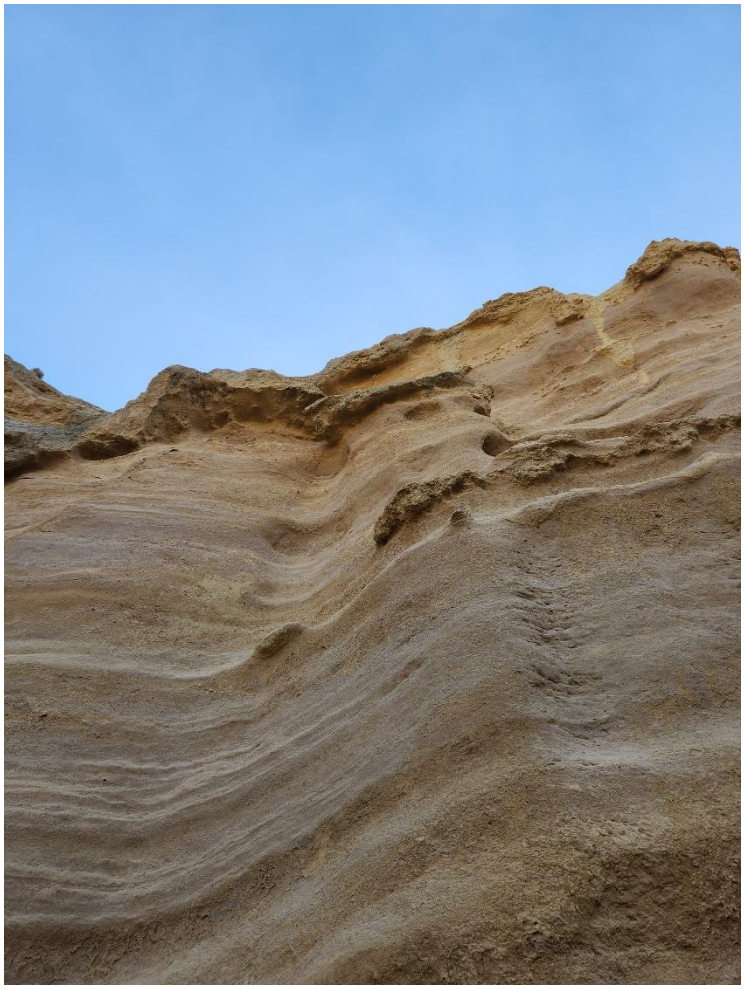

Figure 47. Yellow-orange marlstones exposed near the northern coast of Isla Monserrate. They are typically poorly lithified, with moderate stratification.

Figure 48. Coquina bed in Pliocene deposits, on the southwest coast. Arrangement of seashell fragments shows the bedding plane orientation.

Figure 49. Coquina bed, with a possible armored mudball structures composed of seashell fragments arranged in spheroidal orientation.

Figure 50. A gastropod fossil mold in Pliocene marine beds. Calcitic materials have likely been all dissolved away, leaving behind only the sediment mold.

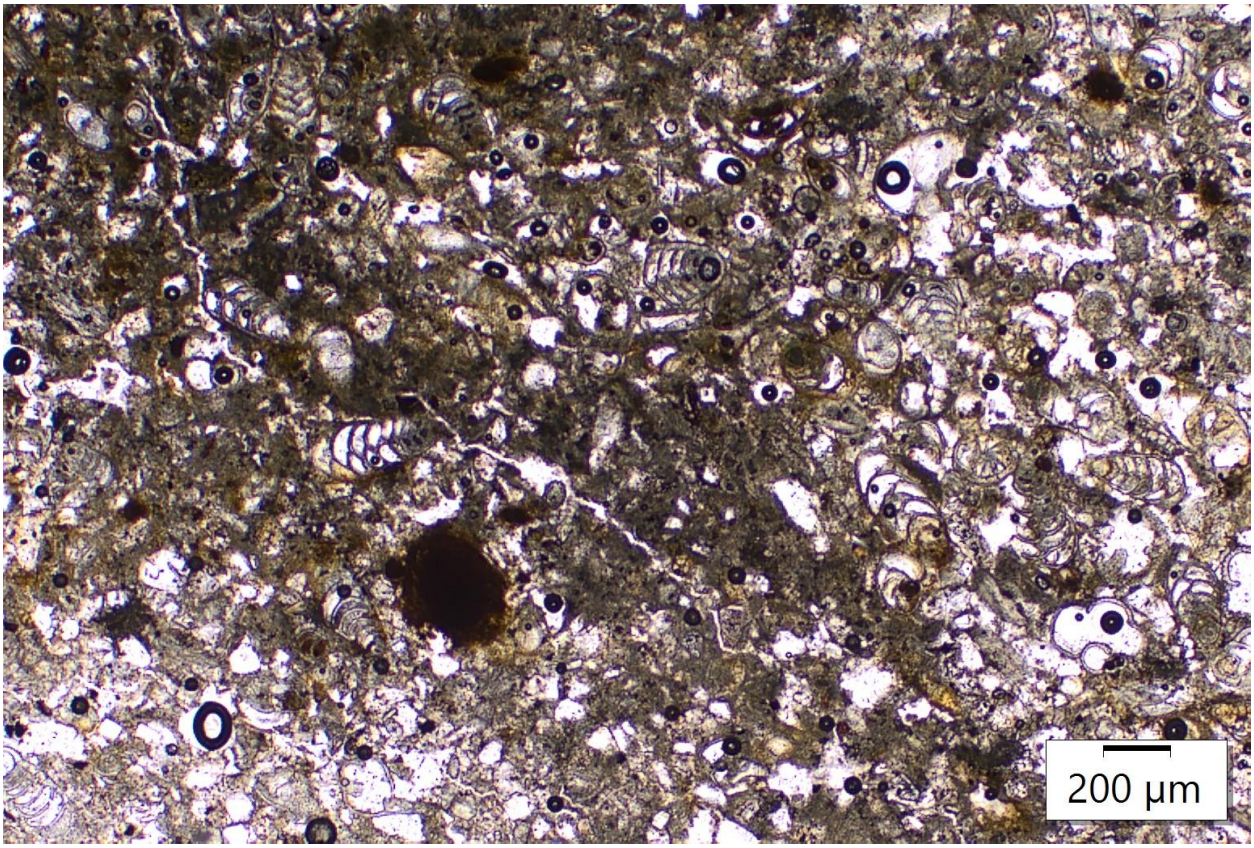

Figure 51. Photomicrograph of ISMON SEPT 23 D18 S3 thin section. Retrieved from coastal marlstone outcrop at the northern beach. Little to no lithic components can be found, and the rock is almost purely dominated by marine microfossils and loose, yellow micrite mud.

Figure 52. Level 1 terrace, with different bedrocks. Sharp, indurated carbonates have only developed on top of Pliocene marine deposits, but not on Comondú volcanic (dark bedrock) and volcaniclastic (brown bedrock in the distance) deposits.

Figure 53. Depositional contact between Pliocene bedrock and overlying terrace sediments. Both Pliocene deposits and quaternary terrace deposits have been indurated due to calcareous materials undergoing weathering and recrystallization process. They are distinguishable due to basal conglomerate layer of terrace sediments.

Figure 54. An outcrop exposing Pliocene marlstone and indurated carbonate layer. A bedding of marlstone can be seen extending into the grey indurated carbonate, demonstrating the well-cemented carbonates are not separate deposits but rather, a product of marlstone diagenesis.

Figure 55. Elevated plateau carbonates and underlying Comondú. A sharp, horizontal depositional contact is clearly visible.

Figure 56. A biostrome outcrop on the eastern cliffside of Plateau 6, showing abundant well-preserved skeletal fossils.

Figure 57. Brown dikes (outlined in red) found within a detachment fault core (black line), with light grey Comondú volcanics as wall rocks. At least two strands of dikes can be seen, both parallel to the faultplane. The lower dike is offset by the fault.

Figure 58. High-angle normal fault. Yellow Pliocene deposits on the hanging wall and light grey Comondú volcanics on the foot wall. Fault is clearly seen not cutting through the terrace deposits. Measurement shows the fault plane dips 51° to west. Located on the southwest coast, photograph taken looking north.

Figure 59. A white, fossiliferous, weathering-resistant marker bed in Pliocene marlstone outcrop used to estimate normal fault displacement. Offset across the fault is approximately 3 m.

Figure 60. Neptunian dikes in Pliocene marlstone, adjacent to a high-angle normal fault. The fault planes/fractures infiltrated by liquified sediments are more resistant to weathering than the poorly lithified marlstone wall rock, making them protrude more.

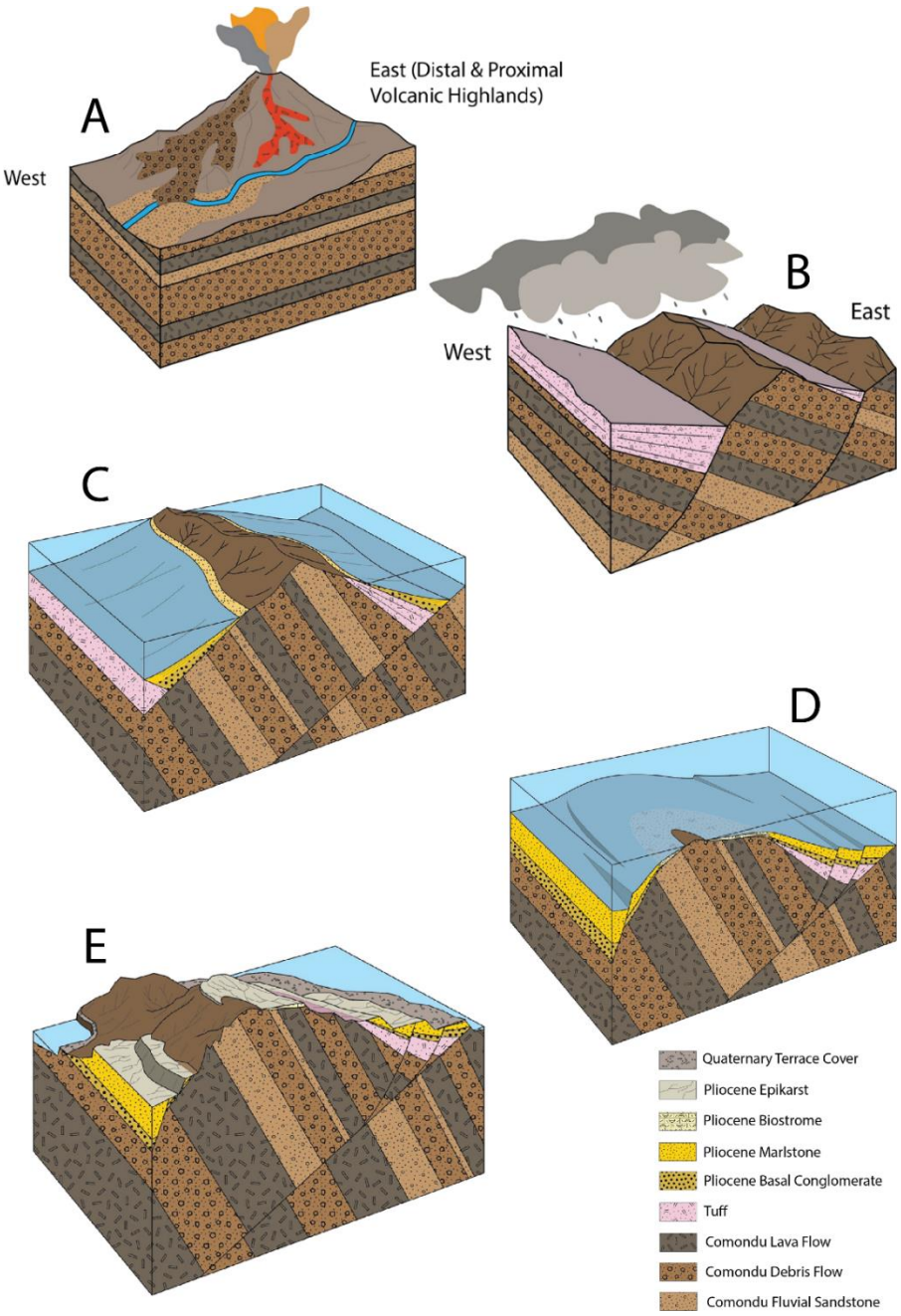

Figure 61. Schematic block diagrams showing the geological evolution of Isla Monserrate. A) Pre-Extensional Stage. Comondú lavas and lahars are deposited from subduction arc volcanism that formed volcanic highlands to the east. B) Onset of extension at ~16 Ma. Detachment faults dipping down west were initiated, rotating the Comondú volcanics. Pyroclastic units were deposited syn-extensionally. C) Continued extension and lithospheric thinning leads to the transgression of Proto-Gulf of California. Fault basins deposit thick beds of large clastic sediments. D) Submergence reaches its peak around Late Miocene to Early Pliocene. Most if not all of the landmass is below sea level, therefore thick clastic beds are no longer deposited. Instead, fossil-rich carbonate beds are developed on the reef-like shallow carbonate shelves, and fine-grained marlstones are deposited in deeper waters. Seismic deformation continued as evident by high-angle normal faults that offset marlstone deposits. E) The detachment faults on Monserrate deactivate, and the island uplifts above sea level. Shallow-marine carbonate shelves become elevated plateaus, and deep-water marlstones are exposed as orange marlstones near the coastline. Older carbonates are weathered and become indurated. By the time younger terraces are formed, sufficient landmass is pushed above water. This provides eroded sediments and fluvial transport system, depositing thicker layers of sediments on top of lower terrace surfaces.

Figure 62. A bivalve fossil on top of terrace level 1. The fossil is relatively fresh, as the colorful inner nacreous layer is still preserved.

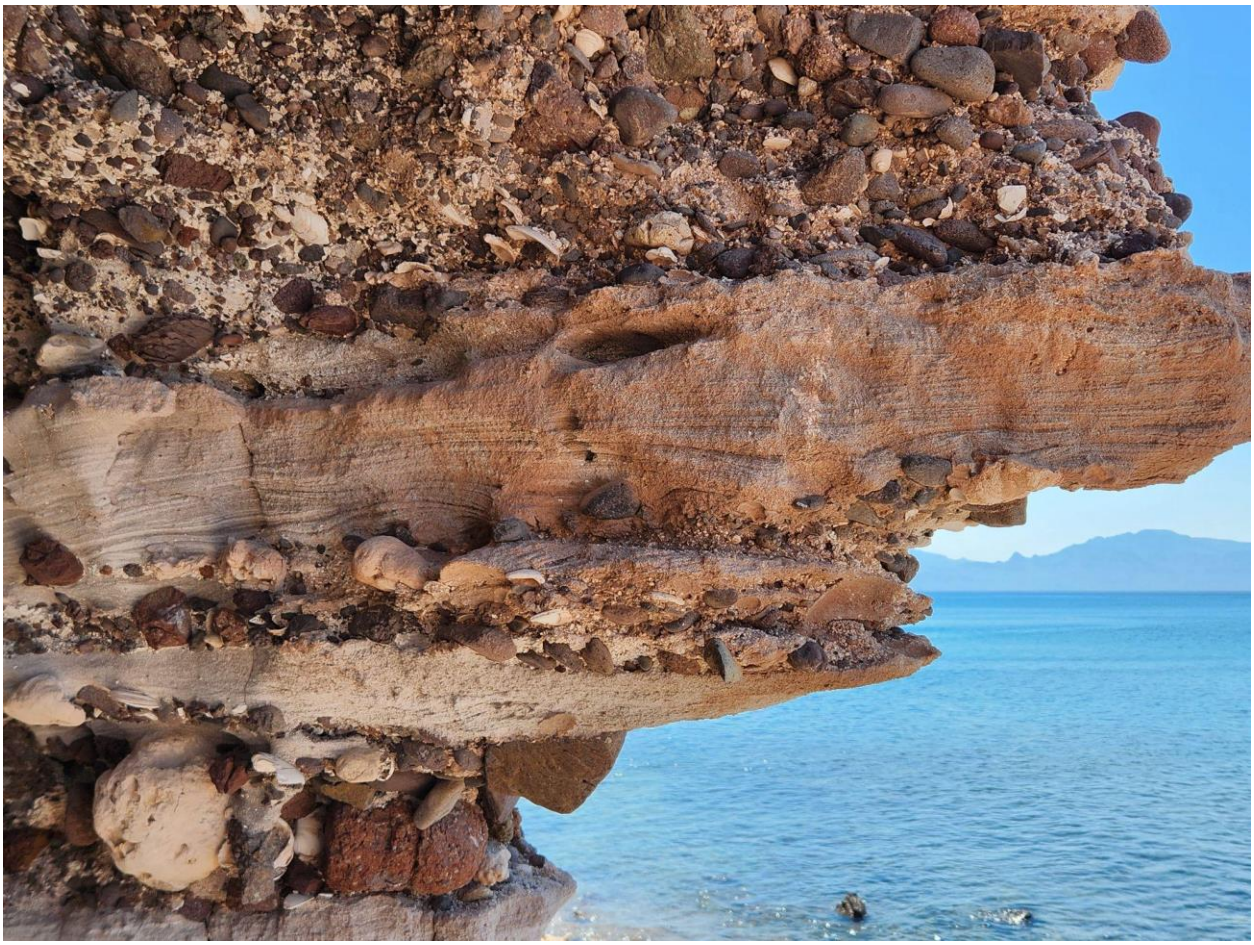

Figure 63. Sub-level 1 terrace beds. Cross laminations are present, indicating flow direction of the waves at the time of deposition. Many of the shells and elongated lithic clasts show signs of imbrication, indicating flow direction to the left (inland/east) side of the picture.

Figure 64. Eolian dunes, developing inland from the north coast sand beach.

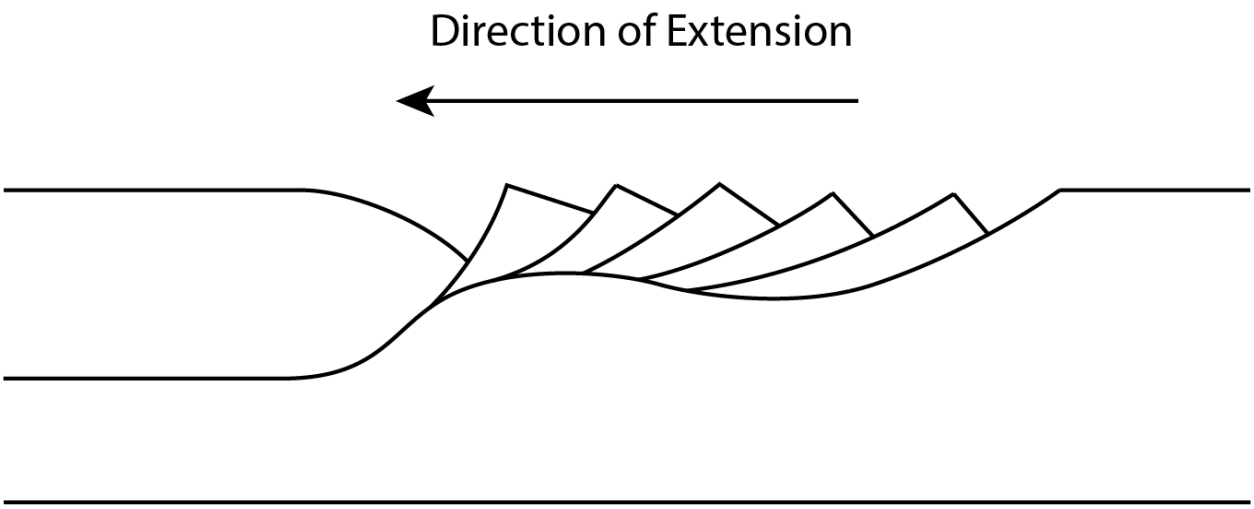

Figure 65. Graphic representation of rolling-hinge model as presented by Wernicke and Axen 1988.

Table 1. Sample Sheet – Sample Site Numbers are shown on the map Figure 2.

Sample Site Number	Sample Number	Field Description	Lat	Long		Thin Section	Geochem alab	Geochronology
1	ISMON 22-2 T1&T2	White tuff - located in the northern part of central island. Overlying basal layer with heavy conglomerate and lithic fragments composition. Well stratified. Bright tan, fine ash matrix. Matrix supported. Fairly well welded. Lithic fragments roughly 20% and phenocrysts roughly 20~30%. Elongated vesicles - pumice grains.	25.692268	-111.040469		Hornblendes, biotites, plagioclase, and rock fragments. Pleochroism. Green hornblende. Amphiboles - 120/60 degrees cleavage, up to 5.5mm, 10% composition. Another mafic mineral – iron magnesium. Plagioclase – twinning, 10% composition. Biotite – brownish yellow color, extinction, 1% trace composition.	sent batch 1	sent to Orozco
2	ISMON Dec 22-1	Red medium grained matrix. Elongated white crystals, and larger white/translucent minerals with cleavage planes - does not fizz	25.708441	-111.056802				
3	ISMON Dec 22-2	Dark reddish brown Ash/pumice clasts included within bright white/tan ashy matrix	25.708425	-111.05733				
4	ISMON Dec 22-3	Large coral fossil fragments recovered from about 1foot depth into brown top soil.	25.6547753	-111.0314052				
5	ISMON Dec 22-4	Light grey matrix with well-developed, black hornblende(?) crystals. Intrusive?	25.6547753	-111.0314052				
6	ISMON Dec 22-5	Dark brown with red hue, medium grained. Extrusive? Blocky	25.651979	-111.0287966				
7	ISMON Dec 22-6	Large coral fossil fragments recovered from about 1foot depth into brown top soil.	25.6524454	-111.0313338				
8	ISMON Dec 22-7	Large coral fossil fragments recovered from about 1foot depth into brown top soil.	25.6524441	-111.0313023				
9	ISMON Dec 22-8	Coral fossil fragments recovered from about 1foot depth into ground. Subangular to rounded, poorly sorted conglomerate clasts. Brown soil. Calcite veins nearby	25.6605214	-111.0223065				
10	ISMON Dec 22-9	Red metallic mineral with well developed cleavage planes. Dark grey matrix with fine-medium grain	25.6683304	-111.015973				
11	ISMON Dec 22-10	Light grey matrix with well developed, large hornblende(?) mineral	25.6597475	-111.0434831				
12	ISMON Dec 22-11	Red brown matrix, with white/translucent fine/medium grained minerals-does not fizz. Extrusive?	25.6949863	-111.0400925				
13	ISMON Dec 22-12	Light grey matrix. Large, translucent minerals with cleavage planes- fizzes	25.6935023	-111.0302791				
14	ISMON Dec 22-13	Dike? Light grey andesite with red oxidation bands. Blocky. Fine grains	25.6928052	-111.02946				
15	ISMON Dec 22-14	Well rounded clasts in light ash tuff. Conlgomerates in rhyolite flow?	25.6998465	-111.039955				
16	ISMON Dec 22-15	Coarse, light brown matrix with angular, poorly sorted dark clasts. Hornblende and pumice?	25.6971357	-111.041599				
17	ISMON SEPT D1 S1	Fossiliferous limestone	25.6955714	-111.0226875				
18	ISMON SEPT D2 S1	Dike in the damage zone of detach fault	25.6668307	-111.0171914				
19	ISMON SEPT D2 S2&3	Vugs with minerals (plag?)	25.6688278	-111.0177851				
20	ISMON SEPT D5 S1	Pink Tuff	25.6984838	-111.0408072				

21	ISMON SEPT D5 S2	Pink tuff fresh surfaces all around	25.6985109	-111.0408052				
22	ISMON SEPT D5 S3	Pink tuff clasts in carbonate. Fossils.	25.699893	-111.0402793				Sent to USGS
23	ISMON SEPT D5 S4&4-B	Marine fossil in carbonate. Sample 4	25.6999431	-111.0404622		Corals. Seashells (leached or replaced, might have been aragonite). Pink tuff and red lava flow grains. Brachiopod fragment?		Sent to USGS
24	ISMON 23 SEPT D8 S1	Carbonate chunk with laminae	25.6751002	-111.0283177				
25	ISMON 23 SEPT D8 S2	Fossiliferous limestone. Oolitic?	25.675359	-111.0295975		Fossil fragments. Sparry calcite matrix. Forams(diamond shaped). Wackestone (lot of grains but also matrix, grains don't touch).		Sent to USGS
26	ISMON 23 SEPT D8 S3	Fossiliferous limestone. Less indurated	25.6748282	-111.0297346				
27	ISMON SEPT D8 JPN PL F1	Fossil samples from south island of Japan Plateau	25.6703415	-111.0332053				Sent to USGS
28	ISMON SEPT D8 JPN PL F2	Fossil samples from south island of Japan Plateau and oolitic limestone	25.6701523	-111.0329768		Ooids - concentric rings(?). Mostly calcite matrix, some sand(lithic) grains. Few fossil fragments?		Sent to USGS
29	ISMON SEPT 23 D10 S1	Sample of dike(?) along the fault zone sandwiched between two lahars	25.6701099	-111.0134308				
30	ISMON SEPT 23 D11 S1&S1A	Sample of hornblende porphyry	25.6708211	-111.0370144				
31	ISMON SEPT 23 D12 S1	Sample of poorly indurated surface carbonate on T1	25.6552148	-111.0350801		Micro shell fragments. Sparry calcites. Volcanic sand grains. Bright white grains that might be ooids(uncertain) - but might be foram based on lamination pattern.		Sent to USGS
32	T1 Clast	Sample of a clast in T1	25.6716436	-111.0474908				
33	ISMON SEPT 23 D13 S1	Sample of loose carbonates found in T1	25.7077702	-111.0557204		Coral fragment with white spots and radial patterns. Concentric ring grains - dark and yellow brown. Carbonate mud(micritic) and soil carbonate developing on the surface.		Sent to USGS
34	ISMON SEPT 23 D14 S1 (TT)	Sample of a tuff on surface of terrace level 4?5?	25.6978049	-111.0512135				
35	ISMON SEPT 23 D15-A	Sample of a tuff at the base of central tuff hill*. Sept 20th. * at least 4 tuff layers with changing dip - nearly horizontal at the base to ~30 dipping west towards the top	25.6968469	-111.0398094				
36	B	2nd from the bottom tuff layer	25.696815	-111.040285				
37	C	2nd from the top tuff layer	25.696815	-111.040285				
38	D	Northern central tuff hill where progressively steepening-to-the-west layers are exposed. Uppermost layer with roughly 30 degrees west dip. Transitions upwards into pink tuff that underlies carbonate plateau surface. Similar to ISMON 22-2 except little to no lithic fragments and no pumice grains. Dark brown phenocrysts - hornblende?	25.696815	-111.040285		Amphiboles - brown hornblende (different chemical composition implied), unaltered, 6-7mm phenocrysts, 10% composition. Plagioclase 10%. No pumice. No biotite. 6 relict glass shards - Vitroclastic texture in the matrix.	batch 2, 2/24	
39	(Alpha)ISMON SEPT 23 D16 S1	Pink tuff. Located at the base of terrace forming tuff, on the cliffside by arroyo at the northwestern section of the island. Above fault contact with Comondú Group volcanics. Medium to well stratified - interbedded white and pink strata. Well welded. Light pink ash matrix. Matrix supported. 30-40% phenocrysts. Little to no lithic fragments. 4-5mm hornblendes and plagioclase.	25.6936972	-111.0491937		Fresh plagioclase. Resorbed quartz, embayed, 2mm, could be xenocryst. Lithic fragments. Hornblende has opaque rims to conmpletely replaced.	batch 2, 2/24	

40	ISMON SEPT 23 D16 S2	Corals	25.688889	-111.052222		Sand grains in the middle likely the cavity. Long striped white fossil fragment.		Sent to USGS
41	ISMON SEPT DAY 18 S1	Sandstone fossil shells	25.7072882	-111.0553148				
42	ISMON SEPT 23 D18 S2	Plag porphyry suspended in ss	25.7076931	-111.0554703				
43	ISMON SEPT 23 D 18 S3	Sandstone sample - fossils absent, poor cementation	25.707141	-111.0529847		Microfossil(?)- long elongated shell sutures? Might be forams. Sand grain dominant. Grainstone. Foram fossils. Biotite, quartz, and sparry calcite matrix.		Sent to USGS
44	ISMON SEPT 23 D 18 S4	Sandstone near fossils	25.7074406	-111.0551597		Radiolarian and Foram. Cone shaped fossils. Quartz, hornblende, biotites, calcite grains. A lot of cone shaped fossils and sutures(?).		Sent to USGS
45	ISMON SEPT 23 D 18 S5	Dark grey plag porphyry. Located at the northern part of west coast. Likely a mafic Comondú Group lava flow. Dark grey (mafic color index) aphanitic matrix. Large elongated phaneritic phenocrysts - nearly a centimeter long. 30~40% phenocrysts.	25.6993463	-111.0578302		Plag porphyry. Fresh plagioclase. Up to 6-7mm. Mafic minerals – clinopyroxenes.	batch 2, 2/24	to date?
46	ISMON SEPT23 D18 S6	Bright white hornblende porphyry	25.6554623	-111.0360253				
47	ISMON SEPT 23 D18 S7-1 &2	Hornblende porphyry	25.706206	-111.0329385				
48	ISMON SEPT 23 D18 S8	Located in the south coast. Dark brown lava flow overlying well-bedded, reddish brown fluvial sandstone. Fine phenocrysts - plagioclase and hornblendes(?).	25.6519342	-111.0286943		Crystal rich but small crystals (too small to sperarate?). Plagioclase - fresh, 0.1~1mm phenocrysts, 40~50% composition. High Bi-refringence for clinopyroxene, 10% composition.	batch 2, 2/24	to date?

Table 2. Table of macrofossils found on Isla Monserrate, organized based on their locations. Ages are shown on the rightmost column, data taken from https://paleobiodb.org

	Elevated Plateaus	**Coastal Deposits**	**Terrace Deposits**	**Age**
Argopecten sp.	x	x	x	34-0 Ma
Argopecten revellei	x			5.3-2.6 Ma
Argopecten percarus		x		5.3-2.6 Ma
Argopecten mendenhalli	x			5.3-3.6 Ma
Glycymeris sp.			x	122-0 Ma
Glycymeris maculata			x	3.6-0 Ma
Glycymeris gigantea	x		x	5.3-0 Ma
Lottia atrata	x			5.3-0 Ma
Lyropecten sp.	x	x	x	83-1.8 Ma
Nodipecten sp.	x	x	x	28-0 Ma
Nodipecten subnodosus	x			5.3-0 Ma
Hyotissa sp.	x	x		89-0 Ma
Clypeaster sp.	x			41-0 Ma
Clypeaster bowseri	x			5.3-3.6 Ma
Spondylus sp.	x		x	251-0 Ma
Megapitaria sp.			x	13.8-0 Ma
Chione sp.			x	59-0 Ma
Chione californiensis			x	5.3-0 Ma
Conus sp.		x	x	113-0 Ma
Anadara sp.			x	140-0 Ma
Anadara grandis			x	11.6-0 Ma
Ostrea sp.		x	x	260-0 Ma
Ostrea angelica			x	5.3-0 Ma
Chama sp.			x	130-0 Ma
Nerita scabricosta			x	-
Triplofusus princeps			x	5.3-0 Ma
Codakia distinguenda			x	5.3-0 Ma

Leopecten sp.		x		33-0 Ma
Leopecten bakeri bakeri		x		5.3-3.6 Ma
Euvola sp.		x		48-0 Ma
Trachycardium sp.			x	109-0 Ma
Malea sp.			x	20-0 Ma
Age Overlap	5.3-3.6 Ma	5.3-3.6 Ma	3.6-0 Ma	

References

Allmendinger, R. (2018). Software FaultKin 8. Retrieved from http://www.geo.cornell.edu/geology/faculty/RWA/programs/faultkin.html

Anderson, Charles A. 1950. “1940 E. W. SCRIPPS CRUISE TO THE GULF OF CALIFORNIA: Part I. Geology of Islands and Neighboring Land Areas.” P. 0 in *1940 E. W. Scripps Cruise to the Gulf of California*. Vol. 43, edited by C. A. Anderson, J. W. Durham, F. P. Shepard, M. L. Natland, and R. Revelle. Geological Society of America.

Anderson, Densmore, and Ellis. 1999. “The Generation and Degradation of Marine Terraces.” *Basin Research* 11(1):7–19. doi: 10.1046/j.1365-2117.1999.00085.x.

Anderson, Ernest. 1951. *The Dynamics of Faulting and Dyke Formation with Applications to Britain*. 2nd ed. Oliver and Boyd.

Avellán, Denis Ramón, José Luis Macías, José Luis Arce, Ricardo Saucedo-Girón, Víctor Hugo Garduño-Monroy, Adrian Jiménez-Haro, Giovanni Sosa-Ceballos, Guillermo Cisneros, Juan Pablo Bernal, Paul W. Layer, Laura García-Sánchez, Gabriela Reyes-Agustín, Elizabeth Rangel, José Antonio Navarrete, and Héctor López-Loera. 2019. “Geology of the Late Pleistocene Tres Vírgenes Volcanic Complex, Baja California Sur (México).” *Journal of Maps* 15(2):227–37. doi: 10.1080/17445647.2019.1576552.

Axen, Gary J. 1988. “The Geometry of Planar Domino-Style Normal Faults above a Dipping Basal Detachment.” *Journal of Structural Geology* 10(4):405–11. doi: 10.1016/0191-8141(88)90018-1.

Axen, Gary J., and John M. Fletcher. 1998. “Late Miocene-Pleistocene Extensional Faulting, Northern Gulf of California, Mexico and Salton Trough, California.” *International Geology Review* 40(3):217–44. doi: 10.1080/00206819809465207.

Axen, Gary J., and John M. Hartley. 1997. “Field Tests of Rolling Hinges: Existence, Mechanical Types, and Implications for Extensional Tectonics.” *Journal of Geophysical Research: Solid Earth* 102(B9):20515–37. doi: 10.1029/97JB01355.

Balestrieri, Maria Laura, Luca Ferrari, Marco Bonini, Jose Duque-Trujillo, Mariano Cerca, Giovanna Moratti, and Giacomo Corti. 2017. “Apatite Fission Dating from Intrusive Rock Sample BEKL4D1.” *In Supplement to: Balestrieri, ML et al. (2017): Onshore and Offshore Apatite Fission-Track Dating from the Southern Gulf of California: Insights into the Time-Space Evolution of the Rifting. Tectonophysics, 719-720, 148-161, Https://Doi.Org/10.1016/j.Tecto.2017.05.012*.

Bartley, John M., John M. Fletcher, and Allen F. Glazner. 1990. “Tertiary Extension and Contraction of Lower-plate Rocks in the Central Mojave Metamorphic Core Complex, Southern California.” *Tectonics* 9(3):521–34. doi: 10.1029/TC009i003p00521.

Batiza, R. 1978. “Geology, Petrology, and Geochemistry of Isla Tortuga, a Recently Formed Tholeiitic Island in the Gulf of California.” *Geological Society of America Bulletin* 89(9):1309. doi: 10.1130/0016-7606(1978)89<1309:GPAGOI>2.0.CO;2.

Batiza, Rodey, Kiyoto Futa, and Carl E. Hedge. 1979. “TRACE ELEMENT AND STRONTIUM ISOTOPE CHARACTERISTICS OF VOLCANIC ROCKS FROM ISLA TORTUGA: A YOUNG SEAMOUNT IN THE GULF OF CALIFORNIA.”

Bennett, Scott E. K., and Michael E. Oskin. 2014. “Oblique Rifting Ruptures Continents: Example from the Gulf of California Shear Zone.” *Geology* 42(3):215–18. doi: 10.1130/G34904.1.

Boggs, Sam. 2006. *Principles of Sedimentology and Stratigraphy*. 4. ed. Upper Saddle River, NJ: Pearson Prentice Hall.

Bot, Anna, Laurent Geoffroy, Christine Authemayou, Hervé Bellon, David Graindorge, and Raphaël Pik. 2016. “Miocene Detachment Faulting Predating EPR Propagation: Southern Baja California.” *Tectonics* 35(5):1153–76. doi: 10.1002/2015TC004030.

Brothers, Daniel, Alistair Harding, Antonio González-Fernández, W. Steven Holbrook, Graham Kent, Neal Driscoll, John Fletcher, Dan Lizarralde, Paul Umhoefer, and Gary Axen. 2012. “Farallon Slab Detachment and Deformation of the Magdalena Shelf, Southern Baja California.” *Geophysical Research Letters* 39(9). doi: 10.1029/2011GL050828.

Bryan, S. E., T. Orozco-Esquivel, L. Ferrari, and M. López-Martínez. 2014. “Pulling Apart the Mid to Late Cenozoic Magmatic Record of the Gulf of California: Is There a Comondú Arc?” *Geological Society, London, Special Publications* 385(1):389–407. doi: 10.1144/SP385.8.

Buck, W. Roger. 1988. “FLEXURAL ROTATION OF NORMAL FAULTS.”

Busby, Cathy, Alison Graettinger, Margarita López Martínez, Sarah Medynski, Tina Niemi, Claire Andrews, Emilie Bowman, Evelyn P. Gutierrez, Matthew Henry, Emma Lodes, Judith Ojeda, Jonathan Rice, Graham Andrews, and Sarah Brown. 2020. “Volcanic Record of the Arc-to-Rift Transition Onshore of the Guaymas Basin in the Santa Rosalía Area, Gulf of California, Baja California.” *Geosphere* 16(4):1012–41. doi: 10.1130/GES02094.1.

Calmus, Thierry, Carlos Pallares, René C. Maury, Alfredo Aguillón-Robles, Hervé Bellon, Mathieu Benoit, and François Michaud. 2011. “Volcanic Markers of the Post-Subduction Evolution of Baja California and Sonora, Mexico: Slab Tearing Versus Lithospheric Rupture of the Gulf of California.” *Pure and Applied Geophysics* 168(8–9):1303–30. doi: 10.1007/s00024-010-0204-z.

Carreño, Analuisa L., J. Ledesma-Vazquez, C. F. Hernandez-Perez, and F. R. Gio-Argaez. 2015. “Microfossils from the Early Pliocene Carmen Formation, Monserrat Island, Baja California Sur, Mexico.” *Micropaleontology* 61(3):199–225. doi: 10.47894/mpal.61.3.07.

Dietz, Robert S. 1963. “Wave-Base, Marine Profile of Equilibrium, and Wave-Built Terraces: A Critical Appraisal.” *GSA Bulletin* 74(8):971–90. doi: 10.1130/0016-7606(1963)74[971:WMPOEA]2.0.CO;2.

Dorsey, Rebecca J., Paul J. Umhoefer, James C. Ingle, and Larry Mayer. 2001. “Late Miocene to Pliocene Stratigraphic Evolution of Northeast Carmen Island, Gulf of California: Implications for Oblique-Rifting Tectonics.” *Sedimentary Geology* 144(1–2):97–123. doi: 10.1016/S0037-0738(01)00137-3.

Drake, William R., Paul J. Umhoefer, Alexis Griffiths, Ann Vlad, Lisa Peters, and William McIntosh. 2017. “Tectono-Stratigraphic Evolution of the Comondú Group from Bahía de La Paz to Loreto, Baja California Sur, Mexico.” *Tectonophysics* 719–720:107–34. doi: 10.1016/j.tecto.2017.04.020.

Dunham, Robert J. 1962. “Classification of Carbonate Rocks According to Depositional Texture1.” P. 0 in *Classification of Carbonate Rocks—A Symposium*. Vol. 1, edited by W. E. Ham. American Association of Petroleum Geologists.

Duque-Trujillo, Jose, Luca Ferrari, Teresa Orozco-Esquivel, Margarita López-Martínez, Peter Lonsdale, Scott E. Bryan, Jared Kluesner, Doris Piñero-Lajas, and Luigi Solari. 2015. “Timing of Rifting in the Southern Gulf of California and Its Conjugate Margins: Insights from the Plutonic Record.” *Geological Society of America Bulletin* 127(5–6):702–36. doi: 10.1130/B31008.1.

Durham, J. Wyatt. 1950. “1940 E. W. SCRIPPS CRUISE TO THE GULF OF CALIFORNIA: Part II Megascopic Paleontology and Marine Stratigraphy.” P. 0 in *1940 E. W. Scripps Cruise to the Gulf of California*. Vol. 43, edited by C. A. Anderson, J. W. Durham, F. P. Shepard, M. L. Natland, and R. Revelle. Geological Society of America.

Ferrari, Luca, Margarita López-Martínez, Gerardo Aguirre-Díaz, and Gerardo Carrasco-Núñez. 1999. “Space-Time Patterns of Cenozoic Arc Volcanism in Central Mexico: From the Sierra Madre Occidental to the Mexican Volcanic Belt.” *Geology* 27(4):303. doi: 10.1130/0091-7613(1999)027<0303:STPOCA>2.3.CO;2.

Ferrari, Luca, Margarita López-Martínez, Teresa Orozco-Esquivel, Scott E. Bryan, Jose Duque-Trujillo, Peter Lonsdale, and Luigi Solari. 2013. “Late Oligocene to Middle Miocene Rifting and Synextensional Magmatism in the Southwestern Sierra Madre Occidental, Mexico: The Beginning of the Gulf of California Rift.”

Ferrari, Luca, Teresa Orozco-Esquivel, Scott E. Bryan, Margarita López-Martínez, and Argelia Silva-Fragoso. 2018. “Cenozoic Magmatism and Extension in Western Mexico: Linking the Sierra Madre Occidental Silicic Large Igneous Province and the Comondú Group with the Gulf of California Rift.” *Earth-Science Reviews* 183:115–52. doi: 10.1016/j.earscirev.2017.04.006.

Ferrari, Luca, Teresa Orozco-Esquivel, Vlad Manea, and Marina Manea. 2012. “The Dynamic History of the Trans-Mexican Volcanic Belt and the Mexico Subduction Zone.” *Tectonophysics* 522–523:122–49. doi: 10.1016/j.tecto.2011.09.018.

Ferrari, Luca, Joann M. Stock, and Jaime Urrutia Fucugauchi. 2000. “Introduction to Special Issue: ‘The Influence of Plate Interaction on Post-Laramide Magmatism and Tectonics in Mexico.’” *Tectonophysics* 318(1–4):vii–ix. doi: 10.1016/S0040-1951(99)00303-0.

Fletcher, J. M., M. Grove, D. Kimbrough, O. Lovera, and G. E. Gehrels. 2007. “Ridge-Trench Interactions and the Neogene Tectonic Evolution of the Magdalena Shelf and Southern Gulf of California: Insights from Detrital Zircon U-Pb Ages from the Magdalena Fan and Adjacent Areas.” *Geological Society of America Bulletin* 119(11–12):1313–36. doi: 10.1130/B26067.1.

Fletcher, John M., and Luis Munguía. 2000. “Active Continental Rifting in Southern Baja California, Mexico: Implications for Plate Motion Partitioning and the Transition to Seafloor Spreading in the Gulf of California.” *Tectonics* 19(6):1107–23. doi: 10.1029/1999TC001131.

Gidde, Andreas. 1992. “Sedimentology of the Miocene Cerro Colorado Member (Upper Part of the El Cien Formation), Baja California Sur, Mexico.” *Zentralblatt Für Geologie Und Paläontologie. Teil 1, Allgemeine, Angewandte, Regionale Und Historische Geologie* 1991(6):1467–77.

Graettinger, A. H., C. J. Busby, M. López-Martínez, T. Orozco-Esquivel, K. Putirka, N. Acuña Henry, J. Allard, S. J. Hutchinson, and T. Niemi. in press. “EARLY MIOCENE TO PLIOCENE MAGMATIC AND STRUCTURAL EVOLUTION OF THE GULF OF CALIFORNIA MARGIN IN CENTRAL BAJA CALIFORNIA (MEXICO): The Mulegé-La Trinidad Region, Baja California Sur.”

Guerrero, Fernando J., Giovanni Sosa-Ceballos, Rosa M. Prol-Ledesma, Mariana P. Jácome-Paz, Marco Calò, Luis Miguel De La Cruz, and José Luis Macías. 2021. “A Numerical Model for the Magmatic Heat Reservoir of the Las Tres Virgenes Volcanic Complex, Baja California Sur, Mexico.” *Journal of Volcanology and Geothermal Research* 414:107227. doi: 10.1016/j.jvolgeores.2021.107227.

Hausback, B. 1984. “CENOZOIC VOLCANIC AND TECTONIC EVOLUTION OF BAJA CALIFORNIA SUR, MEXICO.”

Helenes, J., A. L. Carreño, and R. M. Carrillo. 2009. “Middle to Late Miocene Chronostratigraphy and Development of the Northern Gulf of California.” *Marine Micropaleontology* 72(1):10–25. doi: 10.1016/j.marmicro.2009.02.003.

Johnson, Markes E. 2014. “Song of the Amazon on Isla Monserrat.” in *Off-Trail Adventures in Baja California: Exploring Landscapes and Geology on Gulf Shores and Islands*. University of Arizona Press.

Keller, Edward A., and Nicholas Pinter. 2002. *Active Tectonics: Earthquakes, Uplift, and Landscape*. Prentice Hall.

Kelsey, Harvey M. 2015. "Geomorphological Indicators of Past Sea Levels." Pp. 66–82 in *Handbook of Sea-Level Research*, edited by I. Shennan, A. J. Long, and B. P. Horton. Wiley.

LaForge, Justin S., Barbara E. John, and Craig B. Grimes. 2017. "Synextensional Dike Emplacement across the Footwall of a Continental Core Complex, Chemehuevi Mountains, Southeastern California." *Geosphere* 13(6):1867–86. doi: 10.1130/GES01402.1.

Lehner, Benedikt L. 1991. "Neptunian Dykes along a Drowned Carbonate Platform Margin: An Indication for Recurrent Extensional Tectonic Activity?" *Terra Nova* 3(6):593–602. doi: 10.1111/j.1365-3121.1991.tb00201.x.

Lonsdale, Peter. 1989. "Geology and Tectonic History of the Gulf of California." P. 0 in *The Eastern Pacific Ocean and Hawaii*. Vol. N, edited by E. L. Winterer, D. M. Hussong, and R. W. Decker. Geological Society of America.

Lonsdale, Peter. 1991. "Structural Patterns of the Pacific Floor Offshore of Peninsular California." P. 0 in *The Gulf and Peninsular Province of the Californias*. Vol. 47, edited by J. P. Dauphin and B. R. T. Simoneit. American Association of Petroleum Geologists.

Mammerickx, Jacqueline, and Kim D. Klitgord. 1982. "Northern East Pacific Rise: Evolution from 25 m.y. B.P. to the Present." *Journal of Geophysical Research: Solid Earth* 87(B8):6751–59. doi: 10.1029/JB087iB08p06751.

Martínez, Miranda, and Adriana Yanet. 2019. "Edad de Los Depósitos Marinos Asociados a La Evolución Temprana Del Golfo de California."

McDougall, K. M. 2009."Update on Microfossil Studies in the Northern Gulf of California and the Salton Trough."

McLean, Hugh, B. P. Hausback, and J. H. Knapp. 1986. *The Geology of West-Central Baja California Sur, Mexico*. 1579. U.S. Geological Survey ; For sale by the Distribution Branch, Text Products Section,. doi: 10.3133/b1579.

Mizera, M., T. A. Little, J. Biemiller, S. Ellis, S. Webber, and K. P. Norton. 2019. "Structural and Geomorphic Evidence for Rolling-Hinge Style Deformation of an Active Continental Low-Angle Normal Fault, SE Papua New Guinea." *Tectonics* 38(5):1556–83. doi: 10.1029/2018TC005167.

Mylroie, Joan R., and John E. Mylroie. 2007. "Development of the carbonate island karst model." 69.

Ocampo-Díaz*, Yam Zul Ernesto, Sonia Alejandra Torres-Sánchez, Carita Augustsson, José Luis Macías, Giovanni Sosa-Ceballos, Guillermo Cisneros-Máximo, Laura García-Sánchez,

Susana Osorio-Ocampo, Denis-Ramón Avellán, Jenny Omma, Carlos Ortega-Obregón, Luigi A. Solari, and Gerardo González-Barba. 2021. “Provenance of the El Salto Formation (Early Oligocene to Early Miocene), Southern Part of La Reforma Caldera, Baja California Sur, Mexico.” Pp. 277–308 in *Southern and Central Mexico: Basement Framework, Tectonic Evolution, and Provenance of Mesozoic–Cenozoic Basins*, edited by U. C. Martens and R. S. M. Garza. Geological Society of America.

Oretsky, Zachary Lewis. 2020. “Uplifted Marine Terraces in the Bahía de Loreto Region, Baja California Sur, Mexico; Preliminary Testing of GPS Vertical Velocities and Hydro-Isostatic Loading.”

Oskin, Michael, and Joann Stock. n.d. “Marine Incursion Synchronous with Plate-Boundary Localization in the Gulf of California.” *Geology 2003* 31(1):23–26. doi: https://doi.org/10.1130/0091-7613(2003)031<0023:MISWPB>2.0.CO;2.

Oskin, Michael, Joann Stock, and Arturo Martín-Barajas. 2001. “Rapid Localization of Pacific–North America Plate Motion in the Gulf of California.” *Geology* 29(5):459–62. doi: 10.1130/0091-7613(2001)029<0459:RLOPNA>2.0.CO;2.

Osorio-Ocampo, Susana, Laura García-Sánchez, Reyna Marcela Lira-Beltrán, José Luis Macías*, Antonio Pola, Denis Ramón Avellán, Yam Zul Ernesto Ocampo-Díaz, Gianluca Groppelli, Roberto Sulpizio, Felipe García-Tenorio, Gerardo González-Barba, and Giovanni Sosa-Ceballos. 2019. “Volcanic and Marine Stratigraphy along the El Álamo Canyon, Santa Rosalía Basin, Baja California Sur.” Pp. 187–208 in *Geologic Excursions in Southwestern North America*, edited by P. A. Pearthree. Geological Society of America.

Panchuk, Karla. 2019. “7.3 Classification of Igneous Rocks.”

Paz Moreno, Francisco A., and Alain Demant. 1999. “The Recent Isla San Luis Volcanic Centre: Petrology of a Rift-Related Volcanic Suite in the Northern Gulf of California, Mexico.” *Journal of Volcanology and Geothermal Research* 93(1–2):31–52. doi: 10.1016/S0377-0273(99)00083-9.

Rossi, Matthew W., Mark C. Quigley, John M. Fletcher, Kelin X. Whipple, J. Jesús Díaz-Torres, Christian Seiler, L. Keith Fifield, and Arjun M. Heimsath. 2017. “Along-Strike Variation in Catchment Morphology and Cosmogenic Denudation Rates Reveal the Pattern and History of Footwall Uplift, Main Gulf Escarpment, Baja California.” *GSA Bulletin* 129(7–8):837–54. doi: 10.1130/B31373.1.

Sawlan, M., and James G. Smith. 1984. “Petrologic Characteristics, Age and Tectonic Setting of Neogene Volcanic Rocks in Northern Baja California Sur, Mexico.”

Sawlan, Michael. 1991. “Magmatic Evolution of the Gulf of California Rift.” Pp. 301–69 in *The Gulf and Peninsular Province of the Californias*.

Scott, Andrew T., and Nicholas Pinter. 2003. “Extraction of Coastal Terraces and Shoreline-Angle Elevations from Digital Terrain Models, Santa Cruz and Anacapa Islands, California.” *Physical Geography*.

Shackleton, N. J. 1987. “Oxygen Isotopes, Ice Volume and Sea Level.” *Quaternary Science Reviews* 6(3–4):183–90. doi: 10.1016/0277-3791(87)90003-5.

Smart, Peter L., R. J. Palmer, F. Whitaker, and V. Paul Wright. 1988. “Neptunian Dikes and Fissure Fills: An Overview And.” Pp. 149–62 in *Paleokarst*, edited by N. P. James and P. W. Choquette. New York, NY: Springer.

Sosa-Ceballos, G., J. L. Macías, D. R. Avellán, J. L. Arce, R. Saucedo, M. Boijseauneau-López, L. García-Sánchez, G. Reyes-Agustín, and S. Osorio-Ocampo. 2019. “Genesis of Magmas from the Tres Vírgenes Volcanic Complex, Baja California Sur, Mexico.” *Lithos* 350–351:105240. doi: 10.1016/j.lithos.2019.105240.

Spencer, Jon E. 1984. “Role of Tectonic Denudation in Warping and Uplift of Low-Angle Normal Faults.” *Geology* 12(2):95–98. doi: 10.1130/0091-7613(1984)12<95:ROTDIW>2.0.CO;2.

Stock, J. M., and K. V. Hodges. 1989. “Pre-Pliocene Extension around the Gulf of California and the Transfer of Baja California to the Pacific Plate.” *Tectonics* 8(1):99–115. doi: 10.1029/TC008i001p00099.

Sutherland, Fiona H., Graham M. Kent, Alistair J. Harding, Paul J. Umhoefer, Neal W. Driscoll, Daniel Lizarralde, John M. Fletcher, Gary J. Axen, W. Steven Holbrook, Antonio González-Fernández, and Peter Lonsdale. 2012. “Middle Miocene to Early Pliocene Oblique Extension in the Southern Gulf of California.” *Geosphere* 8(4):752–70. doi: 10.1130/GES00770.1.

Umhoefer, Paul J. 2011. “Why Did the Southern Gulf of California Rupture so Rapidly?—Oblique Divergence across Hot, Weak Lithosphere along a Tectonically Active Margin.” *GSA Today* 4–10. doi: 10.1130/G133A.1.

Umhoefer, Paul J., Rebecca J. Dorsey, Shawn Willsey, Larry Mayer, and Paul Renne. 2001. “Stratigraphy and Geochronology of the Comondú Group near Loreto, Baja California Sur, Mexico.” *Sedimentary Geology* 144(1–2):125–47. doi: 10.1016/S0037-0738(01)00138-5.

Umhoefer, Paul J., Larry Mayer, and Rebecca J. Dorsey. 2002. “Evolution of the Margin of the Gulf of California near Loreto, Baja California Peninsula, Mexico.” *Geological Society of America Bulletin* 114(7):849–68. doi: 10.1130/0016-7606(2002)114<0849:EOTMOT>2.0.CO;2.

Várkonyiv, Péter, and Henrik Hargitai. 2021. “Scour Marks.” Pp. 1–5 in *Encyclopedia of Planetary Landforms*, edited by H. Hargitai and Á. Kereszturi. New York, NY: Springer.

Vázquez, J. Ledesma, A. Y. Montiel Boehringer, D. Backus, M. Johnson, and V. Z. Fernández Diaz. 2007. “ARMORED MUD BALLS IN TIDAL ENVIRONMENTS, PLIOCENE IN THE GULF OF CALIFORNIA.” Pp. 235–38 in *4th European Meeting on the Palaeontology and Stratigraphy of Latin America*. Instituto Geológico y Minero de España.

Wernicke, Brian, and Gary J. Axen. 1988. “On the Role of Isostasy in the Evolution of Normal Fault Systems.” *Geology* 16(9):848. doi: 10.1130/0091-7613(1988)016<0848:OTROII>2.3.CO;2.

Wilson, C. J. N., and Wes Hildreth. 1997. “The Bishop Tuff: New Insights From Eruptive Stratigraphy.” *The Journal of Geology* 105(4):407–40. doi: 10.1086/515937.

Appendix I.

Report on Microfossils from Monserrate Island, Baja California Sur, Mexico

Kristin McDougall

Ten samples submitted from Monserrate Island in the Gulf of California, Mexico, were analyzed to determine the age and environment. Samples Mf14704, 14706 and 14707 were taken in the vicinity of the Carmen Formation section studied by Carreño et al. (2015) whereas the other samples were taken from exposures on the interior of the island (fig. 1). All new samples were questionable thought to be Carmen Formation.

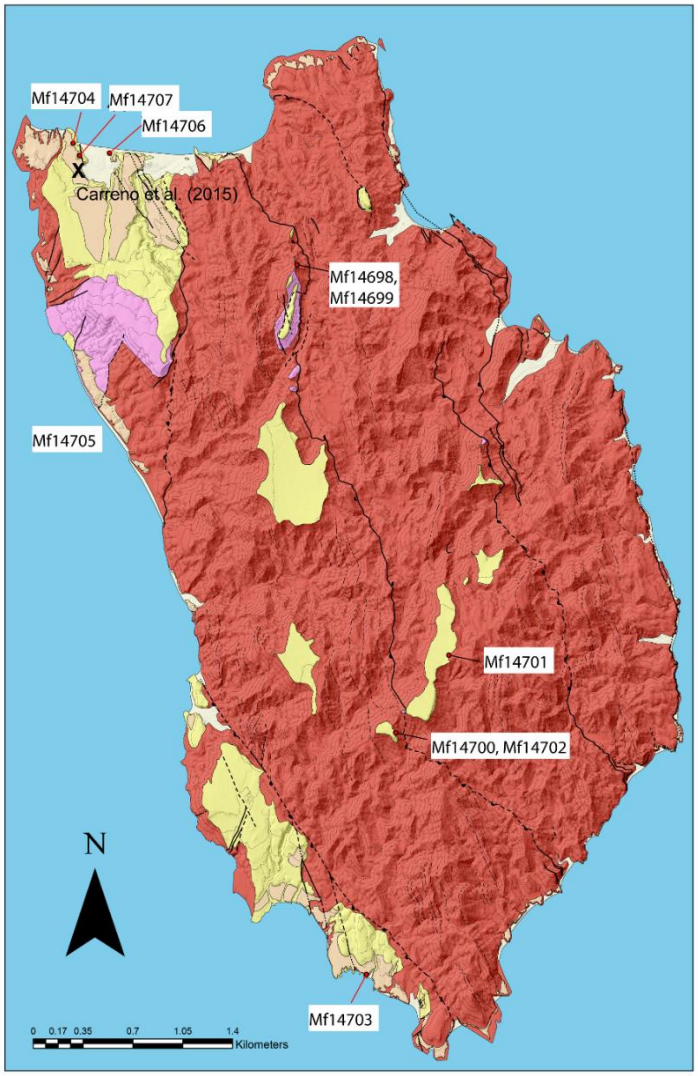

Figure 1. Location map of Monserrate Island, Baja California Sur. Localities from Carreño et al. (2015) are near Mf14704, Mf1706, and Mf14707, at the north end of the island.

Samples collected from exposures in the interior and along the west and south coast, contain microfossils; however, the preservation of most specimens is poor due to the calcium overgrowths and/or destruction of the tests. Microfossil composition of the samples is given in Table 1. Analysis of the assemblages considers the age, ecology and comparison to the section discussed by Carreño et al. (2015).

USGS Lab. Numbers	Mf14698	Mf14699	Mf14700	Mf14701	Mf14702	Mf14703	Mf14705	Mf14704	Mf14706	Mf14707
Field numbers (ISMON Sept)	D5 S3	D5 S4	D8 JPN PL F1	D8 S2	D8 JPN PL F2	D12 S1	D16 S2	D13 S1	D18 S3	D18 S4
*Amphistegina gibbosa	89.47	68.29	65.95	83.33	82.35	32.26	1.89	18.30	-	0.21
*Bolivina argentea	-	-	-	-	-	-	-	0.43	0.43	-
*Bolivina interjuncata	-	-	-	-	-	-	3.77	7.66	18.48	27.78
Bolivina piersonae	-	-	-	-	-	-	-	-	0.65	-
*Bolivina seminuda	-	-	-	-	-	-	1.89	-	-	-
*Bolivina subadvena	-	-	-	-	-	-	1.89	8.51	32.39	27.78
Buccella frigida	-	-	0.24	-	-	-	-	-	-	-
Buccella parkerae	-	-	0.24	-	-	-	-	-	-	-
*Bulimina denudata	-	-	0.48	-	-	-	-	-	0.65	-
*Buliminella curta	-	-	-	-	-	-	-	1.06	5.65	5.56
*Cancris auricula	-	-	0.12	-	-	-	-	-	0.43	-
*Cancris carmenensis	-	-	0.12	-	-	-	-	-	-	-
Cancris spp.	-	-	0.24	-	-	-	-	-	-	-
*Cassidulina limbata	-	-	0.36	-	-	-	-	-	-	-
Cibicides fletcheri	-	1.63	5.28	-	-	-	1.89	4.26	-	-
*Cibicides gallowayi	3.76	-	-	-	-	-	-	-	-	-
Cibicides spp.	-	0.81	-	-	2.94	-	-	-	-	-
*Cibicidoides mckannai	2.26	5.69	10.07	-	5.88	1.61	24.53	15.74	-	0.21
Discorbis spp.	-	-	-	-	-	-	-	0.21	-	-
*Dyocibicides perferata	-	-	0.12	-	-	2.42	-	-	0.22	-
*Elphidium articulatum	-	-	-	-	-	-	7.55	-	-	-
*Elphidium crispum	-	1.63	0.84	-	-	4.84	1.89	7.02	-	-
Epistominella smithi	-	-	-	-	-	-	-	1.49	6.09	4.70
Eponides repandus	2.26	16.26	1.44	-	-	-	18.87	0.64	-	-
*Euloxostomum pseudobeyrichi	-	-	-	-	-	-	-	-	1.09	-
*Fursenkoina bramletti	-	-	-	-	-	-	-	0.21	0.87	-
*Galliherina uvigerinaformis	-	-	-	-	-	-	-	-	-	7.69
*Globobulimina ovula	-	-	-	-	-	-	-	-	3.91	-

*Gyroidina rothwelli	-	-	-	-	-	-	-	5.11	1.96	5.34
*Gyroidina soldanii	-	-	-	-	-	-	-	-	0.65	0.21
Gyroidina spp.	-	0.81	-	-	-	-	-	-	-	-
*Hanzawaia nitidula	-	-	1.08	-	-	0.81	-	1.06	0.43	0.43
*Islandella californica	-	-	-	-	-	-	-	0.85	1.74	0.43
Lagena hexagona	-	-	-	-	-	-	-	-	0.22	-
Melonis affinis	-	-	-	-	-	-	-	-	0.22	-
Neoconorbina tequemi	-	-	0.36	-	-	-	-	-	-	-
*Eubuliminella basispinata	-	-	-	-	-	-	-	-	0.22	-
Peneropolis pertusus	-	-	-	-	-	11.29	3.77	-	-	-
*Planulina ornata	-	-	1.44	-	-	9.68	-	-	-	0.43
*Pullenia bulloides	-	-	-	-	-	0.81	-	-	-	-
Quinqueloculina akneriana	0.75	-	-	-	2.94	25.00	15.09	18.51	-	-
Quinqueloculina lamarkina	-	-	-	-	-	4.03	3.77	0.85	-	-
Rectobolivina hancocki	-	-	0.12	-	-	-	-	-	-	-
Reusella pacifica	-	-	-	-	-	-	-	-	-	0.21
Rotalia spp.	-	-	0.24	-	-	-	-	-	-	-
*Rotorbinella companulata	-	0.81	2.64	-	-	0.81	5.66	0.85	-	-
*Takayanagia delicata	-	-	-	-	-	-	-	0.21	3.26	3.63
Tidwellella exorna	-	-	4.08	-	-	-	-	-	-	-
*Trifarina carinata	-	-	-	-	-	-	-	0.21	1.30	0.85
*Trifarina occidentalis	-	-	-	-	-	-	-	-	0.43	-
Triloculina spp.	0.75	-	-	-	-	-	-	-	-	-
Uvigerina peregrina	-	-	-	-	-	-	-	2.13	1.52	0.21
*Valvulineria inflata	0.75	-	0.12	16.67	-	-	-	2.98	9.57	4.27
unidentified forms	-	4.07	1.32	-	5.88	-	5.66	1.49	0.22	-
Planktic Foraminifers	-	-	3.12	-	-	6.45	1.89	0.21	7.39	10.04
Foraminiferal number	133	123	834	6	34	124	53	470	460	468
Diversity	7	9	23	2	5	12	15	24	26	18

Table 1. Distribution and abundance of foraminifers from samples collected on Monserrate Island, Baja California Sur. Abundances indicate the percentage of the total foraminiferal fauna or absent (-). Diversity is the number of species identified in the sample. An asterisk (*) indicates species was found in the section examined by Carreño et al. (2015).

Discussion of age, environment, and comparison to Carmen Formation

Few benthic foraminifers are found in samples Mf14698 and Mf14699, from the carbonate top of the Plateau 2A. Preservation is poor due to calcium overgrowths and broken specimens. The assemblages are not diagnostic of age but are commonly found in Late Miocene to Pliocene.

The foraminiferal assemblages are moderately diverse with 7-9 species present, although they are dominated by *Amphistegina gibbosa*, which comprises 90% of the assemblage. This species is "normally most abundant in (but not restricted to) tropical and warm subtropical reef, near-reef, and bank biotopes having high $CaCO_3$ content, euhaline to hyperhaline waters, mean winter temperatures no less than 14°C, mean summer temperatures no less than 25°C, and depths not much greater than 100 m. It lives primarily as an epibiont on sea grasses and hard substrates, but it also can live in or on soft sediments." (Crouch and Poag, 1979, p. 92). Other species present are rare (usually <5% of the assemblage) and include *Cibicides fletcheri*, *C. gallowayi*, *C. mckannai*, Elphidium crispum, *Eponides repandus*, *Rotorbinella companulata*, *Quinqueloculina akneriana*, and *Triloculina* spp. All of these species are epifauna and commonly found associated with hard substrates. These species are also present in the lower part of Carmen Formation of Carreño et al. (2015) except *E. repandus*, *Q. ackneriana*, and *Triloculina* spp.

Samples Mf14700 through Mf14702 are from the carbonate plateau in the southeast center of the island, directly south of Plateau 6. The sediments are well indurated. Benthic foraminifers are abundant in sample Mf14700 but sparse in Mf14701-14702 due to preservation. A few (26) planktic foraminifers are observed in sample Mf14700 but preservation is poor. Age diagnostic species are not present and only a general Late Miocene to Pliocene age is suggested. Sample Mf14700 contains 23 species and although still dominated by *Amphistegina gibbosa,* the foraminiferal assemblage contains more species with upper depth limits in the outer neritic and upper bathyal biofacies. Many of the *Amphistegina gibbosa* specimens appear to be transported along with other inner neritic specimens. Species which have their upper depth limits (UDLs) in the outer neritic biofacies but become more abundant in deeper water include *Hanzawaia nitidula, Planulina ornata*, and *Tidwellella exorna. Cibicidoides mckannai* dominates the species with UDLs in the upper bathyal biofacies. Samples Mf14701 and Mf14702 also contain abundant *A. gibbosa* as well as rare inner neritic species and a few upper bathyal species. These assemblages suggest deposition occurred at outer neritic depths (50-150 m) and probably close to the shelf edge based on the presence of rare to few species with UDLs in the upper bathyal biofacies. The low number of planktic foraminifers also suggest deposition in the outer neritic biofacies near the shelf edge.

Again, most of the species are also noted in the Carmen Formation examined by Carreño et al. (2015) but the rare presence of *Cassidulina limbata*, and the common occurrence of *Valvulineria inflata* (Mf14701) in association with the outer neritic and upper bathyal species suggest these samples are most likely coeval with the lower samples (~IM-3) examined by Carreño et la (2015).

Sample Mf14703 was taken from loose sediment cover of terrace 1 (MIS 5e terrace) of south-southwest coast sandstone. The foraminiferal assemblage is similar to the previous group; *A. gibbosa* dominates but is also associated with species that have UDls in the outer neritic biofacies. The upper bathyal species are reduced in this assemblage compared to the previous group. Rare (8) planktic foraminifers are present. Deposition of this sample occurred in the outer neritic biofacies (50-150 m) near the shelf edge.

Sample Mf14705 was taken from terrace level 1 on west coast (MIS 5e terrace surface). Although *A. gibbosa* dominates it more reduced than in previous assemblages and the abundance of upper bathyal species is increased. Few *Bolivina seminuda* and *B. subadvena* appear. These are infaunal species and common in the oxygen minimum zone. Because they are rare in this assemblage, deposition probably occurred above the oxygen minimum zone (OMZ) but in the upper bathyal biofacies (150-500 m). Downslope transport of shelf material is common in this sample. This assemblage is similar to assemblages found in the lower part of the Carreño et al. (2015) section.

Samples Mf14704, Mf14706, and Mf14707 were taken in the vicinity of the Carreño et al. (2015) section on the north end of the island. The age of these samples is Late Miocene, coeval with planktic zone M13 and restricted to the Mohnian to Delmontian Stages of California (Late Miocene; Kleinpell, 1938) based on the occurrence of *Galliherina uvigerinaformis*. The presence of this species is restricted to the lower part of the Carreño et al. (2015) section (IM-1 through IM-3).

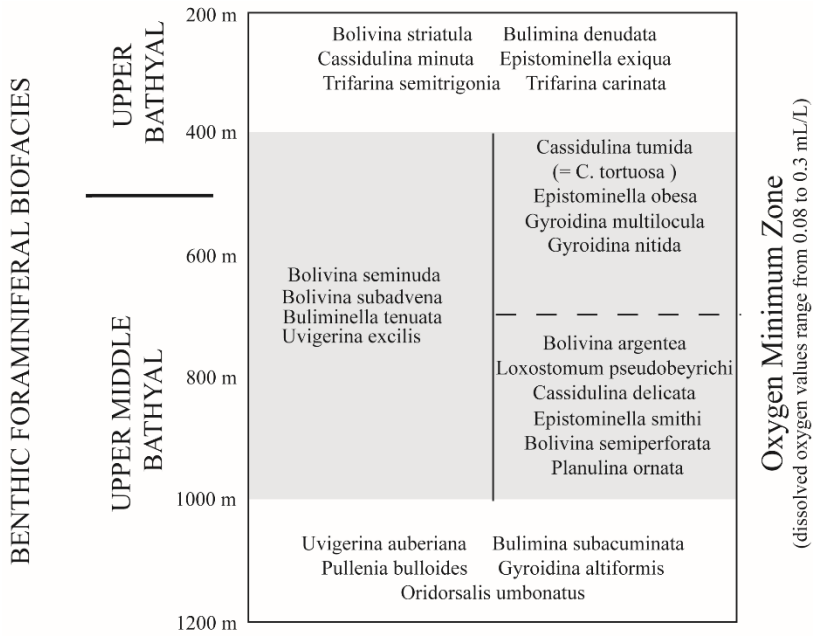

Figure 2. Benthic foraminiferal species characteristic of the oxygen minimum zone off Central America. The OMZ from the Pacific margin off Central America (Smith, 1964), contains a distinct benthic foraminiferal fauna. Distinct group of species are also found to prefer the upper and lower parts of the OMZ.

Foraminiferal assemblages in Mf14704, Mf14706, and Mf14707 indicate deposition occurred at upper bathyal to middle bathyal depths (150-1500 m) within the OMZ (400- 1000 m). The abundance of *Bolivina seminuda, B. subadvena, B. interjunctata*, *Epistominella smithi, Euloxostomum pseudobeyrichi*, *Takayanagia delicata*, and *Planulina ornata* indicates deposition was occurring in the lower part of the OMZ (~700-1000 m; fig. 2). Material from the adjacent shelf is transported downslope to this location.

Conclusions

The new collection of samples is late Miocene in age although few age diagnostic species are present. Samples from the interior plateaus of Monserrate Island were deposited on the shelf where water depths varied from ~50-150 m and on a hard substrate. Samples are coeval with the lower part of the Carmen Formation examined on the northwest corner of the island. Sample Mf14704, 14706, and Mf14707 which were taken from the general vicinity of the Carreño et al (2015) section include faunas that are similar in age (after Miranda-Matinez, 2019) and environment (revised) to those found in the lower part of the Carreño et al. (2015).

The age of the Carreño et al. (2015) was revised by Miranda-Martinez (2019). She interprets the age of the base of the section to be ~5.8 Ma and the top of the section to be ~5.2 Ma based on a $^{87}Sr/^{86}Sr$ ratio of 5.67 Ma (+0.6/-1.52; $^{87}Sr/^{86}Sr$), the presence of *Globorotalia tumida* (FO: 5.72 Ma; Lourens *et al.* 2004) and *Globorotalia crassaformis* (FO: 5.06 Ma; Bylinskaya, 2004) and the last occurrence of *Globigerinoides bulloideus* (LO: 5.6 Ma; Keigwin, 1982) in sample IM-3, *Streptochilus macdougallae* (LO 4.37; Miranda-Martinez et al., 2017) in sample IM-12, and *S.latus* and *S. inglei* (LO 5.2 and 4.37, respectively; Resig, 1989, 1993; Miranda-Martinez et al., 2017) in IM-15 (Fig. 3). The coiling direction change in *Pulleniatina* was placed at ~5.8-5.6 Ma in the Gulf of California (Miranda-Martinez, 2019).

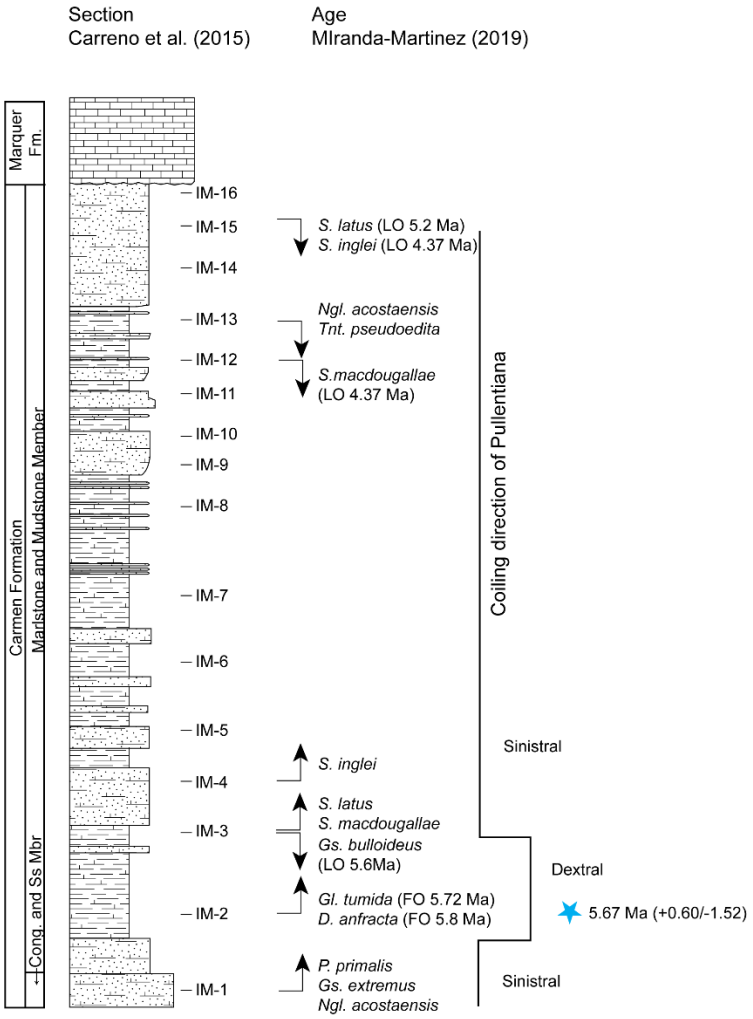

Figure 3. Age of the Carmen Formation on Monserrate Island. Age is Late Miocene based on work by Miranda-Martinez (2019).

Deposition was thought to have occurred under the influence of the oxygen minimum zone at upper bathyal to outer shelf depths, as the result of a tidal mixing mechanism (Carreño et al., 2015). This mechanism was invoked because the northern Gulf of California was interpretated as being deposited in shallow (<200 m) water depths (Helenes et al., 2009). However, subsequent studies have shown that water depths could be greater in the late Miocene (McDougall, 2009). Re-evaluation of the benthic faunas in the Carmen Formation on Monserrate Island indicates deposition occurred at upper middle bathyal depths (500-1500 m) within the lower oxygen minimum zone (~700-1000 m). Water depths shallowed slightly in the upper part of the section.

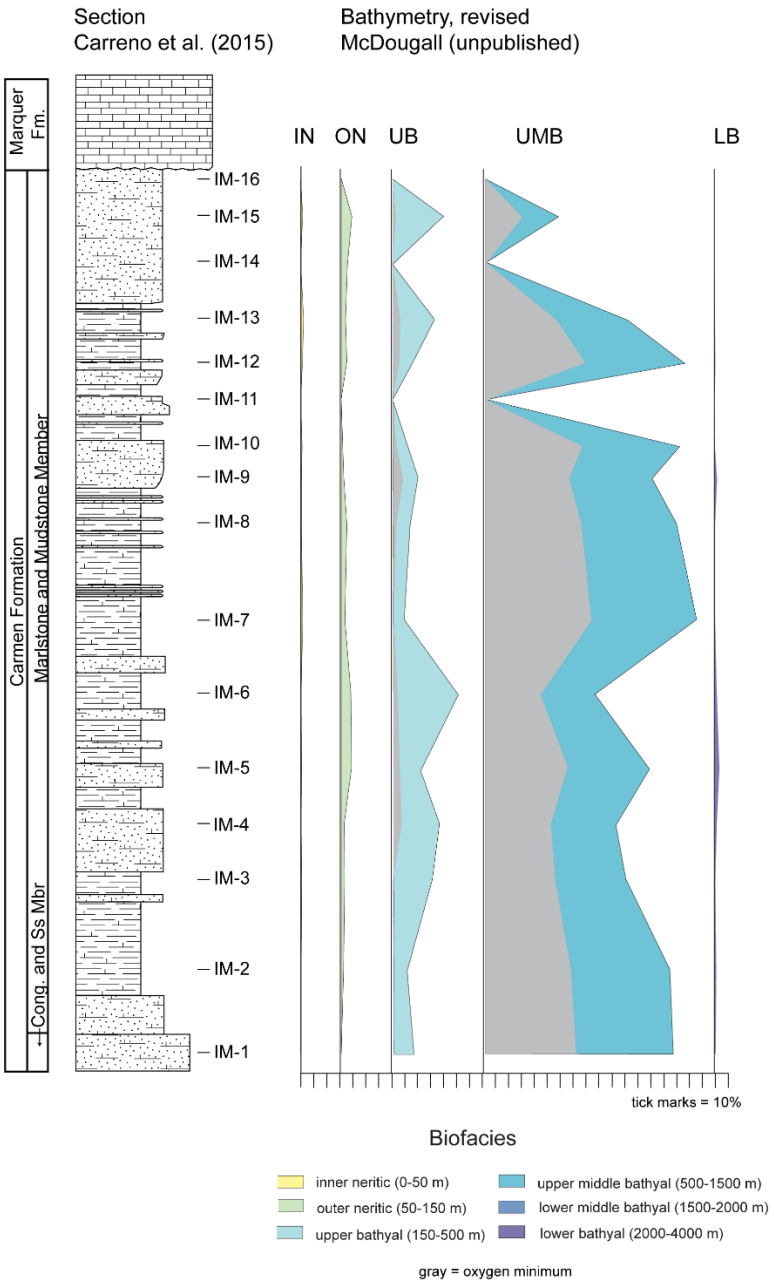

Figure 4 Paleoecologic interpretation of benthic foraminiferal faunas in the Carmen Formation on Monserrate Island. Assemblages indicate deposition occurred at upper middle bathyal depths within the lower part of the OMZ. Modified from Carreño et al. (2015).

References

Bylinskaya, M.E., 2004, Range and stratigraphic significance of the *Globorotalia crassaformis* plexus: Journal of Iberian Geology, v. 31, p. 51-63.

Carreño, A.L., Ledesma-Vaquez, J., Hernandez-Perez, C.F., and Gio-Argaez, F.R., 2015, Microfossils from the Early Pliocene Carmen Formation, Monserrat Island, Baja California Sur, Mexico: Micropaleontology, v. 61, no. 3, p. 199–225.

Crouch, R.W. and Poag, C.W., 1979, *Amphistegina gibbosa* d'Orbigny from the California borderlands: the Caribbean connection: Journal of Foraminiferal Research, 9 (2), 85-105.

Helenes J., Carreño, A.L., and Carrillo, R.M., 2009, Middle to late Miocene chronostratigraphy and development of the northern Gulf of California: Marine Micropaleontology, v. 72, p. 10-25.

Keigwin, L.D., 1982, Isotopic paleoceanography of the Caribbean and East Pacific: role of Panama uplift in late Neogene time: Science, v. 217 (4557), p. 350-353.

Kleinpell, R.M., 1938, Miocene Stratigraphy of California: American Association of Petroleum Geologists, Tulsa, Oklahoma, 450 pp.

Lourens, L., Hilgen, F., Schackleton, N.J., Laskar, J., and Wilson, J., 2004, Orbital tuning calibrations and conversions for the Neogene Period, *in* Gradstein, F.M., Ogg, G. and Smith, A.G. (eds.). A Geological Time Scale 2004: Cambridge University Press, p. 469-471.

McDougall, K.M., 2009, Update on microfossil studies in the northern Gulf of California and the Salton Trough: Margins 2009, poster.

Miranda-Martinez, A.Y., 2019, Edad de los depósitos ma rinos asociados a la evolución temprana del G olfo de California" [Age of Marine Deposits Associated with Early Evolution of the Gulf of California]: Universidad Nacional Autonoma de Mexico, PhD. Dissertation, 276 pp.

Miranda-Martínez, A. Y., Carreño, A. L., and McDougall, K., 2017, The Neogene genus *Streptochilus* (Brönnimann and Resig, 1971) from the Gulf of California. Marine Micropaleontology, v. 132, p. 35-52.

Resig, J.M., 1989, Stratigraphic distribution of late Neogene species of the planktonic foraminifer *Streptochilus* in the Indo-Pacific: Micropaleontology, v. 35(1), p. 49-62.

Resig, J.M., 1993, Cenozoic stratigraphy and paleoceanography of biserial planktonic foraminifers, Ontong Java Plateau, *in* Berger, W.H., Kroenke, L.W., and Mayer, L.A., eds., Proceedings of the Ocean Drilling Program, v. 130, p. 231-244.

Smith, P.B., 1964, Ecology of benthonic species U.S. Geological Survey Professional Paper 429-B, 55 pp.

Appendix I - Taxonomic Notes

Benthic Foraminifers

Amphistegina gibbosa d'Orbigny, 1839, p. 101. — Carreño et al., 2015, p. 224, pl. 3, fig. 19.

Range: Miocene to Holocene (Crouch and Poag, 1979)

Ecology: *Amphistegina gibbosa* is "normally most abundant in (but not restricted to) tropical and warm subtropical reef, near-reef, and bank biotopes having high $CaCO_3$ content, euhaline to hyperhaline waters, mean winter temperatures no less than 14°C, mean summer temperatures no less than 25°C, and depths not much greater than 100 m. It lives primarily as an epibiont on sea grasses and hard substrates, but it also can live in or on soft sediments." (Crouch and Poag, 1979, p. 92).

Bolivina argentea Cushman, 1926, Cushman Lab.,2, pt. 2, no. 29, p. 42, pl. 6, fig. 5. — Smith, 1964, p. B36. = *Brizalina argentea* (Cushman) — Matoba and Yamaguchi, 1982, p. 1040, pl. 1, figs 20A,B. — Carreño et al., 2015, p. 224, pl. 3, fig. 6.

Range: Pliocene to Holocene (Finger 1990)

Ecology: upper middle bathyal biofacies (Ingle, 1980; Bandy, 1961); upper bathyal (435 m), off Ecuador (Smith, 1964). This species is tolerant to low bottom-water oxygen (Khusid, 1974; Resig, 1981; Mallon et al., 2012) and can be used as a proxy for enhanced upwelling during interglacial periods (Heinze and Wefer, 1992).

Bolivina churchi Kleinpell and Tipton, 1980, p. 72, pl. 9, figs. 11, 12. — Carreño et al., 2015, p. 224, pl. 3, fig. 4.

Range: Miocene, Saucesian to Mohnian Stages (Finger, 1990)

Ecology: Ecologic conditions considered similar to *B. acuminata* Natland which has a UDL on the shelf edge transition (Ingle, 1980; Finger, 1990)

Bolivina interjuncta (Cushman) = *Bolivina costata* var. *interjuncta* Cushman, 1926, p. 42. = *Brizalina interjuncta bicostata* (Cushman) — Matoba and Yamaguchi, 1982, p. 1040pl. 1, fig. 21. = *Brizalina interjuncta* — Carreño et al., 2015, p. 224, pl. 3, fig. 3.

Ecology: upper bathyal (Ingle, 1980); rare specimens are found in the outer neritic biofacies, but this species becomes dominate near the shelf edge (Bandy, 1961); outer neritic off Ecuador (Smith, 1964)

Bolivina peirsonae Uchio, 1960, p.63-64, pl. 7, figs. 3,4.

Comments: This species is similar to *Suggrundi eckisi* but is larger and mor inflated (Uchio, 1960)

Ecology: found in the California borderland at a depth of 550 fathoms.

Bolivina seminuda Cushman, 1911, p. 34, fig. 55. = *Bolivinellina seminuda* (Cushman) — Smith, 1964, p. B37. — Matoba and Yamaguchi, 1982, p. 1036. — Carreño et al., 2015, p. 224, pl. 3, fig. 5.

Ecology: upper middle bathyal biofacies (Ingle, 1980); upper bathyal off Ecuador (Smith, 1964); this species is considered indicative of lower oxygen conditions (<0.2 ml/l) and found in the oxygen minimum zone (Phleger and Soutar, 1973; Hermelin and Shimmield, 1990; Bernhard et al., 1997; Ohga and Kitazato, 1997; Gooday et al., 2000; Glock et al., 2011; Cardich et al., 2012; Mallon, 2012; Caulle et al., 2014; Cardich et al., 2015; Erdem et al. 2020) and often suggests dysoxic conditions (Kaiho, 1994; Tetard et al., 2017). *Bolivina seminuda* can be used as a proxy for enhanced upwelling during interglacial periods (Heinze and Wefer, 1992).

Bolivina subadvena Cushman, 1926, p. 44, pl. 6, figs. 6a,b. — Matoba and Yamaguchi, 1982, p. 1036, pl. 1, figs. 15A,B, 16A,B, 17A,B. = *Brizalina subadvena* (Cushman) — Carreño et al., 2015, p. 224, pl. 3, fig. 7.

Ecology: UDL is is in the upper middle bathyal biofacies (Ingle, 1980)

Buccella frigida (Cushman) = *Pulvinulina frigida* Cushman, 1922, p. 12.

Ecology: UDL inner neritic (0-18 m; Bandy, 1961). Bandy (1961) notes UDL of *B. tenerrima* in beach fauna and that *B. mansfieldi* is a dominant species in the inner neritic fauna (0-18 m)

Buccella parkerae Andersen, 1952, p. 149, figs. 9a-c.

Bulimina denudata Cushman = *Bulimina pagoda* Cushman var. *denudata* Cushman and Parker, 1938, p. 57, pl. 10, figs. 1, 2. = *Bulimina denudata* Cushman and Parker — Bandy, 1953, p. 176, pl. 24, fig. 11. — White, 1956, p. 253, pl. 30, fig. 51,b. [spines form ruffle at base of chambers] — Uchio, 1960, p. pl. 6, fig. 3. — Smith, 1964, p. B32, pl. 2, fig. 12. — Smith,1964, B32, pl. 2, fig. 12. — Carreño et al., 2015, p. 224, pl. 3, fig. 8.

Comments: McGann (2006) [abstract forams 2006, 276-277] equals *B. denudata* with *B. marginata* and suggests the use of *B. denudata* abundance correlates with an increase in pollutants.

Ecology: *Bulimina denudata* ranges from the Oregonian to Panamanian provinces of Buzas and Culver (1990). It is found rarely off San Francisco where the cooler California surface waters dominate and commonly (10-20% of the fauna) south of Point Conception where warmer waters dominate (Ingle and Keller, 1980; Culver and Buzas, 1986). The upper depth limit of *Bulimina denudata* is in the inner neritic biofacies (Ingle and Keller, 1980). *Bulimina denudata* is a dominant species in the outer shelf assemblages of the nearshore basins in the California continental borderland (Douglas and Heitman, 1979) and the outer shelf (37-152 m) in the Gulf of California and off Ecuador (Bandy, 1961;

Bandy and Arnal, 1961; Smith, 1964). In the Gulf of California, specimens from 37 to 82 m well developed overhang of chambers; specimens from deeper water show little overhang and less developed spines (Bandy and Arnal, 1961).

Bulimina marginata d'Orbigny, 1826, p. 269, no. 4 pl. 12 fig. 10-12 — Carreño et al., 2015, p. 224, pl. 3, fig 9. — Lankford and Phleger, 1973, p. 116, pl. 4, fig. 11.

Ecology: inner neritic (Lankford and Phleger, 1973); dominates the outer neritic biofacies in the Gulf of California (Bandy and Arnal, 1961)

Buliminella curta Cushman, 1925, p. 33, pl. 5, fig. 13. — Natland, 1952, pl. 8, fig. 5a,b, 6a,b. — Carreño et al., 2015, p. 224, pl. 3, fig. 10, 11. — Smith, 1964, p. B33.

Range: Oligocene (Zemorrian) to Holocene (Finger, 1990)

Ecology: outer neritic biofacies (Ingle, 1980; Bandy, 1961); off Ecuador, the UDL is in the upper middle bathyal (800 m; Smith, 1964). Blake (1991) considers this species an indicator of low oxygen conditions.

Cancris auricula (Fichtel & Moll, 1798) = *Nautilus auricula* Fichtel and Moll, 1798, p. 108, pl. 20, figs. a–f. = *Cancris auriculus* (Fitchel and Moll) — Carreño et al., 2015, p. 224, pl. 4, fig. 9.

Ecology: inner neritic (Ingle, 1980); first appears in the outer neritic biofacies (37-73m) (Bandy, 1961)

Cancris carmenensis Natland, 1950, p. 32, pl. 9, figs.1a-c.— Smith, 1964, p. B45, pl. 5, fig. 6. — Carreño et al., 2015, p. 224, pl. 4, fig. 8.

Ecology: *Cancris baggi* is thought to indicate low-oxygen conditions and be associated with the oxygen minimum zone (Ingle, 1980); upper bathyal biofacies (435 m) off Ecuador (Smith, 1964)

Cassidulina corbyi Cushman and Hughes, 1925, p. 14, pl. 2, fig. 3. — Carreño et al., 2015, p. 224, pl. 3, fig. 26.

Cassidulina limbata Cushman and Hughes, 1925, p. 12, pl. 2, fig. 2. — Carreño et al., 2015, p. 224, pl. 3, fig. 27.

Ecology: upper bathyal (Ingle, 1980) Bandy (1961) notes rare occurrences of C. limbata on the inner neritic biofacies.

Cassidulina pulchella d'Orbigny, 1839 — Carreño et al., 2015, p. 224, pl. 3, fig. 28.

Ecology: upper bathyal biofacies of the Gulf of California (Bandy and Arnal, 1961)

Cassidulina tranlucens Cushman and Hughes, 1925, p. 15, pl. 2, fig. 5. — Carreño et al., 2015, p. 224, pl. 3, fig. 29.

Ecology: upper bathyal (Ingle, 1980; Bandy and Arnal, 1961)

Cassidulinella pliocenica Natland — Carreño et al., 2015, p. 224, pl. 4, fig. 1.

Ecology: Species of *Cassidulinella* have UDLs in the upper bathyal biofacies (Ingle, 1980)

Cibicides fletcheri Galloway and Wissler, 1927, p. 64, pl. 10. figs. 8,9. — Walton, 1955, p. 1005, pl 104, figs. 11,12. — Uchio, 1960, pl. 10, figs. 1-3. — Lankford and Phleger, 1973, p. 117, pl. 6, fig. 11.

Comments: Specimens assigned to this species have a more lobate periphery and chambers in the final whorl expand rapidly in the type specimen. Sutures curve equally on both sides.

Ecology: UDL is in the inner neritic biofacies (Walton, 1955: Ingle, 1980); Bandy (1961) notes UDL in lagoon and beach faunas.

Cibicides gallowayi Cushman and Valentine, 1930, p. 30, pl. 10, figs. 4a-v. — Natland, 1933. — Smith 1964, p. B47. — Carreño et al., 2015, p. 224, pl. 4, fig. 2.

Comments: Described as having a somewhat inflated final whorl with 6-7 chambers and may have slight keel. Type figures, however, resemble *Dyocibicides perforatus*. Illustrations by Carreño et al. (2015) are more circular.

Ecology: outer neritic biofacies (90-280 m) in the Catalina Channel (Natland, 1933); living specimens found between 5 and 35 fms in Todos Santos Bay but dead specimens found down to 215 fms (Walton, 1955).

Cibicides lobatulus (Walker and Jacob) = *Echinus lobatulus* Walker & Jacob, 1798, p. 642, pl. 14, fig. 36. — Carreño et al., 2015, p. 224, pl. 4, fig. 3. = *Cibicides* cf. *lobatulus* (walker and Jacob) — Matoba and Yamaguchi, 1982, p. 1041.

Comments: WORMS now considers this species to be *Lobatula lobatula* (Walker & Jacob, 1798)

Ecology: Inner neritic (Ingle, 1980; Bandy and Arnal, 1961)

Cibicidoides mckannai (Galloway and Wissler) = *Cibicides mckannai* Galloway and Wissler, 1927, p. 65, pl. 10, figs. 5a-6c. — Walton, 1955, p. 1006, pl. 104, figs. 13, 14. — Bandy, 1961, p. 15, pl. 3, fig. 4. — Smith, 1964, p. 47, pl. 6, fig. 4. — Matoba and Yamaguchi, 1982, p. 1041. — Carreño et al., 2015, p. 224, pl. 4, fig. 4.

Comments: Outer ends of sutures on spiral side curve but are straighter on the inner side. Sutures on the dorsal side are strongly curved.

Range: Luisian to Pliocene (Finger, 1990)

Ecology: upper bathyal (Ingle, 1980); species has a UDL in the outer neritic biofacies of the Gulf of California (Bandy, 1961) and of the coast of El Salvador (Smith, 1964).

Dyocibicides biserialis Cushman and Valentine, 1930, p. 31, pl. 10, figs 1,2. — Carreño et al., 2015, p. 224.

Dyocibicides perforata Cushman and Valentine, 1930, p. 31, pl. 10, fig. 3a-c.

Comments: The initial coiling whorls of *D. biserialis* and *D. perforata* are the same. The biserial portion of *D. biserialis* is not present in *D. perforata*. Carreño et al (2015) did not figure the specimens found so it is not possible to determine the presence of the biserial portion. Specimens found in this study did not contain a biserial portion.

Elphidium articulatum d'Orbigny, 1839, p. 30, p. 3, figs. 9,10. — Carreño et al., 2015, p. 224

Ecology: found in the lagoonal and beach biofacies in the Gulf of California (Bandy and Arnal, 1961)

Elphidium crispum (Linne) = *Nautilus crispus* Linne, 1758, p. 709. = *Elphidium crispum* (Linne) — Bandy, 1961, p. 15. — Walton, 1955, p. 1007, pl. 101, fig. 11. — Lankford and Phleger, 1973, p. 119, pl. 3, fig. 25. = *Elphidium granti* Kleinpell, 1938, p. 238, pl. 19, figs. 1, 11. — Carreño et al., 2015, p. 224, pl. 4, fig. 6.

Range: Saucesian to Pliocene (Finger, 1990)

Ecology: inner neritic (Ingle, 1980); none found living in Todos Santos Bay but specimens were found in areas of relict sediments (Walton, 1955).

Elphidium macellum (Fitchel and Moll) — Carreño et al., 2015, p. 224, pl. 4, fig. 5.

Epistominella smithi (Stewart and Stewart) = *Pulvinulinella smithi* Stewart and Stewart, 1930, p. 70, pl. 9, fig. 4.

Ecology: Upper bathyal in the Gulf of Califonria (Bandy, 1961).

Eponides repandus (Fitchel and Moll) = *Nautilus repandus* Fitchel and Moll, 1798, p. 35, pl. 3, figs a-d.

Ecology: Bandy (1961) notes UDL in the inner neritic biofacis (0-18 m).

Eubuliminella basispinata (Stewart & Stewart, 1930) = *Buliminella curta basispinata* Stewart and Stewart, 1930, p. 63, pl. 8, fig. 6. — Matoba and Yamaguichi, 1982, p. 1041, pl. 1, fig. 3. = *Buliminella basispinata* (Stewart and Stewart) — Carreño et al., 2015, p. 224, pl. 3, fig. 25.

Eubuliminella exilis (Brady, 1884) = *Buliminella subfusiformis* var. *tenuata* Cushman, 1927, p. 149, pl. 2, fig. 9. = *Buliminella tenuata* (Cushman) — Carreño et al., 2015, p. 224, pl. 3, fig. 12. = *Buliminella exilis* var. *tenuata* Cushman — Bandy and Arnal, 1957, p. 2050.

Ecology: upper middle bathyal (Ingle, 1980); upper bathyal in the Gulf of California (Bandy and Arnal, 1961); off Ecuador this species has an upper depth limit in upper bathyal biofacies (435 m; Smith, 1964)

Euloxostomum bradyi (Asano) = *Bolivina bradyi* Asano, 1938, p. 603, pl. 16, fig. 2. — Smith, 1964, p. B36. = *Loxostmum bradyi* (Asano). = *Euloxostomum instabile* (Cushman and McCulloch) — Carreño et al., 2015, p. 224. = *Loxostoma instabile* Cushman & McCulloch, 1942

Ecology: UDL off Ecuador is in the outer neritic biofacies (Smith, 1964)

Euloxostomum pseudobeyrichi (Cushman, 1926) = *Bolivina pseudobeyrichi* Cushman, 1926, p. 4. = *Loxostomum pseudobeyrichi* (Cushman) — Matoba and Yamaguchi, 1982, p. 1045, pl. 1, figs. 25A,B. — Carreño et al., 2015, p. 224, pl. 3, fig. 16.

Ecology: upper bathyal (Ingle, 1980; Bandy, 1961; Smith, 1964) This species is considered an indicator of low oxygen conditions and the oxygen minimum zone (Ingle, 1980)

Fissurina sp. — Carrino et al., 2015, pl. 2, fig. 6.

Fursenkoina bramletti (Galloway and Morrey) = *Virgulina bramletti* Galloway and Morrey, 1929, p. 37, pl. 5, fig. 14. — Walton, 1955, p. 101, pl. 102, fig. 18. — Smith, 1964, p. B33. = *Virgulina californiensis* Cushman — Carreño et al., 2015, p. 224, pl. 3, fig. 24

Comments: Smith (1964) suggests that *F. schreibersiana* is more elongate than *F. bramletti* and that *F. bramletti* is closely related to *F. pontoni.* These species are all similar in appearance and maybe variations of the same species.

Ecology: *Fursenkoina bramletti*, *F. schreibersiana* and *F. pontoni* have UDLs in the inner neritic biofacies of the Gulf of California (Bandy, 1961), along the Pacific coast of Baja (Walton, 1955), Pacific Coast (Bandy and Arnal, 1957; Uchio, 1960; Smith, 1964; Lankford and Phleger, 1973).

Galliherina uvigerinaformis (Cushman and Kleinpell) = *Bulimina uvigerinaformis* Cushman and Kleinpell, 1934, p. 5, pl. 1, figs. 14a-b. = *Galliherina uvigerinaformis* (Cushman and Kleinpell) — Carreño et al., 2015, p. 224, pl. 3, fig. 13.

Range: Late Miocene, Mohnian to Delmontian Stages (Finger, 19990)

Ecology: upper middle bathyal (Ingle, 1980)

Globobulimina ovula (d'Orbigny) = *Bulimina ovula* d'Orbigny, 1839, p. 51, pl. 1, figs. 10,11. = *Globobulimina ovula* (d'Orbigny) — Matoba and Yamaguchi, 1982, p. 1042. — Carreño et al., 2015, p. 224, pl. 3, fig. 14.

Ecology: upper middle bathyal (Ingle, 1980).

Guttulina quinquecosta Cushman and Ozawa, 1930, p. 19, pl. 5, fig. 6. — Carreño et al., 2015, p. 224.

Gyroidina rothwelli Natland, 1950, p. 29, pl. 7, figs. 8a-c. — Matoba and Yamaguchi, 1982, p. 1045, pl. 4, figs. 7A-C. — Carreño et al., 2015, p. 224, pl. 4, fig. 10.

Ecology: upper bathyal (Bandy, 1961)

Gyroidina soldanii d'Orbigny, 1826, p. 278. — Matoba and Yamaguchi, 1982, p. 1045. = *Hansenisca soldanii* (d'Orbigny) — Carreño et al., 2015, p. 224, pl. 4, fig. 11.

Ecology: lower bathyal (Ingle, 1980; Bandy and Arnal, 1957; Bandy, 1961; Smith, 1964)

Hanzawaia nitidula (Bandy) = *Cibicidina basiloba* (Cushman) var. *nitidula* Bandy, 1953, p. 178, pl. 22, figs. 3a-c. = *Hanzawaia nitidula* (Bandy) — Carreño et al., 2015, p. 224, pl. 4, fig. 12.

Ecology: outer neritic (Ingle, 1980); dominant in the inner neritic (0-18 m; Bandy, 1961) but continues to be present down to lower bathyal depths in the Gulf of California (Bandy and Arnal, 1961)

Islandiella californica (Cushman and Hughes) = *Cassidulina californica* Cushman and Hughes, 1925, p. 12, pl. 2, figs. 1a-c. = *Islandiella californica* (Cushman and Hughes) — Matoba and Yamaguchi, 1982, p. 1045. — Carreño et al., 2015, p. 224.

Range: Saucesian to Holocene (Finger, 1990)

Ecology: upper bathyal (Ingle, 1980)

Lagena hexagona (Williamson) = *Oolina hexagona* (Williamson) — Carreño et al., 2015, pl. 2, figs. 7.

Lagena spp. — Carreño et al., 2015, pl. 2, figs. 8,9.

Melonis affinis (Reuss) = *Nonionina affinis* Reuss, 1851, p. 72, pl. 5, fig. 32.

Ecology: lower middle bathyal in the Gulf of California (Bandy, 1961)

Neoconorbina tequemi (Rzehak) = *Discorbina terquemi* Rzehak, 1888, p. 228. = ?*Rosalina orbicularis* Terquem, 1876, (not d'Orbigny, 1850), p. 166, pl. 9, fig. 4a,b. = *Neoconorbina* sp. cf. *N. terquemi* (Rzehak) — Lankford and Phleger, 1973, p. 123, pl. 4, fig. 23.

Ecology: inner neritic, < 20 m (Lankford and Phleger (1973).

Nonionella basispinata (Cushman and Moyer) = *Nonion pizarrensis basispinata* Cushman and Moyer, 1930, p. 54, pl. 7, fig. 18.

Ecology: Bandy (1961) notes UDL in the inner neritic biofacies (0-18 m) and continued appearance into the upper bathyal biofacies (366-610 m).

Peneroplis pertusus (Forsskal *in* Niebuhr) = *Nautilus pertusus* Forsskal, 1775, p. 125.

Ecology: Bandy (1961) notes rare *P. pertusus* in the inner and outer neritic biofacies down to 152 m

Planogypsina acervalis (Bardy) = *Planorbulina acervalis* Brady, 1884, p. 657, pl. 92, fig. 4. — Carreño et al., 2015, p. 224, pl. 4, fig. 7.

Planulina ariminensis d'Orbigny, 1826, p. 280, model no. 49, pl. 14, figs. 1-3. — Carreño et al., 2015, p. 224, pl. 4, fig. 13.

Ecology: outer neritic (Ingle, 1980; Bandy and Arnal, 1961)

Planulina ornata (d'Orbigny) = *Truncatulina ornata* d'Orbigny, 1839, p. 40, pl. 6, figs. 7-9. = *Planulina ornata* (d'Orbigny) — Carreño et al., 2015, p. 224, pl. 4, fig. 14.

Range: L. Luisian to early Delmontian (Kleinpell, 1938); Saucesian to Pliocene, Holocene (Finger, 1990).

Ecology: outer neritic (Ingle, 1980); dominant species in the outer neritic biofacies of the Gulf of California (Bandy, 1961; Bandy and Arnal, 1961); Off Ecuador this species has a UDL in the upper middle bathyal biofacies (800 m; Smith, 1964).

Planulinoides biconcavus (Parker and Jones) = *Discorbina biconcava* Parker and Jones *in* Carpenter et al., 1862 = *Planulinoides biconcava* (Jones and Parker) — Carreño et al., 2015, p. 224, pl. 4, fig. 15.

Polymorphina sp

Mucronina compressa (Costa) = *Frondicularia compressa* Costa, 1855, p. 372, pl. 3, fig. 2. = *Proxiforms advena* (Cushman) — Carreño et al., 2015, p. 224, pl. 3, fig. 18.

Range: *Frondicularia advena* ranges from Miocene, Saucesian Stage to Pliocene, Holocene (Finger, 1990)

Ecology: lower middle bathyal (Ingle personal communication in Finger, 1990)

Pseudoparrella bradyana (Cushman) = *Pulvinulinella bradyana* Cushman, 1927, p. 165, pl. 5, figs. 11-13. = *Epistominella bradyana* Cushman — Smith, 1964, p. B43, p. 4, figs. 5a,b. = *Pseudoparrella bradyana* (Cushman) — Matoba and Yamaguchi, 1982, p. 1045, pl. 3, figs. 2A-C. — Carreño et al., 2015, p. 224, pl. 4, fig. 16.

Comment: Lipps (1965) considers *P. bradyana* a junior synonym of *P. subperuviana*; WORMS considers *Pseudoparella bradyana* the accepted name.

Range: *P. subperuviana* ranges from Oligocene, Zemmorrian Stage to Pliocene, Holocene (Finger, 1990)

Ecology: transitional between outer neritic and upper bathyal (Ingle, 1980); dominant species in the outer neritic-upper bathyal biofacies of the Gulf of California (Bandy and Arnal, 1961); outer neritic off Ecuador (Smith, 1964).

Pseudoparrella subperuviana (Csuhman) = *Pulvinulinella subperuviana* Cushman, 1926, p. 73-80, pl. 9, fig. 9. — Kleinpell, 1938, p. 329-330, pl. 10, figs. 10a-c. — Carreño et al., 2015, pl. 4, fig. 17. = *Pulvinulinella* (*Epistominella*) cf. *subperuviana* Cushman — Natland, 1952, pl. 16, fig. 4a,b,c, 5a,b,c.= *Epistominella subperuviana* (Cushman) — Bandy and Arnal, 1969, p. 788. — Haller, 1980, p. 254, pl. 10, fig. 7a,b,c. — McDougall, 1985, p. 393. = *Pseudoparrella subperuviana* (Cushman) — Finger, 1990, p. 210-211, plate-figs. 1-9.

Comments: Kleinpell (1938) concludes that *E. relizensis* is closely related to *E. subperuviana* and that one may be a variety of the other.

Range: Miocene, late Saucesian through late Luisian *(Pulvinulinella relizensis*) and early Saucesian to late Luisian (*Pullvinulinella subperuviana*) (Kleinpell, 1938); Bandy and Arnal (1969) find this species ranges from the Saucesian through the Relizian with rare occurrences in the Zemorrian and Luisian through Mohnian strata of the southern San Joaquin Valley; Oligocene to Holocene (Finger, 1990); FO in late Saucesian (Kleinpell, 1980).

Ecology: upper bathyal biofacies (Ingle, 1980; Resig, 1981); *Pseudoparrella subperuviana* first appears at the shelf edge (Ingle and Keller, 1980). Resig (1981) finds this species associated with temperatures of 7-13° C, a salinity of 34.6 $^{0}/_{00}$ and an oxygen content of less than 1 ml/l.

Pullenia bulloides (d'Orbigny) = *Nonionina bulloides* d'Orbigny, 1846, p. 107, pl. 7, figs. 9-10. = *Bermudezinella riveroi* (Bermudez) — Carreño et al., 2015, p. 224.

Ecology: lower bathyal biofacies in the Gulf of California (Bandy, 1961).

Pullenia quinqueloba (Reuss) = *Nonionina quinqueloba* Reuss, 1851, p. 71, pl. 5, fig. 31. = *Pullenia quinqueloba* (Reuss) — Matoba and Yamaguchi, 1982, p. 1045. — Carreño et al., 2015, p. 224, pl. 4, fig. 18.

Ecology: upper middle bathyal (Ingle, 1980)

Quinqueloculina akneriana d'Orbigny, 1846, p. 290, pl. 18, figs. 16-21.

Ecology: Bandy (1961) notes first appearance in lagoonal and beach faunas

Quinqueloculina lamarkina d'Orbigny, 1839, p. 189, pl. 11, figs. 14,15.

Ecology: Bandy (1961) notes UDL in beach faunas.

Rectobolivina hancocki (Cushman and McCulloch) = *Bifarina hancocki* Cushman and McCulloch, 1942, p. 225, pl. 28, figs. 13-19.

Ecology: Ecology: Bandy (1961) notes rare occurrences of this species from neritic through bathyal biofacies.

Reussella pacifica Cushman and McCulloch, 1948, p. 251, pl. 31, fig. 6. = *Reussella spinulosa* (Reuss) — Carreño et al., 2015, p. 224, pl. 3, fig. 15.

Ecology: Bandy (1961) notes UDL in the inner neritic biofacies (0-18 m)

Rotorbinella campanulata (Galloway and Wissler) = *Globorotalia campanulata* Galloway and Wissler, 1927, p. 58, pl. 9, fig. 14. = *Gavelinopsis campanulata* (Galloway and Wissler) — Carreño et al., 2015, p. 224 = *Rosalina campanulata* (Galloway and Wissler) — Uchio, 1960, p. 66, pl. 7, fig. 26.

Ecology: inner neritic biofacies (Uchio, 1960)

Sigmoilina tenuis (Czjzek) = *Quinqueloculina tenuis* Czjzek, 1848, p. 149, pl. 13, figs. 31-34. = *Sigmoilina tenuis* (Czjek) — Matoba and Yamaguchi, 1982, p. 1048, pl. 1, figs. 1a,b. — Carreño et al., 2015, p. 224, pl. 3, fig. 20.

Strictocostella advena (Cushman and Laiming, 1931) = *Nodogenerina advena* Cushman and Laiming, 1931, p. 106, pl. 11, fig. 19. — Carreño et al., 2015, p. 224, pl. 3, fig. 17. = *Strictocostella advena* (Cushman and Laiming, 1931) — Hayward et al., 2012, p. 187, pl. 21, figs. 13-19.

Range: early Oligocene to early Pleistocene (>0.80 Ma)

Ecology: middle bathyal to upper abyssal (900-2600 m; Hayward et al., 2012).

Suggrundia eckisi Natland, 1950, p. 23, pl. 9, figs. 12a,b. — Matoba and Yamaguchi, 1982, p. 1049, pl. 3, figs. 10a,b. — Carreño et al., 2015, p. 224, pl. 3,fig. 21. — Smith, 1964, p. B38

Ecology: upper bathyal (Ingle, 1980); indicative of low oxygen conditions and the oxygen minimum zone (Ingle, 1980); dominant species in the upper bathyal of the Gulf of California (Bandy and Arnal, 1961)

Takayanagia delicata (Cushman) = *Cassidulina delicata* Cushman, 1927, p. 168, pl. 6, fig. 5. — Uchio, 1960, XX— Smith, 1964, p. B39. = *Paracassidulina delicata* (Cushman) — Finger, 1990, p. 186, fig. 5, plate-figs 1-2, plate-figs. 3-8. = *Takayanagia delicata* (Cushman) — Carreño et al., 2015, p. 224, pl. 4, fig. 19.

Range: Relizian to Pliocene, Holocene (Finger, 1990)

Ecology: upper middle bathyal transition (Uchio, 1960; Ingle, 1980); upper bathyal in the Gulf of California (Bandy, 1961); oxygen minimum indicator (Blake, 1981).

(Erdam et al., 2020) *Cassidulina delicata* Common in the eastern Pacific OMZs at the lower continental slope (Uchio, 1960; Ingle et al., 1980) and under intermediate bottom-water oxygen concentrations, lowest observed is 4.5 μmol kg□1 (Golik and Phleger, 1977; Douglas and Heitman, 1979; Resig, 1981; Mackensen and Douglas, 1989; Kaiho, 1994); used as a proxy for dysoxic conditions (Tetard et al., 2017).

Textularia lateralis Lalicker, 1935, p. 1, pl. 1, figs 3-5. — Carreño et al., 2015, p. 224, pl. 3, fig. 22.

Comments: looks like T. schencki

Ecology: T. schencki dominant in the neritic (0-152 m) biofacies of the Gulf of California (Bandy and Arnal, 1961)

Tidwellella exorna (Phleger and Parker) = *Planulina exorna* Phleger and Parker, 1951, p. 32, pl. 18, figs. 5-8.

Ecology: middle neritic biofacies in the Gulf of Mexico (~57 m; Phleger and Parker, 1951; (Pflum and Frerichs, 1976).

Trifarina angulosa (Williamson) = Uvigerina angulosa Willamson, 1858, p. 67, pl. 5, fig. 140. = *Angulogerina angulosa (Williamson)* — Uchio, 1960, pl 7, fig. 18. = *Trifarina carinata* (Cushman) = *Angulogerina carinata* Cushman, 1927, p. 159, pl. 4, fig. 3. — Uchio, 1960, p. 66, pl. 7, fig.19. — Matoba and Yamaguchi, 1982, p. 1036. — Carreño et al., 2015, p. 224, pl. 3, figs. 1.

Comments: Specimens from the Yu samples do not have any striae.

Ecology: species of *Trifarina* have a transitional distribution from the outer neritic to the upper bathyal biofacies and therefore consider diagnostic of the shelf-edge (Ingle, 1980; Smith, 1964).

Trifarina carinata (Cushman) = *Angulogerina carinata* Cushman, 1927, p. 159, pl. 4, fig. 3.

Comments: Now place in synonymy with *T. angulosa* by Hayward et al., 2010.

Ecology: Bandy (1961) notes rare occurrences of this species in the neritic and bathyal biofacies

Trifarina hughesi (Galloway and Wissler) = *Uvigerina hughesi* Galloway and Wissler, 1927, p. 76, pl. 12, fig. 5. = *Angulogerina hughesi* (Galloway and Wissler) — Carreño et al., 2015, p. 224, pl. 3, fig. 2.

Ecology: species of *Trifarina* have a transitional distribution from the outer neritic to the upper bathyal biofacies and are therefore consider diagnostic of the shelf-edge (Ingle, 1980); rare specimens are found on the shelf in the Gulf of California from the inner neritic on (Bandy and Arnal, 1961).

Trifarina occidentalis (Cushman) = *Uvigeirna occidentalis* Cushman, 1923, p. 169.

Ecology: outer neritic/upper bathyal low oxygen (Ingle, 1980).

Uvigerina peregrina Cushman, 1925, p. 166, pl. 42, figs. 7-10.

Ecology: upper bathyal (Bandy, 1961)

Uvigerina excellens Todd, 1948, p. 258, pl. 33, fig. 2. — Smith, 1964, p. B34, pl. 2, fig. 13a,b. — Matoba and Yamaguchi, 1982, p. 1049, l 2, figs. 9. — Carreño et al., 2015, p. 224, pl. 3, fig. 23.

Ecology: upper bathyal (Bandy and Arnal, 1961; Smith, 1964)

Uvigerina peregrina Cushman, 1923, p. 166, pl. 42, figs. 7-10.

Ecology: upper bathyal (Ingle, 1980).

Valvulineria inflata (d'Orbigny) = *Valvulina inflata* d'Orbigny, 1839, p. 48, pl. 7, figs. 7-9 — Matoba and Yamaguchi, 1982, p. 1050. — Carreño et al., 2015, p. 224, pl. 4, fig. 20.

Comments: Natland (1950) notes the close resemblance of *C. panamensis* and *V. inflata* and suggests that *V. inflata* should be considered a *Cancris*.

Ecology: upper bathyal biofacies (Bandy, 1961)

Planktic Foraminifers

Dentigloborotalia anfracta (Parker, 1967) = *Tenuitella anfracta* (Parker, 1967) — Miranda-Martinez, 2019, p. 107, table 7.

Range: PL1 (N18; 5.20-5.72 Ma) to extant; FO is 5.8 in the Pacific (Kennett and Srinivasan, 1983).

Ecology: Tropical (Kennett and Srinivasan, 1983; Brinton and Douglas, 1986)

Globigerina bulbosa LeRoy, 1944, 1969 — Miranda-Martinez, 2019, p. 107, table 7.

Globigerina bulloideus d'Orbigny, 1826 — Miranda-Martinez, 2019, p. 107, table 7. = *Globigerina bulloides bulloides* d'Orbigny — Carreño et al., 2015, p. 224, pl. 1, fig. 1.

Range: O5-extant

Ecology: cosmopolitan species but most abundant in the middle and high latitudes; indicator of high productivity (Naidu and Malmgren, 1966; Coulbourn et al, 1980; Divakar, 1990; Chaisson and Leckie, 1993; Kucera, 2007; Kumar and Srinivasan, 2016)

Globigerina falconensis (Blow, 1959) = *Globoturborotalia falconensis* Blow 1959 — Miranda-Martinez, 2019, p. 107, table 7.

Range: M4 (N7; 16.38-17.54 Ma)

Ecology: high latitudes, temperate water masses (Kennett and Srinivasan, 1983); subtropical (Antonarakou et al, 2007; Kucera and Schonfeld, 2007)

Globigerina multiloba Romeo, 1965 1969 — Miranda-Martinez, 2019, p. 107, table 7.

Globigerina parabulloides Blow, 1959 — Miranda-Martinez, 2019, p. 107, table 7.

Globigerina sp.

Globigerina umbilicata Orr and Zaitzeff, 1971

Range: PL5 (N21; 1.93-3.1 Ma) – PT1 (N22; 0.0-1.93 Ma)

Ecology: temperate species (Kennett and Srinivasan, 1983)

Globigerinella calida (Parker, 1962) = *Globigerina calida praecalida* Blow, 1969 — Miranda-Martinez, 2019, p. 107, table 7.

Range: PL2 (N19; 4.74 Ma) to extant; FO is 0.22 Ma (Chaproniere et al., 1994; Wade et al., 2011)

Ecology: Tropical (Kennett and Srinivasan, 1983; Ave et al., 2011); also considered a marker for subtropical (Kucera, 2007; Kucera and Schonfeld, 2007)

Globigerinella siphonifera d'Orbigny1839 — Carreño et al., 2015, p. 224. = *Hastigerina siphonifera* (d'Orbigny, 1839) — Carreño et al., 2015, pl. 1, fig. 11a,b. = *Globigerinella aequilateralis* Brady,1879 — Miranda-Martinez, 2019, p. 107, table 7.

Range: M9 (N12; 11.79-13.41 Ma) to extant

Ecology: Tropical (Bandy, 1961; Bradshaw, 1959)

Globigerinita glutinata (Egger, 1893) — Carreño et al., 2015, p. 224, pl.1, fig. 3a,b. = *Globigerinita flparkerae* Bronnimann and Resig, 1971 — Miranda-Martinez, 2019, p. 107, table 7. = *Tinophodella glutinata* (Egger, 1893) — Miranda-Martinez, 2019, p. 107, table 7.

Range: O2(30.38-32.10 Ma) to extant

Ecology: tropical to subpolar, abundant in warm and temperate water (Kennett and Srinivasan, 1983; Pearson et al, 2018); high productivity (Bandy, 1961; Coulbourn et al., 1980; Hemleben et al., 1989; Chaisson, 1995; Kumar and Srinivasan, 2016)

Globigerinita uvula (Ehrenberg, 1861) — Carreño et al., 2015, p. 224, pl.1, fig. 4. = *Globigerinita* cf. *uvula* — Miranda-Martinez, 2019, p. 107, table 7.

Range: O5(26.93-28.09 Ma) to extant.

Ecology: indicates high productivity (Boltovskoy et al., 2000; Antonarakou et al, 2007; Rasmussen and Thomsen, 2008)

Globigerinoides extremus Bolli, 1957 — Carreño et al., 2015, p. 224, pl. 1, fig. 9.

Range: M13a (8.9 Ma) to PL6 [Atl](2.0 Ma); FO is 8.94 Ma; LO is 1.98 Ma (Chaisson and Pearson, 1997; Wade et al., 2011); FO in the South Pacific is 6.9 Ma , 8.5 Ma in the North Pacific, and 8.3 Ma in the equatorial Pacific (Keller,1980, 1981; Chaisson and Leckie, 1993; Anthonissen and Ogg, 2012).

Ecology: tropical to cool subtropical (Kennett and Srinivasan, 1983; low latitudes Ave et al. (2011)

Globigerinoides conglobatus (Brady, 1879) — Carreño et al., 2015, p. 224, pl. 1, fig. 8. — Miranda-Martinez, 2019, p. 107, table 7

Range: M13b (6.5 Ma) to extant; FO is 6.20 Ma (Chaisson and Pearson, 1997; Wade et al., 2011); 5.2 Ma in the Pacific (Saito et al., 1975, 1977; Ryan et al., 1974); 5.5 Ma in the Equatorial Pacific (Thunell, 1981); 6.2 Ma in the equatorial Atlantic (Anthonisson and Ogg (2012).

Ecology: tropical to warm subtropical (Bandy, 1961; Kennett and Srinivasan, 1983; Brinton and Douglas, 1986; Kucera, 2007; Kucera and Schofeld, 2007)

Globigerinoides obliquus Bolli, 1957 — Carreño et al., 2015, p. 224, pl. 1, fig, 10. — Miranda-Martinez, 2019, p. 107, table 7

Range: M1b (21.22-22.4 Ma) to PT1a (1.3 Ma); LO 1.30 Ma (Chaisson and Pearson, 1997; Wade et al., 2011); L in the Pacific is 1.63-1.76 Ma and 2.78 in the equatorial Pacific (Saito et al., 1975, 1977; Thompson and Sciarillo,1978; Shackleton et al., 1995)

Ecology: Cosmopolitan in middle and high latitudes (Spezzaferri et al., 2018); indicates low productivity (Boltovskoy et al., 2000; Antonarakou et al, 2007; Rasmussen and Thomsen, 2008)

Ecology: cosmopolitan (Spezzaferri et al., 2018)

Globigerinoides ruber (d'Orbigny, 1839) — Carreño et al., 2015, p. 224, pl. 1, fig. 7. — Miranda-Martinez, 2019, p. 107, table 7

Range: M11 (N14; 10.46-11.63 Ma) to extant; LO G, ruber (pink) is 0.12 Ma (Thompson et al, 1979; Wade et al., 2011)

Ecology: warm to cool subtropical (Kennett and Srinivasan, 1983); indicates low productivity (Bandy, 1961; Geraga et al., 2000; Toledo et al., 2008)

Globoquadrina conglomerata (Schwager, 1866) = *Globigerina conglomerata* (Schwager, 1866) 1969 — Miranda-Martinez, 2019, p. 107, table 7.

Range: PL2 (3.85-4.37 Ma) to extant; FO is 5.3 Ma in the South Pacific (Chaisson and Leckie, 1993); LO is 0.61 Ma in the Pacific and 3.3 Ma in the equatorial Pacific (Thompson and Sciarillo, 1978; Keigwin , 1982)

Ecology: Tropical (Kucera and Schonfeld, 2007; Ave et al., 2011)

Globorotalia crassaformis Galloway and Wissler — Carreño et al., 2015* — Miranda-Martinez, 2019, p. 107, table 7

Range: PL2 (4.3 Ma) to extant; FO is 4.31 Ma (Chaisson and Pearson, 1997; Wade et al., 2011); ranges from 4.41 to 4.9 Ma in the South Pacific (Srinivasan and Sinha,1992), 4.4 Ma in the North Pacific (Keller, 1979), and 3.48 in the equatorial Pacific (Keigwin,1982).

Ecology: warm subtropical to temperate (Kennett and Srinivasan, 1983; Kucera, 2007)

Goboconella inflata (d'Orbigny) = *Globorotalia inflata* (d'Orbigny, 1839) — Miranda-Martinez, 2019, p. 107, table 7

Range: PL5 [Atl] (2.39-3.13 Ma) to extant; FO in the North Pacific is 3.3 Ma (Keigwin, 1982)

Ecology: sub-antarctic to warm subtropical areas (Kennett and Srinivasan, 1983; Aze et al., 2011); temperate water masses (Bandy, 1961; Kucera, 2007; Kucera and Schonfeld, 2007)

Globorotalia menardii (Parker, Jones, and Brady, 1865) — Carreño et al., 2015, pl. 2, fig. 1a,b. — Miranda-Martinez, 2019, p. 107, table 7

Range: M9 (N12; 11.79-13.41 Ma) to extant

Ecology: tropical to warm subtropical (Kennett and Srinivasan, 1983; Kennett et al, 1985)

Globorotalia plesiotumida Banner and Blow, 1965 — Miranda-Martinez, 2019, p. 107, table 7.

Range: M13b (8.6 Ma) to PL3[Atl] (3.8 Ma); FO is 8.58 Ma and LO is 3.77 Ma (Chaisson and Pearson, 1997; Wade et al., 2011); FO is 5.6-5.57 Ma in the south Pacific (Beggren et al., 1995), 5.1 Ma in the North Pacific (Keller, 1979) and 5.2 to 5.59 in the equatorial Pacific (Saito et al, 1975,1977; Keigwin, 1982; Schackleton et al., 1995; Lourens et al., 2004; Anthonissen and Ogg, 2012) and ranges from 5.6 to 5.82 Ma in the equatorial Atlantic (Beggren et al., 1985; Chaisson and Pearson, 1997; Anthonissen and Ogg, 2012)

Ecology: tropical (Kennett and Srinivasan, 1983)

Globorotalia scitula (Brady, 1882) — Miranda-Martinez, 2019, p. 107, table 7 .

Range: M6 (N9; 14.24-15.01 Ma)

Ecology: tropical to temperate (Kennett and Srinivasan, 1983; Ave et al., 2011); temperate water masses (Kucera, 2007; Antonarakou et al, 2007)

Globorotalia tumida (Brady, 1877) = *Globigerinoides tumida* Brady, 1877. — Carreño et al., 2015, p. 224. — Miranda-Martinez, 2019, p. 107, table 7. = *Globorotalia tumida tumida* (Brady, 1877) — Carreño et al., 2015, pl. 2, fig. 2a,b.

Range: PL1[Atl] (5.7 Ma) to extant; FO in the Pacific is 5.59 Ma and in the Atlantic is 5.82 Ma (Shackleton et al., 1995; Chaisson and Pearson, 1997; Wade et al., 2011).

Ecology: tropical (Bradshaw, 1959; Bandy, 1961; Kennett and Srinivasan, 1983; Kucera, 2007)

Globoturborotalita apertura Cushman — Miranda-Martinez, 2019, p. 107, table 7.

Range: M11 (11.1 Ma) to PT1a (1.6 Ma); FO is 11.19 Ma; LO is 1.64 Ma (Caisson and Pearson, 1997; Wade et al., 2011)

Ecology: warm subtropical to temperate (Bandy, 1961; Kennett and Srinivasan, 1983; Serrano et al., 2007; Antonarakou et al., 2007)

Globoturborotalita decoraperta (Takayanagi and Saito, 1962) — Miranda-Martinez, 2019, p. 107, table 7.

Range: M11 (11.5 Ma) to PL5[Atl] (2.8 Ma); FO in the equatorial Pacific is 4.4 – 5.5 Ma (Thunell, 1981; Jenkins and Orr, 1972); LO is 2.75 Ma (Chaisson and Pearson, 1997; Wade et al., 2011)

Ecology: subtropical (Kennett and Srinivasan, 1983; Serrano et al., 2007)

Globoturborotalita rubescens (Hofker, 1956) — Miranda-Martinez, 2019, p. 107, table 7.

Range: PL2 (N20; 3.10-4.37 Ma) to extant; FO in th south Pacific is 3.5 MA and 3.0 Ma in the equatorial Pacific (chaisson and Lecki, 1993;

Ecology: tropical to warm subtropical (Kennett and Srinivasan, 1983; Serrano et al., 2007; Kucera and Schonfeld, 2007)

Globoturborotalita woodi Jenkins, 1960 — Miranda-Martinez, 2019, p. 107, table 7

Range: O4 (28.09-29.18 Ma) to PL6 [Atl] (2.3 Ma); LO is 2.33 Ma (Berggren et al, 1995b; Chaisson and Pearson, 1997; Wade et al., 2011); LO in the south Pacific is 1.9 Ma (Jenkins and Orr, 1972; Chaisson and Leckie, 1993).

Ecology: temperate, mid latitudes (Spezzaferri, 1994, 1995); indicates high productivity (Chaisson, 1995)

Neogloboquadrina acostaensis (Blow, 1959) — Carreño et al., 2015, p. 224, pl. 1, fig. 13a,b. — Miranda-Martinez, 2019, p. 107, table 7.

Range: M13a (9.8 Ma) to PT1a (0.61-1.88 Ma); FO is 9.82 Ma (Chaisson and Pearson, 1997; Wade et al., 2011)

Ecology: tropical to warm subtropical (Kennett and Srinivasan, 1983); indicator of high productivity (Hemleben et al., 1989; Antonarakou et al., 2007)

Neogloboquadrina dutertrei (d'Orbigny, 1839) — Carreño et al., 2015, p. 224, pl. 1, fig. 14a,b. — Miranda-Martinez, 2019, p. 107, table 7. = *Neogloboquadrina dutertrei blowi* Rogl and Bolli, 1973 — Miranda-Martinez, 2019, p. 107, table 7. = *Neogloboquadrina* cf. *dutertrei blowi* Rogl and Bolli, 1973 — Miranda-Martinez, 2019, p. 107, table 7

Range: PL1 (N19; 4.37-5.20 Ma) to extant; FO in the South Pacific is 2.77 Ma (Sinha and Singh, 2008).

Ecology: tropical to warm subtropical (Kennett and Srinivasan, 1983); indicates high productivity (Bandy, 1961; Coulborn et al, 1980; Hemleben et al., 1989; Chaisson and Leckie, 1993; Kucera, 2007)

Neogloboquadrina humerosa (Takayanagi and Saito 1962) — Miranda-Martinez, 2019, p. 107, table 7.

Range: M13b (8.6 Ma) to PT1a (0.61-1.88 Ma); FO is 8.50 Ma (Beggren et al., 1995b; Wade et al., 2011); LO in the Pacific is 1.15 Ma (Thompson and Sciarillo, 1978; Miranda-Martinez, 2019)

Ecology: tropical to subtropical (Kennett and Srinivasan, 1983; Ave et al., 2011)

Neogloboquadrina incompta (Cifelli, 1961) = *Paragloborotalia incompta* (Cifelli, 1961) — Miranda-Martinez, 2019, p. 107, table 7.

Range: M13a (N16; 8.58-9.83 Ma) to extant

Ecology: cold water (Kucera, 2007)

Neogloboquadrina pachyderma (Ehrenberg, 1862) — Carreño et al., 2015, p. 224, pl. 1, fig. 12a,b. — Miranda-Martinez, 2019, p. 107, table 7.

Range: M13a (N16; 8.58-9.83 Ma) to extant

Ecology: polar to warm subtropical (Kennett and Srinivasan, 1983); indicates cooler conditions (Kucera, 2007)

Neogloboquadrina acostaensis-humerosa — Miranda-Martinez, 2019, p. 107, table 7.

Orbulina universa d'Orbigny, 1839 — Carreño et al., 2015, p. 224, pl. 1, fig. 17. — Miranda-Martinez, 2019, p. 107, table 7.

Ecology: subtropical (Bandy, 1961; Brinton and Douglas, 1986; Antonarakou et al., 2007)

Paragloborotalia pseudopima (Blow, 1969) — Miranda-Martinez, 2019, p. 107, table 7.

Comments: original species citation is *Globorotalia (Turborotalia) acostaensis pseudopima* Blow, 1969

Pulleniatina cf. *praecursor* Banner and Blow, 1967 — Miranda-Martinez, 2019, p. 107, table 7.

Range: *Pulleniatina praecursor* ranges from PL1 (N19; 4.37-5.20 Ma) to PL5 (N21; 1.93-3.10 Ma); LO in is 1 Ma (Thompson and Sciarillo, 1978; Miranda-Martinez, 2019)

Ecology: *P. praecursor* is a tropical to warm subtropical species.

Pulleniatina obliquiloculata (d'Orbigny, 1865) — Carreño et al., 2015, p. 224, pl. 2, fig. 5a,b. — Miranda-Martinez, 2019, p. 107, table 7.

Range: PL1 (N19; 4.37-5.20 Ma) to extant

Ecology: tropical to warm subtropical (Bradshaw, 1959; Bandy, 1961; Kennett and Srinivasan, 1983; Kucera, 2007)

Pulleniatina primalis Banner and Blow — Carreño et al., 2015, p. 224, pl. 2, fig. 4a,b. — Miranda-Martinez, 2019, p. 107, table 7.

Range: M13b (6.8 Ma) to PL3 (3.7 Ma); FO is 6.40 Ma; LO is 3.65-3.66 Ma (Beggren et al., 1995a; Wade et al., 2011; Anthonissen and Ogg, 2012; Pearson and Penny, 2021); FO in the south Pacific is 5.7 to 6.6 Ma, 5.7 Ma in the North Pacific and 5.49 to 6.4 in the equatorial Pacific (Ryan et al., 1974; Keller, 1981; Thunell, 1981; Keigwin, 1982; Berggren et al., 1985; Berggren et al., 1995; Sinha and Singh, 2008; Anthonissen and Ogg, 2012). A sinistral to dextral coiling change occurs at 4.07 Ma (Chaisson and Pearson, 1997; Srinivasan and Sinha, 2000; Wade, 2011; Pearson and Penny, 2021). Older coiling changes have not been documented, except by Miranda- Martinez (2019) who noted a change at ≤5.8 to 5.6 Ma in the Gulf of California.

Ecology: tropical (Kennett and Srinivasan, 1983; Srinivasan and Sinha, 2000)

Pulleniatina primalis-praecursor — Miranda-Martinez, 2019, p. 107, table 7.

Streptochilus inglei Miranda-Martinez, Carreño and McDougall, 2019— Miranda-Martinez, 2019, p. 107, table 7.

Range: M14[Pac] (5.60-6.1 Ma) to PL1[Pac] (4.37-5.60 Ma)

Ecology: indicates high productivity (Hemleben et al., 1989; Resig and Kroopnick, 1983; Smart and Thomas, 2006; Darling et al., 2009)

Streptochilus latus Bronniman and Resig, 1971 — Miranda-Martinez, 2019, p. 107, table 7.

Range: M13a (N16; 8.58-9,83 Ma) to M14 (N17b; 5.72-6.60 Ma); FO in the equatorial Pacific is 8.1-7.45 Ma and the LO is 5.4-5.2 (Resig,1989, 1993).

Ecology: indicates high productivity (Hemleben et al., 1989; Resig and Kroopnick, 1983; Smart and Thomas, 2006; Darling et al., 2009)

Streptochilus macdougallae Miranda-Martinez, Carreño and McDougall, 2019 — Miranda-Martinez, 2019, p. 107, table 7.

Range: M14[Pac] (5.60-6.1 Ma) to PL1[Pac] (4.37-5.60 Ma)

Ecology: indicates high productivity (Hemleben et al., 1989; Resig and Kroopnick, 1983; Smart and Thomas, 2006; Darling et al., 2009)

Tenuitella guaymensis (Matoba and Oda) = *Turborotalita guaymensis* Matoba and Oda, p. 1018, pl. 5, figs. 1A-13B. = *Tenuitella guaymensis* (Matoba and Oda) — Miranda-Martinez, 2019, p. 107, table 7.

Tenuitella pseudoedita (Subbotina, 1960) — Miranda-Martinez, 2019, p. 107, table 7.

Comments: originally descried as *Globigerina pseudoedita* Subbotina, 1960 but may be placed in synonymy with *Tenuitella angustiumbilicata* (Bolli, 1957). Taxonomic discussion is ongoing (Beggren and Wade, 2018).

Range: FO in the equatorial Atlantic is 5.3 Ma (BouDagher, 2013).

Tenuitella juvenilis (Bolli, 1957) — Miranda-Martinez, 2019, p. 107, table 7.

Comments: This species was originally described as *Globigerina juvenilis* Bolli, 1957 but has been placed in synonymy with *Globigerinita glutinata* (Egger, 1893).

Range: O2 (30.28-32.1Ma) to extant

Ecology: tropical to subpolar, abundant in warm and temperate water (Kennett and Srinivasan, 1983; Pearson et al, 2018)

Tenuitellita cf. *iota* (Parker, 1962) — Miranda-Martinez, 2019, p. 107, table 7.

Ecology: indicates cooler conditions (Parker, 1971)

Trilobatus immaturus (Leroy, 1939) = *Globigerinoides immaturus* LeRoy 1939 — Miranda-Martinez, 2019, p. 107, table 7.

Range: M1a – nonextinct

Ecology: temperate water masses (Kennett and Srinivasan, 1983; Ave et al., 2011)

Trilobatus quadrilobatus (d'Orbigny, 1846) = *Globigerinoides quadrilobata* (d'Orbigny, 1846) — Miranda-Martinez, 2019, p. 107, table 7. = *Globigerina quadrilatera* Galloway and Wissler, 1927. — Carreño et al., 2015, p. 224. — Miranda-Martinez, 2019, p. 107, table 7. = *Globigerinoides quadrilobatus* (d'Orbigny, 1846) — Carreño et al., 2015, p. 224, pl. 1, fig. 2. = *Globigerina* aff. *quadrilatera* Galloway and Wissler, 1927 — Miranda-Martinez, 2019, p. 107, table 7.

Range: M1a (22.44-22.96 Ma) to non-extinct

Ecology: Cosmopolitan (Spezzaferri et al., 2018)

Trilobatus sacculifer (Brady, 1877) = *Globigerinoides sacculifer* Brady, 1877 — Carreño et al., 2015, pl. 1, fig. 5. — Miranda-Martinez, 2019, p. 107, table 7

Range: M4a (N6; 17.54-17.59 Ma) to extant

Ecology: warm water species found in low latitudes (Bandy, 1961; Kennett and Srinivasan, 1983; Brinton and Douglas, 1986; Kucera, 2007; Aze et al., 2011; Kumar and Srinivasan, 2016)

Trilobatus trilobus (Reuss) = *Globigerinoides trilobus* (Reuss, 1850) — Miranda-Martinez, 2019, p. 107, table 7

Range: M1a (22.44-22.96 Ma) to extant

Ecology: tropical (Be and Tolderlund, 1971; Spezzaferri et al., 2002; Kucera, 2007; Zagrosrk et al., 2007; Spezzaferri et al., 2018)

Turborotalita quinqueloba (Natland, 1938) — Miranda-Martinez, 2019, p. 107, table 7. = *Turborotalita* cf. *quinqueloba* (Natland, 1938) — Miranda-Martinez, 2019, p. 107, table 7.

Range: E14 (35.89-37.99 Ma) to extant

Ecology: tropical; high productivity (Bandy, 1961; Chaisson and Leckie, 1993; Antonarakou et al, 2007; Kucerea, 2007); peaks at cool latitudes (Pearson and Kucera, 2018).

Species in Carreño et al. (2015) but not found in this study:

Globigerinoides elongatus (d'Orbigny, 1826).

Globigerinoides ungulata Bermudez, 1960

Globorotalina puncticulata (Deshayes, 1832)

Neogloboquadrina humerosa (Takayanagi and Saitom 1962) - *N. dutertrei* (d'Orbigny 1839)